VI Taller sobre Metamateriales, Cristales Fotónicos, Cristales Fonónicos y Estructuras Plasmónicas

Centro de Convenciones del Hotel Real de Minas
San Miguel de Allende, GTO, México
11 – 14 de Enero, 2015

Invitados:

L. Mochán (Cuernavaca, UNAM)
C. Noguez (México, UNAM)
J. Sánchez-Dehesa (Valencia, UPV)
R. G. Barrera (México, UNAM)
F. Villa (León, CIO)
Y. Gurevich (México, CINVESTAV)
R. Méndez (Cuernavaca, UNAM)
F. Pérez (Puebla, IFUAP)
J. Flores (México, UNAM)
J. E. Lugo (Montreal, UM)
J. M. Nápoles (Chihuahua, UACH)

Cuerpos Académicos Participantes (PROMEP) :

Física de Materiales
(Facultad de Ciencias Físico Matemáticas, Puebla, BUAP)

Fenómenos Ópticos
(Departamento de Investigación en Física, Hermosillo, UNISON)

Participación abierta para sesión de *POSTERS*

Información:
DIF-US
Tel: (662) 2893792
Email: framos@cifus.uson.mx

VI Taller
de Metamateriales, Cristales Fotónicos, Cristales Fonónicos y Estructuras Plasmónicas
San Miguel de Allende, Gto, México
Enero 11-14, 2015

PROGRAMA

Domingo 11

19:00-20:00 Registro de Participantes.

Lunes 12

8:45-9:00 Bienvenida

SESIÓN 1

9:00-9:40 **Jesús Manzanares-Martínez** (CAFO, Universidad de Sonora)
Subwavelength mode conversion caused by bending in photonic waveguides.

9:40-10:20 **Felipe Pérez-Rodríguez** (CAEF, Benemérita Universidad Autónoma de Puebla)
Infrared response of metal-dielectric periodic multilayer stacks.

10:20-11:00 **W. Luis Mochán** (Invitado, ICF-UNAM, Cuernavaca)
Second harmonic generation in nanostructured metamaterials.

11:00-11:20 Café

11:20-12:00 **Yuri G. Gurevich** (Invitado, CINVESTAV-IPN)
Dember effect: mith and reality.

12:00-12:40 **Jorge Flores Valdés** (Invitado, IF-UNAM)
Doorway states in classical and quantum physics.

12:40-13:20 **Ruben G. Barrera** (Invitado, IF-UNAM)
Fórmulas de Fresnel extendidas para coloides turbios.

13:20-14:00 **J. Eduardo Lugo** (Invitado, University of Montreal)
Inducing forced – and auto – oscillations in one dimensional photonic crystal with light.

14:00-14:15 **Sesión de Posters I**, *in advance.*

14:15-17:00 Comida

SESIÓN 2

17:00-17:40 **Rosendo Lozada-Morales** (CAFM-Benemérita Universidad Autónoma de Puebla)
Composition dependence of the crystalline-to-amorphous phase transformation of vanadate compounds in the CdO-V_2O_5 binary system.

17:40-18:00 **María Elena Zayas-Saucedo** (CAFO-Universidad de Sonora)
The zone formation of glass in the CdO-TeO_2-GeO_2 system.

18:00- 18:15 Instalación de Posters

18:15-19:30 **SESIÓN DE POSTERS I.**

1. **A Maldonado García**, Y. A. González-Rivera, L. Aquino Meneses, R. Lozada Morales, S. Jiménez Sandoval, E. Rubio Rosas, O Zelaya Angel, and F. Rodríguez Melgarejo,
   Photoluminescence and electro-optical characterization of Nd-doped (ZnV_2O_6, $Zn_2V_2O_7$).
2. **I. V. García Amaya**, M. E. Zayas Saucedo, J. Alvarado Rivera, B. Manzanares Martínez and R. Lozada Morales,
   Raman and FT-IR spectroscopy characterization of glasses with high TeO_2 content.
3. **Y. A. González Rivera**, E. Cervantes Juárez, L. Aquino Meneses, R. Lozada Morales,
   Photoluminescence in Er-doped V_2O_5 and Er-doped CdV_2O_6.
4. **E. Cervantes Juárez**, R. Lozada Morales,
   Analysis of vanadate compounds and glasses from the Cu-CdO-V_2O_5 ternary systems.
5. **P. M. Trejo García**, M. R. Palomino Merino, J. E. Espinosa Rosales, R. Aceves Torres,
   Synthesis and luminescence characterization of $Li_2B_4O_7$ doped with Manganese and Europium.
6. **B. Manzanares Martínez**, E. Cervantes Juárez, R. Lozada Morales y M. E. Zayas Saucedo,
   Caracterización mecánica por métodos ultrasónicos de vidrios ZnO-CdO-V_2O_5 dopados con Neodimio y Erbio.
7. **E. Gutiérrez Reyes**, J. Flores Méndez, A. L. González, F. Pérez Rodríguez,
   Efective elastic constants for three dimensional elastic materials.
8. **J. A. Lima Flores**, M. R. Palomino Merino, and E. Rubio Rosas,
   Synthesis and characterization of titanium dioxide nanotubes by hydrothermal method assisted by microwave.
9. **J. G. Quiñones Galván**, E. Campos, S. Muhl, M. Flores,
   TiAlN thin films deposited by laser ablation.

10. **C. E. Ávila Crisóstomo,** F. Sánchez Mora, F. Perez Rodríguez**,**
    Synthesis and modeling of SiO_2 opals with Fe inclusions.
11. **V. Chabanenko**, E. Zubov, R. Cortés-Maldonado, F. Pérez Rodriguez, R. Escudero, F. Morales, R. Kochkanjan, A. Zaritovskii, O. Kuchuk, S. Zolotar, A. Nabialek,
    Magnetic Properties of nanostructured C-Co and C-Ni complexes.
12. **S. Tehuacanero-Cuapa**, J. Reyes Gasga, M. R. Palomino merino and R. García García.
    Holes drilling in gold and silver decahedral nanoparticles by the convergent beam electron diffraction electron beam.
13. **A. J. Carmona Carmona**, M. A. Palomino Ovando, M. R. Palomino Merino, E. Sánchez,
    Growth and optical characterization of inverse opals generated by mixing $SiO_2 – TiO_2$.

Martes 13

SESIÓN 3

9:00-9:40 **José Sánchez-Dehesa** (Invitado, DIE- Universidad Politécnica de Valencia)
Absorption enhancement by lattice of perforated shells.

9:40-10:20 **F. Villa-Villa**, (CAEF, CIO)
Nystrom integral equation method for the propagation of 3D acoustic waves.

10:20-11:00 **Rafael A. Méndez Sánchez**, (CAEF, ICF-UNAM, Cuernavaca)
Bloch oscillations in elastic systems.

11:00-11:20 Café

SESIÓN 4

11:20-12:00 **Cecilia Noguez** (Invitada, IF-UNAM)
Designing the plasmonic response of metallic nanoparticles.

12:00-12:20 **R. García Llamas** (CAFO, Universidad de Sonora)
Diffraction of light by two dimensionally structured metallic surfaces.

12:20-12:40 **J. A. Gaspar Armenta** (CAFO, Universidad de Sonora)
Metal – 2D photonic cristal interface: surface modes interacting with waveguide modes.

12:40-13:00 **J. M. Nápoles-Duarte** (Invitado, FCQ, UACh)
Understanding the origin of core-shell mode interactions in plasmonic tubes.

13:00-13:40 **Eugenio Méndez** (Invitado, CICESE)
Numerical studies of the efficiency of excitation of surface plasmon-polaritons by compact surface structures.

13:40-14:00 **Sesión de Posters II**, *in advance.*

14:00-14:15 Fotografía de participantes.

14:15-17:00 Comida

SESIÓN 5

17:00-17:20 **B. Flores Desirena** (CAFM, Benemérita Universidad Autónoma de Puebla)
Two-dimensional dispersive photonic crystals from the plane wave method,

17:20-17:40 **F. Ramos-Mendieta** (CAFO, Universidad de Sonora)
Mid-infrared Otto excitation of transverse electric surface plasmons in doped graphene.

17:40-18:00 **E. I. Kuchuk**, (Invitada, IPE, Ucrania)
Fractal-like structure of magnetic field penetration into superconducting NbTi disc: stochastic jumps of flux bundles and Meissner holes.

18:00-18:15 Instalación de Posters.

18:15-19:30 Sesión de Posters II.

1. **Y. J. Rodríguez-Viveros**, B. Manzanares Martínez, P. Castro Garay, D. Moctezuma Enriquez, C. I. Ham Rodríguez and J.Manzanares Martínez, *Dynamical modeling of the radiation emitted by a luminescent dye embedded in a slab*.
2. **L. A. Mayoral Astorga**, J. A. Gaspar Armenta, F. Ramos Mendieta, *Inhomogeneous fields for surface plasmon excitation.*
3. **A. Arreola Lukas**, G. Baez, J. A. Franco Villafañe, R. A. Méndez Sánchez,
In-plane vibrations of a rectangular plate: plane-wave expansion modelling and experiment.
4. **E. Juárez Pérez**, M. A. Palomino Ovando,
Delay times in layered structures with dielectric and metamaterial constituents.

5. **D. Márquez Ruiz**, F. Ramos Mendieta and B. Manzanares Martínez, *Cristal fotónico 1D de componentes magnetoreológicas sintonizable con campo magnético.*
6. **J. A. Hernández López**, M. A. Palomino Ovando and F. Ramos Mendieta, *Excitation of Surface plasmons on graphene via ATR and multilayer graphene study for TM polarization.*
7. **A. Konovalenko**, J. A. Reyes Avendaño and F. Pérez Rodríguez, *Influence of metal conductivity on the chirality of metamaterials with twisted U-shaped resonators.*
8. **E. Flores Olmedo**, G. Báez, M. Martínez Mares and R. A. Méndez Sánchez, *Transport of mechanical vibrations in 2D elastic chaotic cavities.*
9. **H. Kinto-Ramírez**, M. A. Palomino Ovando and F. Ramos Mendieta, *Reducción de los efectos de absorción en la propagación de la radiación electromagnética en cristales fotónicos construidos con materiales izquierdos y derechos*.
10. **B. Manzanares-Martínez**, C. I. Ham Rodríguez, D. Moctezuma Enríquez, and J. Manzanares Martínez, *Detección de modos guiados en guías de onda acústica.*
11. **J. E. Pérez Rodríguez**, M. A. Palomino Ovando and G. Hernández Cocoletzi, *Surface modes coupling in one-dimensional metamaterial photonic crystals with defects.*
12. **F. Ramírez Ramírez**, G. Báez, J. A. Franco Villafañe, and R. A. Méndez Sánchez *In-plane vibration in a two-dimensional periodic elastic system: experimental realization.*
13. **C. I. Ham-Rodríguez**, J. Manzanares Martinez, Y. J. Rodríguez Viveros, B. Manzanares Martínez. P. Castro Garay and D. Moctezuma Enriquez, *Asymmetric propagation between subwavelength planar waveguides.*
14. **Noemi Sánchez**, J. E. Lugo and M. A. Palomino Ovando, *Theoretical and experimental study of electromagnetic forces induced in 1D photonic crystals.*

Miércoles 14

9:00-10:00	Sesión de trabajo de Cuerpos Académicos de la RED. Proyecto 2015-2016.
10:00-10:30	Conclusiones generales y propuestas de colaboración. Asamblea general de participantes. Clausura.

Sesión 1

Subwavelength mode conversion caused by bending in photonic waveguides

D. Moctezuma-Enriquez,[1] Y. J. Rodriguez-Viveros,[2] B. Manzanares-Martinez,[2]
C. I. Ham-Rodriguez,[3] E. Urrutia-Banuelos,[3] and J. Manzanares-Martinez[3,a)]

[1]*Centro de Investigacion en Materiales Avanzados (CIMAV), Miguel de Cervantes 120, Chihuahua 31109, Mexico*
[2]*Departamento de Fisica, Universidad de Sonora, Blvd. Luis Encinas y Rosales, Hermosillo, Sonora 83000, Mexico*
[3]*Departamento de Investigacion en Fisica, Universidad de Sonora, Apartado Postal 5-088, Hermosillo, Sonora 83000, Mexico*

Optical Fibers (OF) are dielectric waveguides in the form of cylinders with a diameter (d) larger than the visible range wavelengths ($\lambda_v = 390{\sim}700\ nm$) [1]. OF are flexible waveguides, however the angle of bending (θ) is limited by a critical angle (θ_c) defined by the principle of Total Internal Reflection (TIR). They are widely used in optical networks, sensors and other devices. Nowadays to control the flow of data on the telecom industry coexist optical and electronic devices. On the one hand, for long distances photons are transported via optical fibers, which support high band-widths with low-losses. On the other hand in the electronic circuitry, the essential functions of switching and routing are made by manipulating the flow of electrons. The bottleneck for data transfer in this hybrid technology is the operation frequency of the electronic processors which currently is of only a few GHz. To increase the speed of data transfer in optical networks it has been proposed the development of Photonic Integrated Circuits (PIC). A PIC does analogous main functions to those of Electronic Integrated Circuits (EIC). The difference is that PIC provide a direct manipulation of the photons traveling in optical waveguides. It is expected that the processing of light in PIC will be able to overcome the physical limitations of speed and power dissipation faced by EIC.

A progressive development of PIC has been made in the last two decades, which can be classified on three main approaches. A first approach is based on the use of Photonic Crystals (PC) as a framework for the design of photonic devices to control the flow of light. PC are periodic dielectric structures composed by at least two materials in the unit cell of period d which is on the order of the visible wavelength, $d{\sim}\lambda_v$. The fundamental characteristic of PC is the existence of Photonic Band Gaps (PBG) where photons cannot propagate through the periodic lattice. Photonic devices of the order of the visible wavelengths can be engineered in PC introducing localized states in the PBG by removing unit cells in the otherwise perfect crystal. A second strategy to design PIC is based on the use of plasmons. Plasmon-based approaches require a precise manipulation of the electromagnetic fields, which are exponentially decaying from the surfaces. It has been suggested the possibility of creating surface-plasmon circuitry with photonic components smaller than the diffraction limit of light. Plasmons however have substantial optical losses which can severely limit their applicability. To overcome these losses, it has recently been suggested the use of gain-loss structures which introduce unusual possibilities for the propagation of plasmons.

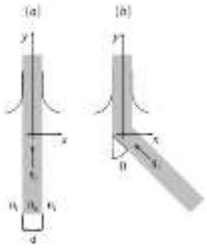

FIG. 1: (a) Planar waveguide of width d and refractive index n_h between two semi-infinite media of refractive index n_l . (b) Waveguide with an angular bend θ.

A third approach to fabricate PIC is based on the use of nanowires. In a similar manner to OF, dielectric nanowires are cylindrical waveguides but with a subwavelength diameter which is smaller than the visible wavelength, $d < \lambda_v$. In contrast to OF where a diameter $d > \lambda_v$ allow multimodal propagation, the subwavelength diameter permits precise control and manipulation of light which is desirable for the design of optical devices.

In the last decade an intensive effort has been made to reduce the width of waveguides. The fabrication of optical waveguides with diameters smaller than the wavelength is a difficult task. For many years was not possible to attain nanowires with a good quality fabrication cause of inherent disorder in the fabrication process such as the existence of surface roughness and diameter variations. In 2003, L. Tong *et al.* reported an experimental technique that allowed fabricating wires with diameters as small as 50 nm with an excellent quality. These subwavelength nanowires allowed a higher confinement of photons in small volume regions opening new possibilities for both, the study of fundamental properties and their integration into functional devices. The use of subwavelength waveguides has spun the development of at least five fundamental building blocks for photonic circuitry; i) light sources (lasers), ii) passive components (interconnects), iii) active components (transistors), iv) nonreciprocal optical isolators (diodes), and v) light detectors.

In this work the conversion of modes is studied for the planar waveguide sketched in Fig. 1. Panel (a) presents a slab of width d and high refractive index n_h sandwiched between two semi-infinite media of low refractive index n_l. Panel (b) illustrates an angular bending of the slab with an angle θ. We analyze the case of the Transversal

Electric (TE) polarization where the electric field is parallel to the z-axis, $E_z(x,y)$. The electromagnetic waves inside and outside the slab are propagating and evanescent, respectively.

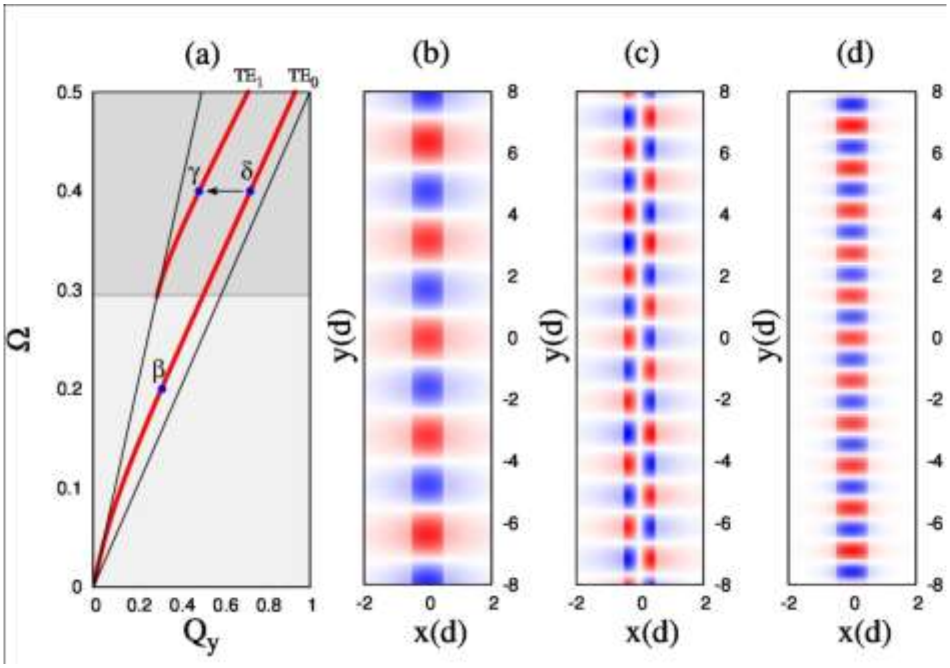

Fig. 2 (a) Dispersion relation for a planar waveguide of width d. The light and dark gray regions are the monomodal and multimodal regimes. The β and δ points belong to the TE_0 mode while the γ point is part of the TE_1 mode. Panels (b), (c) and (d) are the electric profile of the eigenmodes at the β, γ and δ points, respectively.

Infrared response of metal-dielectric periodic multilayer stacks

Felipe Pérez-Rodríguez

Instituto de Física, Benemérita Universidad Autónoma de Puebla,
Apdo. Post. J-48, Puebla, Pue. 72570, Mexico

The optical properties of metal-dielectric superlattices are here revisited. Commonly, the electrodynamic properties of such periodic heterostructures are described within the Drude model, which is based on the assumption of a local relation between the electrical current density and the electric field. Nevertheless, because of the high mobility of conduction electrons and inhomogeneity of the electromagnetic field in metals, the constitutive equation actually has an integral form and, consequently, is nonlocal. It is well established that such a nonlocality (spatial dispersion) is responsible for the anomalous skin effect. Evidently, the simple Drude model absolutely ignores the spatial dispersion effects. In addition, when the size of the metallic layers is comparable with the skin depth of the electromagnetic field penetration, as it occurs in modern micro- and nanostructures, it is necessary to consider the size effect. In the talk, we will analyze the spatial-dispersion and size effects upon the photonic band structure of one-dimensional periodic metallodielectric systems. The nonlocal relation between the electric current density and the electric field inside the metal layers is calculated within the formalism of the Boltzmann kinetic equation. If the metallic layers are thin enough, the photonic band structure for the superlattice exhibits narrow pass bands due to the very strong contrast between the impedances of the metal and the dielectric. The narrow pass bands are associated to Fabry-Perot resonances occurring inside the relatively-thick dielectric layer. The metal spatial dispersion is well manifested in the infrared and, therefore, the nonlocal effect upon the photonic band structure of the one-dimensional periodic crystal is particularly strong when the Fabry-Perot resonance bands are precisely in such a frequency range. Recent results for the photonic band structure of Al-dielectric superlattices [1], which were obtained within the nonlocal formalism and compared with the predictions of the local Drude model, are here discussed. As it is shown, the differences between the local and nonlocal formalisms are rather noticeable not only in the magnitude, but also in the sign of the real part of the Bloch wave number within the very narrow Fabry-Perot resonance bands.

Since the metal spatial dispersion is particularly strong in the infrared, the photonic band structure for a superlattice, composed of a nonlocal metal and a resonant dielectric (e.g. an ionic crystal or heteropolar semiconductor), would be altered at frequencies of the forbidden band. The latter is created from the coupling between the transverse optical phonons and the transverse electromagnetic waves inside the dielectric. Here, the infrared spectrum for a superlattice composed of alternating resonant dielectric and metal layers is analyzed. The dielectric component is assumed to be characterized by a local (independent of the wave vector) resonant dielectric function, which is modeled with a Lorentz oscillator. After solving Maxwell equations for the electromagnetic fields in each superlattice layer and applying the boundary conditions together with the Bloch theorem, an analytic expression for the photonic dispersion relation in terms of the surface impedances at the interfaces of the metal and dielectric layers is obtained. Due to the large difference between the permittivities of the metal and dielectric components, the photonic band structure exhibits flat pass bands associated with Fabry-Perot resonances in the dielectric layers. There is also a wide stop band because of the existence of the polaritonic gap. Another fundamental distinction from the ordinary situation, when the dielectric possesses a linear photon dispersion, consists in the fact that the Fabry-Perot resonances in the case of a polar material are defined by the nonlinear polariton dispersion. The results are compared with the predictions of the Drude model for the frequency-dependent metal permittivity. It is found that the nonlocal effect on the Fabry-Perot resonance bands is strong if their corresponding frequencies are in the interval where the difference between the impedances at both metal surfaces, predicted by the nonlocal and local formalisms, is maximal.

Results for Bi/ionic-dielectric superlattices will also be analyzed. Such superlattices are of interest because the infrared response of Bi is well described by the Drude model, but with a plasma frequency in the same range and a relatively-large background dielectric constant. As a result, the infrared photonic band structure of the superlattices depends on the relative position of the polaritonic gap with respect to the Bi plasma frequency. The photonic dispersions for TE and TM plasma-phonon polaritons in superlattices composed of alternating Bi and resonant-dielectric (NaBr, LiCl, LiH) layers will be presented and discussed.

Acknowledgment

This work was partially supported by SEP-CONACYT (grant CB-2011-01-166382).

Reference

[1] A. Paredes-Juárez, D. A. Iakushev, B. Flores-Desirena, N. M. Makarov, and F. Pérez-Rodríguez, “Nonlocal Effect on Optic Spectrum of a Periodic Dielectric-Metal Stack,” Opt. Express **22**, 7581–7586 (2014).

Second Harmonic Generation in Nanostructured Metamaterials

W. Luis Mochán[1], Bernardo S. Mendoza[2], and Guillermo P. Ortiz[3]

[1]*Instituto de Ciencias Físicas, UNAM, Cuernavaca, Morelos, México.*
[2]*Centro de Investigaciones en Óptica, León, Guanajuato, México.*
[3]*FCENA, Universidad Nacional del Nordeste, Corrientes, Argentina.*

The surface of the nanoparticles in a composite metamaterial may be a source of strong SH radiation, but only if their geometry is itself non-centrosymmetric. We present an efficient scheme for its calculation.

Introduction. The nonlinear dipolar second order third rank susceptibility tensor responsible of second harmonic generation (SHG) vanishes due to selection rules within centrosymmetric media. Nevertheless, at surfaces the centrosymmetry is necessarily lost and a large second order dipolar polarization may be induced within a thin region close to the interface of an otherwise centrosymmetrical system [1]. Thus, it may be expected that nanoparticles made up of centrosymmetrical materials could be sources of a large SH signal, given their large surface to volume ratio. Unfortunately, for simple geometries which are themselves centrosymmetrical, such as that of a sphere, the strong SH contributions from opposite sides of the particle cancel out, leaving only a multipolar SH signal [2]. The quadrupolar nature of the SH radiated by arrays of nanoparticles has been confirmed experimentally and techniques have been developed to enhance their SH signal [3].

In this paper we study the SH polarization produced by an ordered array of nanoparticles made up of centrosymmetrical materials when their geometry is not centrosymmetrical. In this case, the surface SH signal is not cancelled out when adding contributions all around the particles. To study this case we extend a formalism used previously to calculate very efficiently the macroscopic dielectric response of nanostructured metamaterials of arbitrary geometry and composition [4]. This formalism uses using Haydock's recursion to obtain a basis in which the longitudinal microscopic dielectric function is represented as a tridiagonal matrix, allowing its efficient inversion, from which the macroscopic tensor may be identified. As a bonus, this method yields a set of Haydock states which allow the calculation of the microscopic electric field.

As the microscopic field has rapid spatial variations across the surface of the nanoparticles, it produces an appreciable second harmonic polarization, which we calculate using a *continuous dipolium* model applied to flat surfaces [1].

Results. Fig. 1 shows the magnitude and direction of the microscopic linear field within a 2D square lattice of holes within a conductor. The holes are pear shaped so that the system is not invariant under a $x \rightarrow -x$ reflection, although it is invariant under a $y \rightarrow -y$ reflection. The conductor is described by a Drude dielectric function characterized by its plasma frequency ω_p and lifetime $\tau=100/\omega_p$. The macroscopic electric field points along the vertical *y* direction. The frequency was taken as $\omega=0.55\omega_p$. Notice there are several hot regions along the surface of the holes where the field is particularly large due to a resonant excitation of localized surface plasmons.

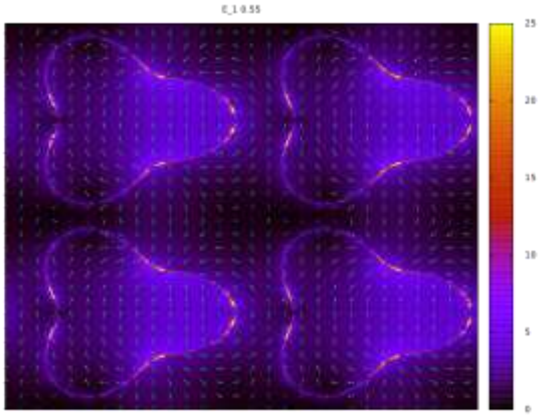

Fig. 1. Magnitude and direction of the microscopic linear field for a 2D square array of pear shaped holes within a conductor

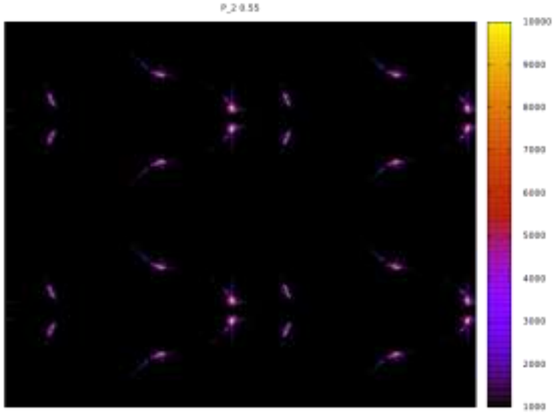

Fig. 2 Magnitude of the nonlinear polarization for the same system as in Fig. 1.

Fig. 2 shows the magnitude of the nonlinear polarization induced by the field shown in Fig. 1. Notice that the polarization is strongly concentrated at the surface of the holes in the neighborhood of the hot spots mentioned previously. Averaging the nonlinear polarization we obtained the macroscopic nonlinear polarization which turns out to point along *x*, as expected from symmetry, and the nonlinear susceptibility χ_{xyy}. Considering other field directions we obtain all the components of the second order susceptibility.

Conclusions. Whenever their geometry is noncentrosymmetric, nanostructured metamaterials have a finite dipolar quadratic susceptibility even if their components are centrosymmetric. The suceptibility we obtained is smaller than that of non-centrosymmetric materials, but it is not negligible, and it may be continuosly tuned, as well as the linear dielectric tensor, by modifying the geometry of the system. These results suggest that novel sources of SH radiation, such as phase matched non-linear optical fibers using glass or other ordinary materials may be designed by tuning a few appropriate geometrical parameters.

Acknowledgements

This work was supported by DGAPA-UNAM under grant IN108413.

References

[1] B.S. Mendoza and W.L. Mochán, Phys. Rev. B **53**, 4999 (1996).
[2] W.L. Mochán et al. Phys. Rev. B **68**, 085318 (2003).
[3] P. Figliozzi et al. Phys. Rev. Lett. **94**, 047401 (2005).
[4] W.L. Mochán et al., Optics Express **18,** 22119-22127 (2010).

Dember Effect: Myth and Reality

Yuri G. Gurevich
Depto. De Fisica, CINVESTAV-I.P.N.
Mexico D. F.
gurevich@fis.cinvestav.mx

The photoelectric Dember effect is one of the classic photoelectric phenomena in semiconductors. It was discovered in 1931 [1], and describes the photoelectromotive force (photo-EMF) in a homogeneous finite size semiconductor under nonuniform illumination. The theory explaining this effect was proposed almost at the same time [2–4]. In those studies an expression for the Dember EMF was obtained. It was found that the Dember EMF is proportional to the difference of the diffusion coefficients of electrons, *Dn*, and holes, *Dp*, *Dn –Dp*. Subsequently, this result served as the support for the explanation of the nature of this EMF as due to ambipolar diffusion of nonequilibrium electrons and holes [5–10].

The theory of the Dember effect bears an additional interest because its description is based on the same ideas and equations as the ones used for the description of solar cells. Therefore, the understanding of basic principles of formation of the Dember EMF will help to further develop the theory of solar cells.

One of the main applications of the photo-Dember effect is the generation of terahertz (THz) radiation pulses for terahertz time-domain spectroscopy. This effect is present in most semiconductors but it is particularly strong in narrow-gap semiconductors (mainly arsenides and antimonides) such as InAs and InSb [11–13] owing to their high electron mobility. Experimentally, and in a number of theoretical studies [14–17] based on simulations, it was found that the magnitude of the Dember EMF obtained under semiconductor excitation by short laser pulses should be considerably higher than the typical stationary values expected according to the established theory. The photo-Dember terahertz emission should not be confused with the surface field emission, that takes place if the surface energy bands of a semiconductor fall between its valence and conduction bands, producing a phenomenon known as Fermi level pinning; Fermi level pinning would originate band bending and, subsequently, the formation of a depletion or an accumulation layer close to the surface. This layer would contribute to the acceleration of charge carriers [12]. These two effects can contribute constructively or destructively for the dipole formation depending on the direction of the band bending.

Unfortunately, the explanation of the nature of the Dember EMF found in the literature that attributes its origin to the difference between the diffusion coefficients of electrons and holes is incorrect. The analysis of the conventional calculation and explanation of the Dember EMF that is presented in, for instance, reference [18], assumes the absence of total current in the circuit. As a result, the field of forces of nonelectrical nature is identified with an electric field that would arise to compensate the diffusion fluxes in the semiconductor. The gradients of the electrochemical potentials (Fermi quasilevels of electrons and holes) are responsible for carrier movement in the semiconductor. The Fermi quasilevel includes both the electric field and the concentration gradient. The result of this movement in the case of the Dember effect is the setting up of an EMF. The correct calculation of EMF is possible only in a closed circuit by using the Ohm's law after calculation of the internal resistance of the source. Subsequently, the EMF in an open circuit is obtained in the limit when the value of theloading resistance tends to infinity.

In reference [18] a new approach to calculate of the Dember EMF was proposed that was free of all of the above-mentioned shortcomings, and a new expression for the EMF was obtained. In the model used in [18] both strong absorption at the surface and an absence of bulk recombination and recombination on the illuminated contact (under these conditions the Dember effect exhibits its maximum value) was assumed.

In reference [19] it was demonstrated that the precise physical nature of the Dember effect is a concentration gradient of nonequilibrium carriers under nonuniform illumination. It was used the fact that any photo-EMF can only exist in the presence of nonequilibrium charge carriers, when there are two different Fermi quasilevels. That is why the Dember EMF (as the photo-EMF of any nature) is not identified as a voltage drop arising between the device contacts in open circuit. It was shown that the Dember EMF does not depend on the difference of electron-to-hole diffusion coefficients and it is not linked to ambipolar diffusion. Additionally, it was found that the sign of the EMF depends on the ratio between the recombination rates on the contacts, which can be detected from the spectral characteristic of the Dember EMF.

The aim of this report is to propose a full linear theory of the Dember effect, which takes into account the real experimental conditions for measuring and using the Dember EMF.

Using the general approach based on continuity equations for nonequilibrium carriers in the linear approximation and a closed circuit we clearly demonstrated that the precise physical nature of Dember effect is related to the nonhomogeneous concentration of nonequilibrium carriers. Accordingly, the Dember EMF does not change its sign when the sign of $Dn - Dp$ changes. The Dember EMF can change its sign when recombination at the illuminated contact exceeds recombination at the dark contact.

Let us remark that the obtained expression for EMF is nonsymmetrical with respect to holes and electrons. This result is explained by the absence of hole current in metal contacts. Under the linear theory the Dember EMF exhibits a maximum value in p- and i-type semiconductors and a minimum value in n-type semiconductors.

[1] H. Dember, Phys. Zeits. **32**, 554 (1931); **32**, 856 (1931); **33**, 207 (1932).
[2] H. Frohlich, Phys. Zs. Sowjet **8**, 501 (1935).
[3] J. Frenkel, Nature **132**, 312 (1933); Phys. Zs. Sowjet. **8**, 185 (1935).
[4] L. Landau and E. Lifshts, Ztshr. Sow. **9**, 477 (1936).
[5] B. Parent, S. O.Macheret, and M. N. Shneider, J. Computational Physics **230**(22), 8010 (2011).
[6] A. A. Abdullaev, A. R. Aliev, and I. K. Kamilov, Semiconductors **37**(10), 1156 (2003).
[7] K. Seeger, Semiconductor Physics (Springer, Berlin, 1985).
[8] T. S. Moss, G. J. Burrell, and B. Ellis Semiconductor Opto-Electronic (Butterworth and Co., London, 1973).
[9] S. M. Rivkin, Photoelectric Phenomena in Semiconductor (Nauka,Moscow, 1963).
[10] J. Tauc, Photo and Thermoelectric Effects in Semiconductors (Pergamon Press, N.-Y., Oxford, London, Paris, 1962).
[11] T. Dekorsy, Phys. Rev. B **53**, 4005 (1996).
[12] S. Kono, P. Gu, M. Tani, and K. Sakai, Appl. Phys. B **71**(6), 901 (2000).
[13] P. Gu, M. Tani, S. Kono, K. Sakai, and X.-C. Zhang, J. Appl. Phys. **91**, 5533 (2002).
[14] M. B. Johnston, Phys. Rev. B **65**, 165301 (2002).

[15] V. L.Malevich, Semiconductors **40**(2), 155 (2006).
[16] P. A. Ziaziulia, V. L. Malevich, I. S. Manak, and A. Krotkus, Semiconductors **46**(2), 143, (2012).
[17] A. Reklaitis, J. Appl. Phys. **108**, 053102 (2010).
[18] Yu. G. Gurevich and A. V. Meriuts, Phys. Lett. A **377**, 2673 (2013).
[19] A. V. Meriuts, Yu. G. Gurevich, Ann. Phys. (Berlin) **526,** 533, (2014).

Doorway states in classical and quantum physics

Jorge Flores
Instituto de Física
Universidad Nacional Autónoma de México

Doorway states, first recognized in the forties as giant-dipole resonances in nuclei, are now ubiquitous. They have been recently discussed in several atomic and molecular systems as well as in clusters, quantum dots, fullerenes and also in nucleon-nucleus collisions. The influence of the doorway state on the spectral properties of nuclei has also been considered. A connection between doorway states and super-radiant dynamics was established. Furthermore, the doorway state phenomenon has been observed in classical systems: microwave resonators and in the seismic response of sedimentary basins. In all these cases, a state of a “distinct” and simple nature is immersed in a “sea” of states of a different, more complicated, structure and the strength function phenomenon appears: The amplitude of the distinct state, which is not an eigenstate of the complete Hamiltonian, is spread over the complicated eigenstates with a Lorentzian-like shape. The distinct state acts as a doorway state whenever this simple state is coupled to the continuum and to the sea of complicated states, but the latter are coupled to the continuum only through the distinct, simple state.

We present here, both from the experimental and theoretical points of view, the doorway state phenomenon in a special chain of harmonic oscillators, a quasi-one dimensional elastic rod, in the seismic response of the valley of Mexico, and in an optical device formed by dielectric films.

The doorway state phenomenon is a very general one: It appears in systems covering a range in size of 19 orders of magnitude, it also applies to systems with chaotic spectra as well as to integrable systems.

Fórmulas de Fresnel extendidas para coloides turbios

Rubén G Barrera[1], Edahí Gutiérrez-Reyes[2], Gesuri Morales-Luna[3] y Augusto García-Valenzuela[4]
[1]Instituto de Física de la Universidad Nacional Autónoma de México.
[2]Institutto de Física “Luis Rivera Terrazas” de la Benemérita Universidad Autónoma de Puebla
[3]Posgrado en Ciencias Físicas de la Universidad Nacional Autónoma de México.
[4]Centro de Ciencias Aplicadas y Desarrollo Tecnológico de la Universidad Nacional Autónoma de México.

En este trabajo presentamos unas nuevas fórmulas para las amplitudes de reflexión de la luz en coloides turbios, estas fórmulas tienen una estructura parecida a las bien conocidas fórmulas de Fresnel de la electrodinámica continua, razón por la cual las hemos llamado. Fórmulas extendidas de Fresnel. Los coloides son sistemas de dos fases consistentes en una fase dispersa (partículas coloidales) inmersa en otra fase continua (matriz). Cuando el tamaño de las partículas coloidales llega a ser del mismo orden de magnitud que la longitud de onda λ_0 del haz incidente, el fenómeno de esparcimiento de la luz por las partículas coloidales es tal, que el campo electromagnético en el seno del sistema está compuesto por dos componentes: una componente que viaja con una dirección definida (haz coherente) y otra componente que viaja en todas direcciones (campo difuso) y es la que da origen a la turbidez.

Cuando las partículas coloidales son mucho más pequeñas que λ_0, aunque el esparcimiento también existe, la potencia transportada por el campo difuso es tan pequeña comparada con la transportada por el haz coherente, que simplemente se ignora. En este caso siempre es posible describir las propiedades ópticas del coloide con una teoría de medio efectivo, es decir, es posible encontrar, por ejemplo, un índice de refracción efectivo que se puede utilizar, sin problema, en la ley de Snell y en las fórmulas de Fresnel aprovechando todos los resultados de la electrodinámica continua y tratando al coloide como un material ordinario con propiedades “efectivas”. Pero cuando el coloide es turbio, la presencia del campo difuso no hace claro saber, si es siquiera posible definir algo como un índice de refracción efectivo. Sin embargo, el haz coherente se refleja y se refracta de manera similar a la de los materiales ordinarios, por lo tanto si se ignora la presencial del campo difuso es tal vez posible construir una teoría de medio efectivo y caracterizar al coloide turbio con propiedades efectivas que describan sólo el comportamiento del haz coherente.

La primera fórmula reportada para el índice de refracción efectivo n_{eff} de un coloide turbio aparece en el libro de H. C. van de Hulst “*Light Scattering by Small Parteicles*” en el año de 1957 y que ha sido re-impreso por la editorial *Dover Publications Inc*. en 1981 [1]. Esta fórmula se escribe:

$$\frac{n_{eff}}{n_M} = 1 + \frac{3}{2} f \frac{S(0)}{(ka)^3} \tag{1}$$

en donde n_M es el índice de refracción de la matriz, f es la fracción de volumen ocupada por las partículas coloidales, $S(0)$ es la amplitud de esparcimiento de las partículas coloidales, inmersas en la matriz, en la dirección de incidencia, *k* es el vector de onda de la luz en el seno de la matriz y *a* es el radio de las partículas coloidales. Sin embargo al utilizar está fórmula indiscriminadamente en los resultados de la electrodinámica continua, se encontró que en muchos casos no daba lugar a resultados consistentes. Por ejemplo, al tratar de utilizarla para determinar el índice de refracción efectivo de un coloide turbio utilizando un refractómetro tipo Abbe, se encontraba que no era no era posible definir con precisión el ángulo crítico, dando lugar a incertidumbres y ambigüedades en la determinación del índice de refracción efectivo [2].

Mucho del trabajo en los últimos años dedicados a este proyecto, ha sido precisamente el aclarar y resolver muchas de las dudas y problemas sobre el origen físico de estas incertidumbre y ambigüedades. Nuestros resultados se pueden resumir de la siguiente manera:

(i) Sí es posible definir un índice de refracción efectivo en un coloide turbio, al igual que una permitividad efectiva ε_{eff} y una permeabilidad efectiva μ_{eff}, sin embargo, se encuentra que tanto ε_{eff} como μ_{eff} gozan de dispersión espacial [3], es decir, no dependen sólo de la frecuencia ω, sino también del vector de onda k, del haz incidente, por lo tanto se tiene que : $\varepsilon_{eff}(k,\omega)$ y $\mu_{eff}(k,\omega)$. Sin embargo, la relación de dispersión para modos transversales

$$k = \frac{\omega}{c}\sqrt{\varepsilon_{eff}(k,\omega)\,\mu_{eff}(k,\omega)}\,, \qquad (2)$$

hace posible obtener $k(\omega)$ y de ahí escribir $k(\omega) = (\omega / c)\, n_{eff}(\omega)$ para obtener un índice de refracción efectivo que depende sólo de la frecuencia. En la Ref. [3] se muestra también que el índice de refracción efectivo deducido por van de Hulst [Ec. (1)] es, en muchos casos, una muy buena aproximación al que se obtiene utilizando la Ec. (2). Como colofón es interesante hacer notar que el sistema coloidal tiene una repuesta magnética muy apreciable (magnetismo óptico), aunque las partículas coloidales sean no magnéticas..

(2) Dado que la respuesta electromagnética goza de dispersión espacial, es claro entonces que no es posible utilizar $\varepsilon_{eff}(k,\omega)$ y $\mu_{eff}(k,\omega)$ en las relaciones de Fresnel, las cuales asumen que tanto ε_{eff} y μ_{eff} dependen sólo de la frecuencia y no sen ven alterados por la presencia de la interfaz. Este no es el caso en presencia de dispersión espacial, es más, la presencia misma de la interfaz exige que al romperse la invariancia translacional, la respuesta electromagnética no dependa sólo de (k,ω) sino que dependa de dos vectores de onda, es decir, que dependa de $(\vec{k},\vec{k}';\omega)$. Esto hace que ya *no* sea posible definir un medio efectivo, dado que en la electrodinámica continua no existen propiedades macroscópicas que dependan de $(\vec{k},\vec{k}';\omega)$. Esto nos obliga a replantear el problema desde sus inicios y a partir de las propias ecuaciones de Maxwell, lo cual hacemos formulándolas como ecuaciones integrales, resolviéndolas en el límite diluido, es decir, cuando el volumen ocupado por las partículas coloidales no es muy grande. En una cierta aproximación, a la que llamamos “heurística”, por razones que por ahora no tenemos espacio para abundar, obtenemos que las amplitudes de reflexión para polarización *s* y *p*, para una interfaz entre dos medios: la matriz sin partículas y la matriz con partículas. Está fórmulas están dadas por [4]:

$$r_{s,p}=\frac{S_{\alpha}(\theta_r-\theta_t)}{S_{\alpha}(\theta_i-\theta_t)}\frac{k_z^i-k_z^t}{k_z^i+k_z^t} \tag{3}$$

en donde $\alpha=1$ para polarización s y $\alpha=2$ para polarización p, las funciones $S_{\alpha}(\theta)$ son los elementos de matriz diagonales de la matriz de esparcimiento de una esfera, con θ como ángulo de esparcimiento, k_z^i , k_z^t y k_z^r son las relaciones de dispersión de los haces incidente, transmitido y reflejado, respectivamente, dadas en términos del índice de refracción efectivo. Estas fórmulas son el resultado principal de este trabajo y las cuales tienen un sentido físico muy atractivo, dado que los ángulos de esparcimiento corresponden precisamente a las direcciones, en donde, por interferencia constructiva, se forman los haces transmitido y reflejado. En el límite de partícula pequeña se recuperan las fórmulas de Fresnel.

(iii) Finalmente, para poder comparar con los experimentos de laboratorio, es necesario tomar en cuenta que la interfaz en el arreglo experimental consiste de un prisma de vidrio de un lado y el coloide [agua + partículas] del otro. Esto requiere de la inclusión, en el formalismo, de las densidades de cargas y corrientes inducidas en la interfaz vidrio-agua. Esto se hizo, sustituyendo en el formalismo, un propagador (función de Green) calculado con la presencia de la interfaz vidrio-agua y repitiendo todo el cálculo. El resultado fue realmente asombroso, porque se obtuvo una fórmula relativamente simple que corresponde a la que en electrodinámica continua de llama la formula de Fresnel de 3 medios, en donde el medio 1 es el vidrio, el medio 2 una capa de agua de ancho 2a y el medio 3 es el coloide [4].

Para finalizar presentamos unos resultados en donde se muestra una muy buena concordancia entre los resultados de la teoría y de unos primeros experimentos realizados en nuestro laboratorio, para un sistema partículas de TiO_2, de 202 nanómetros de radio, dispersas en agua, en interfaz con un prisma de índice de refracción igual a 1.5302.

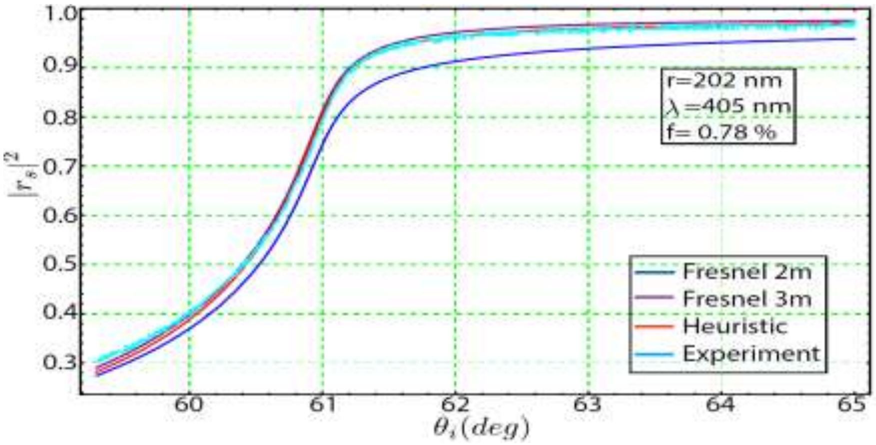

Referencias

[1] H C van de Hulst, *Light Scattering by Small Particles* (Dover, New York, 1981). Cap. 4.
[2] G H Meeten, Meas. Sci. Technol. **8**, 728 (1997).
[3] RG Barrera, A Reyes-Coronado y A García-Valenzuela, Phys. Rev. B **75**, 184201 (2007)
[4] E Gutiérrez-Reyes, A García-Valenzuela y RG Barrera, J. Phys. Chem. B **118**, 6015 (2014)

Inducing forced - and auto- oscillations in one-dimensional photonic crystals with light

J. Eduardo Lugo,[a], Rafael Doti,[a] Noemi Sanchez,[b] Martha Palomino[b] M. B. de la Mora[c], J. A. del Rio[d] and Jocelyn Faubert[a]

[a]*University of Montreal, Visual Psychophysics and Perception Laboratory, School of Optometry, C.P. 6128 succursale Centre Ville, Montreal H3C3J7, Canada*

[b]*Meritorious Autonomous University of Puebla, Physics and Mathematics Sciences Department, Avenue San Claudio y Río Verde, Col. San Manuel, Puebla 72570, México*
[c]*CCADET, Universidad Nacional Autonoma de Mexico, Circuito Exterior S/N, Ciudad Universitaria, Mexico, DF.*

[d]*Instituto de Energıas Renovables, Universidad Nacional Autonoma de Mexico, Temixco 62580, Morelos, Mexico.*

We induced forced and auto-oscillations in one-dimensional photonic crystals (1-D- PCs) with localized defects when light impinges transversally to the defect layer. The photonic structure used consists of a microcavity-like structure formed of two 1-D-PCs made of free-standing porous silicon, separated by a variable air gap (the defect) and the working wavelength is 633 nm. The force generation was made evident by driving a laser light by means of a chopper; the light hit the photonic structure and induced a vibration and the vibration was characterized by using a very sensitive vibrometer. For example, this photonic configuration creates forces of hundredth of nNewtons with 8.3 mW of optical power. That is at least 500 times higher than conventional Optical Tweezers.

Sesión 2

Composition dependence of the crystalline-to-amorphous phase transformation of vanadate compounds in the CdO-V_2O_5 binary system

R. Lozada-Morales[1*], L. Aquino-Meneses[1], S. Jiménez-Sandoval[2], Ma. E. Zayas[3], O. Zelaya-Angel[4], M. Becerril[4], J. Carmona-Rodriguez[5]

[1] *Benemérita Universidad Autónoma de Puebla. Postgrado en Física Aplicada. Facultad de Ciencias Físico-Matemáticas. Av. San Claudio y Av. 18 Sur, Col. San Manuel, Ciudad Universitaria, Puebla, Pue. C. P. 72570, Mexico.*

[2] *Centro de Investigación y de Estudios Avanzados del IPN, Unidad Querétaro, Apartado Postal 1-798, Querétaro, Qro. 76001, Mexico.*

[3] *Departamento de Investigación en Física de la Universidad de Sonora, Edificio 3I, Blvd. Edifício 5 E, Luís Encinas s/n, Col. Centro, 83000. Hermosillo, Sonora, Mexico.*

[4] *Departamento de Física, Centro de Investigación y de Estudios Avanzados, P.O. Box 14-740, México 07360 D. F., Mexico.*

[5] *Instituto de Física y Matemáticas, Universidad Tecnológica de la Mixteca, Carretera a Acatlima Km. 2.5 Huajuapan de León, Oax., México C.P. 69000.*

By mixing different molar concentrations of V_2O_5 and CdO as reactants, and using the melt-quenching method, an evolution from crystalline vanadate compounds to amorphous materials was produced. For chemical compositions with high mol% of V_2O_5, crystalline phases with the sequence V_2O_5, CdV_2O_6, and $Cd_2V_2O_7$ were synthesized. On the other hand, high mol% of CdO led to the formation of amorphous materials. The identification of the crystalline and amorphous phases was carried out by X-ray diffraction and Raman scattering experiments. From optical absorption data, the optical band gap was determined with values between 1.97 and 2.83 eV. Dark conductivity measurements from room temperature to 450 K were made for the whole set of samples. In all cases thermally activated transport was observed. By scanning electron microscopy, depending on the mol% of the reactants, different morphological structures for each crystalline and amorphous material were recorded.

*Corresponding author. Tel.: +52 222 2295500, Fax: +52 222 2295636

E-mail address: rlozada@fcfm.buap.mx (R. Lozada-Morales)

The zone formation of glass in the CdO-TeO_2-GeO_2 system

Ma. E. Zayas[1], D. A. Rodriguez-Carvajal[2], J. Alvarado-Rivera[3]

[1]Departamento de Investigación en Física, Universidad de Sonora, Hermosillo, Sonora, 83000, México.
[2]Departamento de Física, Universidad de Sonora, Hermosillo, Sonora, 83000, México.
[3]Cátedras Conacyt at Departamento de Física, Universidad de Sonora, Hermosillo, Sonora, 83000, México

---

1. Introduction

Research in the glass formation area of new ternary systems containing TeO_2 and GeO_2 is important for the fabrication of new transparent optical materials with good transmittance in the infrared range[1,2]. In addition, ternary systems like ZnO-TeO_2-GeO_2 and WO_3-TeO_2-GeO_2 are of interest not only from fundamental but from a practical point of view regarding the simultaneous use of two glass-former oxides in it. A study of glass formation in the multicomponent PbF_2-PbO-TeO_2-GeO_2 was made by Y. Ivanova[3] for its potential application in infrared optics. On the other hand it has been reported that amorphous CdO-GeO_2 thin films with semiconductor properties can be obtained[4]; and also there are stable glass formation in the binary TeO_2-GeO_2 system[5]. The purpose of this paper is to determine the glass formation area in the new ternary CdO-TeO_2-GeO_2 system.

2. Materials and methods

The original batches were prepared by mixing appropriate amounts of reagent grade oxides from Sigma Aldrich with a purity of 99.999 %: CdO, TeO_2 and GeO_2. The starting compositions of the 36 sample are shown in Table I.

The components were melted into a high alumina crucible in an electrically heated Thermolyne furnace model 46100 in an air atmosphere. Fusion temperature was varied in the range of 900-1350 °C, depending on glass composition. The vitrification of mixtures was achieved by quenching or rapid cooling of the melt on a stainless-steel mold, preheated near the glass transition temperature. After quenching, the glasses were annealed at 300 °C for 2h.

3.Results and discussions

Glass formation zone

Two kind of vitreous samples were obtained: namely transparent glass and partly crystallized glass (Fig. 1). The melting conditions for these samples led to a typical high volatility and to low viscosity due to the specific behavior of cadmium and tellurium oxide, which affects the final composition of glass.

Table I. Original batch compositions % wt of all fabricated glass samples.

Sample	GeO_2	TeO_2	CdO
1	80	10	10
2	70	10	20
3	60	10	30
4	50	10	40
5	40	10	50
6	30	10	60
7	20	10	70
8	10	10	80
9	70	20	10
10	60	20	20
11	50	20	30
12	40	20	40
13	30	20	50
14	20	20	60
15	10	20	70
16	60	30	10
17	50	30	20
18	40	30	30
19	30	30	40
20	20	30	50
21	10	40	60
22	50	40	10
23	40	40	20
24	30	40	30
25	20	40	40
26	10	40	50
27	40	50	10
28	30	50	20
29	20	50	30
30	10	50	40
31	30	60	10
32	20	60	20
33	10	60	30
34	20	70	10
35	10	70	20
36	10	80	10

Figure 2 shows the glass formation region located into the ternary triangle for the CdO-TeO_2-GeO_2 system. The transparent glass formation region is indicated as a light green area near the 100% of TeO_2 and GeO_2 while the partly crystallized region is indicated as a dark green area. The glass formation area for the batches investigated here is wide. The system is constituted by two formers oxides and one modifier oxide, however we can see on the three corners of the Gibbs Triangle there are formation of glass. Normally that behavior is not expected; in fact the corner of the modifier oxide (CdO), with low contents of Tellurium and Germanium oxides also forms both transparent and partially transparent glass with yellow colorations.

The conventional concept of glass structure composed of a random special network of GeO_4 tetrahedra and --

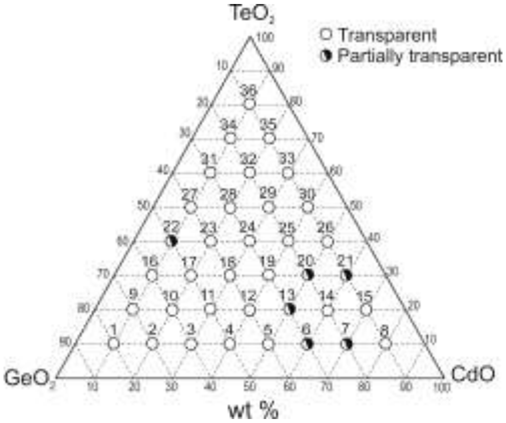

Figure 1. Glasses obtained in the CdO-TeO_2-GeO_2 system.

TeO_4 (tbp), whose interstice are filled with the network modifier cation, cannot be sustained in this case. It is suggested that the dominant cation Cd^{2+} form the network and that the interstices are occupied by Ge^{4+} and Te^{2+} cations. The function of the Ge^{4+} and Te^{2+} ions apparently are to distort the highly polarizable Cd^{2+} ion enough to form a random network[6]. It appears to be possible that Cd^{2+} can form the network in six-fold coordination. Visibly homogeneous glasses of a light emerald green, yellow and clear glass were obtained. The visible coloration in the 36 glasses varies from colorless, clear yellow, yellow, brown-orange and green-yellow.

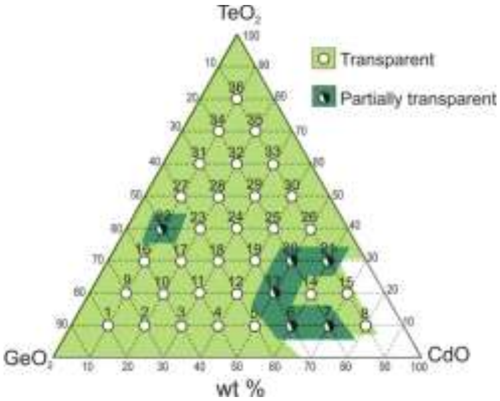

Figure 2. Areas of glass formation in the CdO-TeO_2-GeO_2 system.

X-ray diffraction

Diffraction patterns for transparent glasses are shown in Figure 3 a) and b). These glasses correspond to the composition range of 10-50 CdO, 40-80 TeO_2 and 10-40 GeO_2 (wt %). In general, the patterns show a broad band at about 2θ = 17-35°, corresponding to a long range disordered structure. However, the samples 26 and 30 display well defined peaks. Sample 26 shows the most intense peak and it is located at 2θ = 31.8° which corresponds to Cd_3TeO_6 (cadmium ortotellurate) monoclinic phase (JCPDS 76-1007). Sample 30 shows a peak at 2θ = 33.1° which is related with CdO cubic phase (Monteponite, JCPD 75-0591). Both samples contain the higher proportions of CdO of this series of glasses. From, the

TeO_2 rich glass Gibb’s triangle zone, these samples (26 and 30) are the only ones that present crystallization.

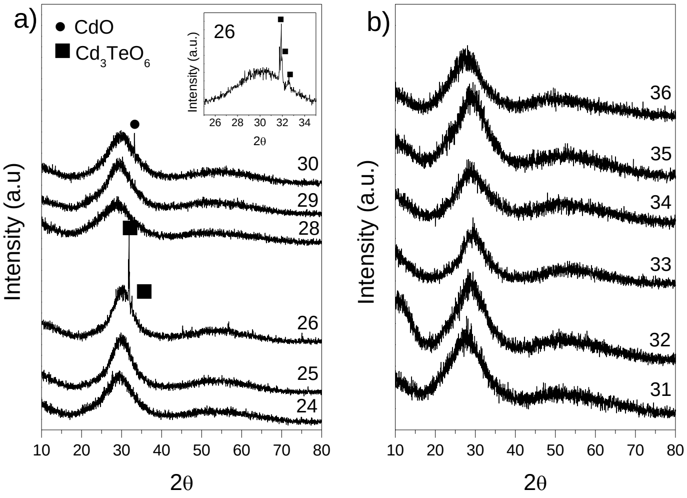

Figure 3. XRD diffraction patterns of the selected area of Gibbs triangle a) samples 24 to 30, with medium TeO_2 content; and b) samples 31 to 36 with the highest content of TeO_2.

Conclusions

The glass formation area of the $CdO-TeO_2-GeO_2$ system has been determined. Transparent and partially crystallized glasses were obtained. This glass formation zone covers a large zone of the Gibbs triangle even at high contents of cadmium oxide. A transparent orange glass with a composition of $80CdO.10TeO_2.10GeO_2$ was possible to obtain. XRD analysis revealed that the glass with $50CdO.40TeO_2.10GeO_2$ presented the formation of Cd_3TeO_6 (cadmium orthotellurate) crystalline phases.

References

1.G. Upender, C.P. Vardhani, S. Suresh, A.M. Awasthi, V. Chandra Mouli, Structure, physical and thermal properties of WO3–GeO2–TeO2 glasses, Materials Chemistry and Physics 121 (2010) 335–341.

2.G. E. Rachkovskaya and G. B. Zakharevich, germanate lead-tellurite glasses for optical light filters, Glass and Ceramics, Vol. 68, Nos. 11 – 12, March, 2012.

3. Y. Ivanova Glass formation in the $PbO-PbF_2-TeO_2-GeO_2$- system Journal of material science letter 10(1991) 1309-1311.

4.Satoru Narushima, Masahiro Orita and Masahiro Hirano, Hideo Hosono Electronic structure and transport properties in the transparent amorphous oxide semiconductor 2 CdO"GeO2 Physical Review B **66**, 035203 (2002).

5. E. Kashchieva, Dissertation, Sofia (1984).

6. BH. V. Janakirama Rao, Journal of the American Ceramic Society Vol 45 Issue 11 page 555-563 November 1962. Dielectric properties of glasses in the systems $Bi_2O_3-CdO-SiO_2$, $Bi_2O_3-CdO-B_2O_3$ and $Bi_2O_3-CdO-GeO_2$ and their relation to the structure of glass.

Posters I

Photoluminescence and electro-optical characterization of Nd-doped (ZnV_2O_6, $Zn_2V_2O_7$)

Y. A. González-Rivera[a], L. Aquino-Meneses[a], R. Lozada-Morales[a]*, **A. Maldonado-García[a]***, S. Jiménez-Sandoval[b], E. Rubio-Rosas[c], O. Zelaya Angel[d], and F. Rodriguez-Melgarejo[b]

[a]Benemérita Universidad Autónoma de Puebla. Postgrado en Física Aplicada. Facultad de Ciencias Físico-Matemáticas, Av. San Claudio y Av. 18 sur, Col. San Manuel Ciudad Universitaria, Puebla, Pue. C. P. 72570, Mexico.
[b]Centro de Investigación y de Estudios Avanzados del IPN, Unidad Querétaro, Apartado Postal 1-798, Querétaro, Qro. 76001, Mexico.
[c]Centro Universitario de Vinculación y transferencia de Tecnología, Prol. De la 24 Sur y Av. San Claudio, Col. San Manuel, Puebla, Mexico.
[d]Departamento de Física, Centro de Investigación y de Estudios Avanzados, P.O. Box 14-740, México 07360 D. F., Mexico.

By using the melt-quenching method, ZnV_2O_6 and $Zn_2V_2O_7$ vanadate compounds were prepared and simultaneously doped with Nd^{3+}. X-ray diffraction patterns indicate the polycrystalline character of both materials, which are acting as a matrix of Nd^{3+}. The crystallinity of the two vanadate compounds was also verified by Raman scattering, where different vibrational modes assigned to ZnV_2O_6 and $Zn_2V_2O_7$ were detected. The analysis of electron dispersive spectroscopy shows an homogeneous doping of Nd throughout the ZnV_2O_6 and $Zn_2V_2O_7$ host materials, of the order of 1.0 ± 0.2 at %. The micrographs acquired by Scanning Electron Microscopy, show that Nd-doped ZnV_2O_6 is constituted of microrods and irregular crystalline blocks. In the case of Nd-doped $Zn_2V_2O_7$, only irregular crystalline blocks were observed. The band gap energy was calculated from optical absorption data, the values were $E_g = 1.85$ and, $E_g = 2.58$ eV for ZnV_2O_6:Nd and $Zn_2V_2O_7$:Nd, respectively. By means of two points dark conductivity measurements, values in the 10^{-4}-10^{-6} $(\Omega\ \mathrm{cm})^{-1}$ range for ZnV_2O_6:Nd and in the 10^{-6}-$10^{-8}$$(\Omega\ \mathrm{cm})^{-1}$ range for $Zn_2V_2O_7$:Nd were registered. By photoluminescence, multiple emissions assigned to electronic

transitions of Nd^{3+} ion were detected. For instance, in Nd-doped ZnV_2O_6, $\{^4F_{5/2}, ^4F_{3/2}\} \rightarrow {}^4I_{9/2}$ electronic transitions, were observed. Concerning to Nd-doped $Zn_2V_2O_7$, $\{^4G_{7/2}, ^4F_{7/2}, ^4F_{5/2}, ^4F_{3/2}\} \rightarrow {}^4I_{9/2}$ electronic transitions were identified. All these results suggest that a successful doping of vanadates was obtained by the melt-quenching growth technique.

Experimental. With the aim to get predominantly crystalline phases of ZnV_2O_6 and $Zn_2V_2O_7$ compounds, a mixture of 50-50 mol % and 66.7-33.3 mol % of ZnO (Sigma-Aldrich) and V_2O_5 (Sigma-Aldrich) reactants respectively, were prepared,[4]. A 2 mol % of the reactive Nd $(NO_3)_3$ $5H_2O$ (powder Sigma-Aldrich) was aggregated in order to provide Nd^{3+} ions to each vanadate. Afterwards, the mixtures were melted at 1000°C. Then, suddenly cooled down to 650°C for the Nd-doped ZnV_2O_6 and 800°C for Nd-doped $Zn_2V_2O_7$. The mixtures were kept at these respective temperatures during two hours. Subsequently, the resultant samples were slowly cooled until room temperature.

The fabrication process for the studied samples was carried out in an electrical thermoline furnace model 4800, using porcelain ceramic crucibles. The X-ray diffraction patterns were acquired in a Siemens D500 diffractometer by using the CuK_α line. The electron dispersive spectroscopy (EDS) analysis was recorded in a Jeol LSM-6610LV Scanning Electron Microscope. In the same device, Scanning Electron Microscopy (SEM) images in the scale of microns were recorded. The energy band gap (E_g) for each sample was determined from optical absorption (OA) spectra, which was acquired by using a Cary 100 Varian spectrometer. The dark conductivity (DC) measurements were carried out in a conventional apparatus from GMW Magnet System model 3472-20.

The photoluminescence and Raman spectra were obtained at room temperature in a Dilor LabRam micro spectrometer equipped with a Si CCD detector and an Ar^+ laser, emitting at 514.5 or 488.0 nm, as excitation sources.

Raman and FT-IR spectroscopic characterization of glasses with high TeO_2 content

I.V. García Amaya[1], Ma. E. Zayas[2], J. Alvarado-Rivera,[3] B. Manzanares-Martínez,[2]
and R. Lozada-Morales
[1] *Departamento de Física, Universidad de Sonora, Hermosillo, Sonora, 83000, México.*
[2] *Departamento de Investigación en Física, Universidad de Sonora, Hermosillo, Sonora, 83000, México.*
[3] Cátedras Conacyt Departamento de Física, Universidad de Sonora, Hermosillo, Sonora, 83000, México

1. Introduction

Glasses doped with rare earth ions, with numerous applications in the field of luminescence, have been extensively studied over the past few decades due to their potential technological and commercial applications. For instance, they can be use as efficient lasers where the upper lasing level should have a lifetime as large as compared to the optical pumping time, and the fluorescence band width should be small. On the other hand, for optical imaging purposes, lifetime of the luminescent level should be small so that the rapidly changing images can be recorded with good contrast [1-2]. Tellurite oxide glasses are very good candidates for these applications, it can accept large concentration of RE ions; exhibit large transmittance window from the visible to the infrared region, have low cut off phonon energy 700 cm^{-1}, present high refractive index ≈2.0 and show high chemical stability [3].

2. Materials and methods

The glasses were fabricated using zinc oxide (ZnO, Fluka Analitycal), cadmium oxide (CdO, 99.5%), tellurium dioxide (TeO_2 ≥99%) and europium nitrate hexahidrate ($Eu(NO_3)_3 \cdot 6H_2O$, 99.99%) from Sigma Aldrich. The powders were weighted in an OHAUS analytical weighting scale, model GA110 with a precision of 0.0001 g.

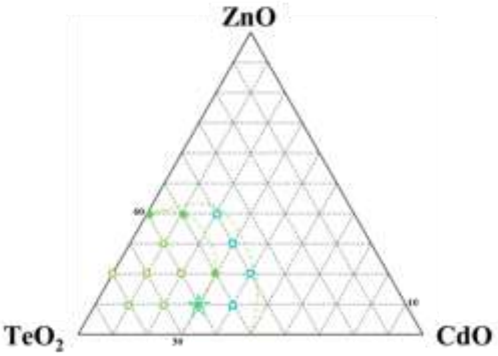

Figure 1. *The ternary ZnO–CdO–TeO_2 composition system.*

In the Table I the nominal composition of the mixtures is presented. These compositions were determined on the basis of the CdO-ZnO-TeO_2 system glass formation area study by Zayas *et. al.* [4]. For this series of glasses doped whit Eu^{3+}, five compositions corresponding to partially devitrified glass were chosen. The glasses were fabricated by the melt-quenching method in high alumina crucibles at 1000°C in a Thermolyne 48000 furnace with a dwell time of 30 minutes. After quenching, the glasses were annealed at 350°C for 30 minutes and let it cool to room temperature inside the oven.

Table 1. *Batch compositions (wt%) of ZnO–CdO–TeO$_2$.*

Label	ZnO	CdO	TeO$_2$	Eu(NO$_3$)$_3$·6H$_2$O
			(%mol)	
V1	17	32	51	0.3
V2	17	32	51	0.6
V3	17	32	51	0.9
V4	17	32	51	1.2
V5	17	32	51	1.5

3. Results and discussions

3.1. DRX

In Figure 2 diffraction patterns of all glasses are presented. All samples shown an amorphous structure evidenced by the a broad band localized in the range of 2θ from 20° to 40°, indicating the presence of structural ordering or several small crystallizations [5]. It is interesting to observe that the band has a well-defined maximum position at $2\theta = 29.7°$ [6].

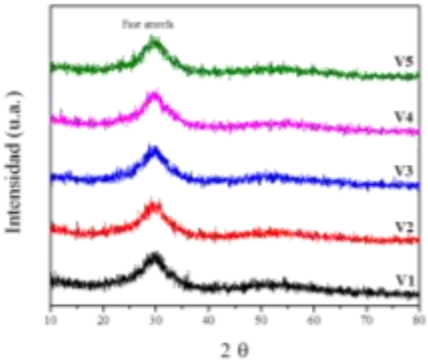

Figure 2. *Diffraction patterns of all fabricated glasses. It can be seen that all the samples are amorphous.*

3.2. FT-IR

The infrared spectra of the glasses in the range of 1200 to 370 cm^{-1} are displayed in Figure 3. A broad absorption band appears in the range of 870-520 cm^{-1} with its minimum at 676-674 cm^{-1}, and it is assigned to asymmetric stretching vibrations of Te-O bonds of TeO$_3$ trigonal pyramids units. Moreover, a less intense absorption band appears for all glasses, in the range of 500 to 400 cm^{-1}. It presents a shift to higher frequencies of 435 to 442 cm^{-1} that can be attributed to stretching vibrations of Cd-O bonds [7]. At low wavenumber values there are small absorption peaks for V3, V4 and V5 located at 420 – 410 cm^{-1} corresponding to ZnO$_4$ units [8].

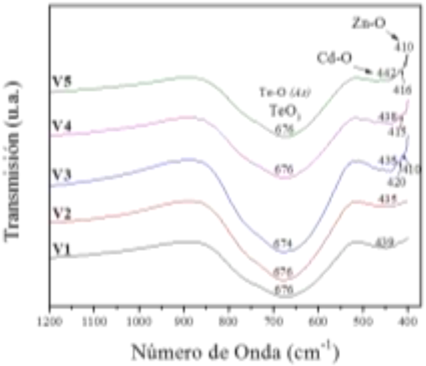

Figure 3. *Infrared spectra of the fabricated glasses of the ZnO-CdO-TeO_2 with different Eu^{3+} ions content.*

3.3. RAMAN

In general, raman spectra of all glasses present a similar behavior among them, as it can be seen in Figure 4. The first two bands at low raman frequencies of 114 and 345 cm^{-1}, are assigned to the oscillations of Te-O bonds in TeO_4 tetrahedra characteristic of α-TeO_2 [9-10].

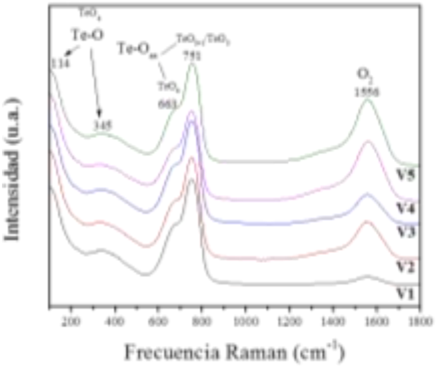

Figure 4. *Raman spectra of the ZnO-CdO-TeO_2 with different Eu^{3+} ions content.*

In the case of the bands located at 663 and 751 cm^{-1}, they are related to stretching vibrations of TeO_{ax} in groups TeO_4 and TeO_3/TeO_{3+1}, respectively [11-13]. The absorption band at 663 cm^{-1} corresponds to vibrations in tbp of TeO_4 groups that constitute the continuous network [4]. A. Jha *et al.* [14] reported that this band corresponds to a strong crystallization band of α-TeO_2 localized around 670 cm^{-1}. The band at 751 cm^{-1} is generated by $[TeO_{3+1}]^{4-}$ and $[TeO_3]^{2-}$ units [15]. These structural changes in the glass matrix are induce by the introduction of ZnO and CdO that produce the breakdown of Te-O-Te bonds [4,16]. These results are in agreement with the FT-IR analysis where TeO_4, TeO_3/TeO_{3+1} groups where identified. Furthermore, there is an absorption band at 1556 cm^{-1} that increases in intensity as the Eu^{3+} ions concentration raises, that corresponds to the Q rotational-vibrational band of O_2 in air [17]. In the tellurate glasses, the molecular oxygen it is most likely to be produced during glass fabrication. The change in oxidation state of Te from TeO_4 to TeO_3 produces structural voids around it, increasing the interstitial space in the glass matrix [18]. We consider that in our glasses the TeO_4 or TeO_3 units are sharing two O atoms, which form a OTe(OO)TeO bridge [19-20] and the possible cause of of O_2 generation.

4. Conclusions

For all europium ions content, green and visible transparent homogeneous glasses were obtained. XRD analyzes confirm the presence of amorphous phases. FT-IR and Raman spectra show that TeO_{3+1}/TeO_3 groups are the predominant structural units. Thus is a large proportion of NBO present in the glass matrix. These changes are induced in the glass network by breaking Te-O-Te bonds caused by the addition of ZnO and CdO. In Raman spectra an unusual band characteristic of molecular oxygen was detected, which probably formed during fabrication. In this regard it is suggested that TeO_{3+1}/TeO_3 units form OTe(OO)TeO bridges sharing two oxygen atoms.

5. References

1. A. Kumar, et. al., *Spectrochimica Acta Part A*, no. 58, p.p. 2115–2125, 2002.
2. K. Maheshvaran and K. Marimuthu, *Journal of Luminescence*, no. 132, p.p. 2259–2267, 2012.
3. W. Stambouli, et. al., *Journal of Luminescence*, no. 132, p.p. 205–209, 2012.
4. M. E. Zayas et. al., *Physics and Chemistry of Glasses*, vol. 46, no. 1, pp, 46-50, 2005.
5. C. Ruvalcaba et. al., *Journal of the American Ceramic Society*, vol. 96 no. 10, pp. 3084–3088, 2013.
6. M. J. Redman and J. H. Chen, *Journal of the American Ceramic Society*, vol. 50, no. 10, pp. 523-525, 1967.
7. P. Gayathri Pavani et. al., *Optical Materials*, vol. 34, no. 1, pp. 215 – 220, 2011.
8. P. Gayathri Pavani, et. al., *Physica B: Condensed Matter*, vol. 406, no. 6 – 7, pp. 1242–1247, 2011.
9. V.N. Sigaev, et.al., *Journal of Non-Crystalline Solids*, vol. 279, pp. 136-144, 2001.
10. A.M. Zahra, et. al., *Journal of Non-Crystalline Solids*, vol. 155, pp. 45-55, 1993.
11. V.R. Bandi, et. al., *Journal of the American Ceramic Society*, vol. 92, no. 12, pp. 2953 – 2956, 2009.
12. Y. Dwivedi and S. B. Rai, *Journal of the American Ceramic Society*, vol. 93, no. 3, pp. 727 – 731, 2010.
13. G. E. Rachkovskaya and G. B. Zakharevich, *Journal of Applied Spectroscopy*, vol. 74, no. 1, pp. 86-89, 2007.
14. A. Jha, et. al., *Physical Review B*, vol. 62, no. 10, pp. 6215-6227, 2000.
15. G. Upender, et. al., *Materials Chemistry and Physics*, no. 121, pp. 335–341, 2010.
16. A. Kaur, et. al., *Journal of Non-Crystalline Solids*, vol. 356, pp. 864-872, 2010.
17. S. Agnello, et. al., *Journal of Applied Physics*, vol. 114, 104305, 2013.
18. C. R. Pulluru, et. al., *Applied Physics Letters*, vol. 87, pp. 91 – 107, 2005.
19. L. Skuja, et. al., *Journal of Applied Physics*, vol. 83, no. 11, pp. 6106 – 6110, 1998.
20. L. S. Wang, et. al., *Journal. Physics Chemistry*. 100, 8697-8700 (1996).

Photoluminescence in Er-doped V_2O_5 and Er-doped CdV_2O_6

Y. A. González-Rivera[a], E. Cervantes-Juárez[a], L. Aquino-Meneses[a], R. Lozada- Morales[a]
[a]*Benemérita Universidad Autónoma de Puebla. Postgrado en Física Aplicada. Facultad de Ciencias Físico-Matemáticas, Av. San Claudio y Av. 18 sur, Col. San Manuel Ciudad Universitaria, Puebla, Pue. C. P. 72570, Mexico.*

A group of samples from the CdO-V_2O_5 binary system, particularly with high V_2O_5 content, doped with Er^{3+} were prepared. The set of samples was fabricated using the conventional melt-quenching method. Depending on the proportion of the used reactants, the existence of V_2O_5 and of CdV_2O_6 was identified from X-ray diffraction measurements and Raman spectroscopy. Depending on the relative concentrations of CdO and V_2O_5, different types of morphologies for each sample were found in a scanning electron microscope. Their chemical composition was measured from energy dispersive spectroscopy in the same instrument. An effective Er-doping of the order of 1.0 ± 0.35 at.% was found for each sample. From optical absorption data, the composition dependent optical band gap was determined with values between 1.94 and 2.29 eV. Finally, photoluminescence experiments showed, in the samples with the highest V_2O_5 content, wide bands associated to oxygen vacancies. For the rest of the samples emissions from electronic transitions of Er^{3+} ions were detected.

Introduction. The family of vanadate compounds has attracted the attention because structures of different dimensions and shapes can be generated with this type of compounds. These include nanocolumns, nanowires, nanotubes and nanorods. As regards their possible technological applications, physical and chemical properties of these materials have been exploited in the development of chemical sensors, cathode materials in batteries, switching devices, thermoelectric catalytic materials, among others. Beside stoichiometric and crystalline vanadate compounds, glasses based on CdO-V_2O_5 binary system have also been studied because of their interesting optical and electrical properties. There is a wide range of potential technological applications around these types of layered materials in which the insertion of distinct metallic ions within the layered structure allows tailoring their physical properties.

In this work, two types of luminescent effects were observed. One of them due to oxygen vacancies, ascribed to samples that contain mostly Er-doped V_2O_5. The second type was emission due to electronic transitions between levels of Er^{3+} ions immersed in the crystalline network of CdV_2O_6.

Experimental. By mixing different proportions in weight (wt.%) of CdO (Sigma-Aldrich 99.9%) and V_2O_5 (Sigma-Aldrich 99.6%) reactants, a batch of 7 samples was prepared. The synthesis for each sample was carried out by using the conventional melt-quenching method in porcelain crucibles in the 800-1200 °C range, depending on their chemical composition. The melting was poured in a stainless steel container in which a thermal shock was produced. The samples were labeled in concordance to the wt.% of used reactants, that is, the V_2O_5 wt. %, followed by the CdO wt. %. Thus, the labels of the samples are: M1 → (100% - 0%); M2 → (95% - 5%); M3 → (90% - 10%); M4 → (80% - 20%), M5 → (75% - 25%); M6 → (70% - 30%); M7 → (65% - 35%). Additionally, of the total composition, for all samples 5 wt. % of $Er(NO_3)_3$*$5H_2O$ (powder Sigma Aldrich) was aggregated to the V_2O_5-CdO mixture, prior to melting, as source of Er^{3+} ions. In this case, the interval of wt. % of the starting reactants was not varied beyond the above mentioned values because in a previous work, the photoluminescent properties in Er-doped samples with high CdO content in the same CdO-V_2O_5 system was reported.

Conclusions. By the melt quenching method a batch of samples based on the V_2O_5-CdO binary system was synthetized and doped with Er^{3+} ions. In the selected range of wt. % of starting reactants, Er-doped V_2O_5, Er-doped CdV_2O_6, and a mixture of them were produced. This was verified by X-ray diffraction and Raman spectroscopy. By optical absorption, E_g values in the 1.94 - 2.29 eV interval for this series of samples were found. For samples that are predominantly formed by Er-doped V_2O_5, bands of PL associated to OV located at 650 and 730 nm were observed. On the other hand, for samples particularly including Er-doped CdV_2O_6, PL associated to distinct electronic transitions of Er^{3+} was dominant. Some of those electronic transitions present sharp and narrow emissions, and their number is augmented when the CdV_2O_6 content in the samples is larger. In this way, it has been shown that CdV_2O_6 is an efficient host matrix for luminescent Er^{3+} ions. Finally, it was also found that samples with lamellar plates microstructure emit PL associated to oxygen vacancies in V_2O_5.

Analysis of vanadate compounds and Glasses from the Cu-CdO-V2O5 ternary system

E. Cervantes Juárez, R. Lozada-Morales

Facultad de Ciencias Físico-Matemáticas de la Benemérita Universidad autónoma de Puebla

It has been of great interest the research of glassy materials of vanadates due to the advantages for generating different structural groups, and their capability as host of different metallic ions, providing wide versatility of structural, optical and electrical properties in the resulting materials [1-6]. As an example, from vanadium oxide it has been demonstrated that it is possible to obtain nanostructures such as nanotubes, nanorods and nanospikes [7-9]. And even it is possible to fabricate glasses containing CuO and V2O5 which are of large interest due to their electrical and magnetic properties [10-11].

The original contribution of this work is to report a wide and unusual GFA in the Cu-CdO-V_2O_5 ternary system.

A batch of 23 compositions were prepared starting rom CdO (Sigma-Aldrich 99.99%), and V2O5 (Sigma-Aldrich 99.60%) Cu powders (Fermont 99.80 %). The melting process for each sample was carried out by using a conventional melting melt-quenching method in porcelain crucibles in the 800 – 1200 °C range depending on their chemical composition.

The samples were tagged in concordance to the wt % of the used reactants. Thus, the numbers separated by dashes in the tag, for each glass, correspond to wt.-% of: Cu, CdO, and V2O5 respectively.

Before fabrication of samples, depending on the proportion in weight of the used reactants the diagram of compositions was divided in three regions. Region I was established for samples with higher CdO content, region II was organized for samples whose glass former (V_2O_5) content is the highest and finally region III was planned for samples with the highest Cu content. After fabrication of samples, in region I two types of materials were found, that is, within this region only amorphous materials were observed. Meanwhile, on the perimeter that surrounds such glass formation area, crystalline compounds like $Cd_2V_2O_7$, and mixtures of phases of $CuCd(VO_4)$, Cu_2O, and CdO, were found.

The crystalline state for each synthesized sample was determined by X-ray diffraction (Fig.1) and corroborated by Raman spectroscopy (Fig. 2).

References

[1] G.I. Petrov, V. V. Yakovlev, J. Squier, Appl. Phys. Letters 81 (6) (2002) 1023-1025.

[2] D. Ilieva, V. Dimitrov, Y. Dimitriev, G. Bogachev, Phys. Chem. Glasses 40 (1) (1999) 6-11.

[3] Y. Dimitriev, V. Dimitrov, M Arnaudov, and D. Topalov, J. Non-Crytalline Solids 57 (1983) 147-156.

[4] M.M. El–Desoky, M.S. Al-Assiri, Mat. Sci. and Engineering B 137 (2007) 237-246.

[5] J.E. Garbarczyk, M. Wasiucionek, P. Machowski, W. Jakubowski, Solid State Ionics 119 (1999) 9-14.

[6] G.M. Clark and A.N. Pick, J. Thermal Anal. 7 (1975) 289-300.

[7] C. O’ Dwyer V. Lavayen, S.B. Newcomb, M.A. Santa Ana, E. Benavente, G. Gonzalez, and C.M. Sotomayor Torres, J. Electrochem. Soc, 154 (8) (2007) k29-k35.

[8] Xueqin Liu, Chunming Huang, Jiawen Qiu, Yinyue Wang, Appl. Surf. Sci., 253 (2006) 2747-2751.

[9] A.G. Souza Filho, O. P. Ferreira, E. J. G. Santos, J. Mendes Filho, and O. L. Alves, Nano Letters 4 (11) (2004) 2099- 2104.

[10] M.S. Al-Assiri, Physica B 403 (2008) 2684-2689.

[11] I.S. Yahia, Y.B. Saddeek, G.B. Sakr, W. Knoff, T. Story, N. Romcevic, W. Dobrowolski, J. Magn. Magn. Mater. 321 (2009) 4039-4044.

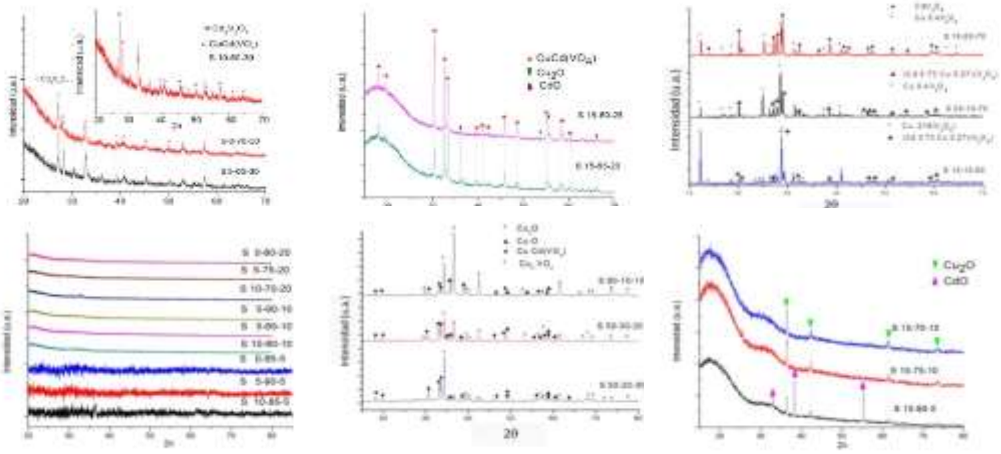

Fig. 1.X-ray diffraction patterns

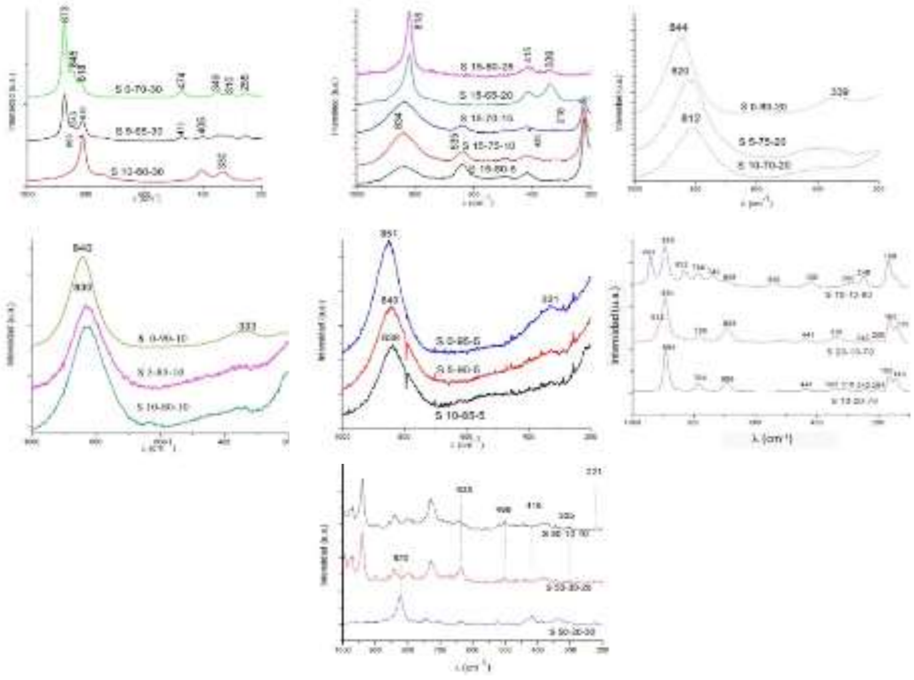

Fig. 2.Raman spectra

Synthesis and Luminiscence Characterization of $Li_2B_4O_7$ Doped with Manganese and Europium

Martín Rodolfo Palomino Merino*, José Eduardo Espinosa Rosales*, Pablo Marco Trejo García*,
Raúl Aceves Torres**
**FCFM, Benemérita Universidad Auntónoma de Puebla, Puebla, México*
*** CIF US, Universidad de sonora, Hermosillo, Sonora, México.*

In the present study, Lithium tetraborate ($Li_2B_4O_7$) doped with manganese (0.5 wt%) and europium (0.3 and 0.5 wt%) have been obtained using as dopant MnCl2 and Eu(NO3)3 respectively. Two types of LiBO were used. The LiBO:Mn:Eu was powdered using an agata morter. Powder X-Ray diffraction patterns were recorded to corroborate the phase purity of the samples synthesized.

The fluorescence´s experiments was realized using a spectometer with double grids Fluorolog FL3-22 (Jobin - Yvon Horiba) in emission mode front face and equipped with a Xe lamp of 450 Watts . The excitation spectra is denoted by "x " and the successsor number indicates the wavelength at which will see. The Emission spectra is denoted by "m" and the successor number represent the excitation wavelength .

RESULTS AND DISCUSSION

Powder X-ray diffraction (XRD)patterns were recorded in an X-Ray Bruker D8 Discover Diffractometer, to corrobórate the phase purity of the samples synthesized. The slow scan was performed in the 2θ range from 15-80° with a scan step of 0.040°. The results obtained were matched with the standard data available for $Li_2B_4O_7$. The next figures shows the X-ray diffraction pattern of the synthesized Li2b4o7:Mn:Eu.

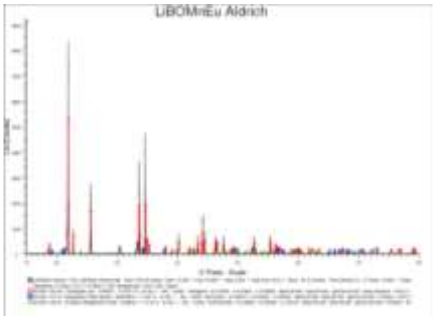

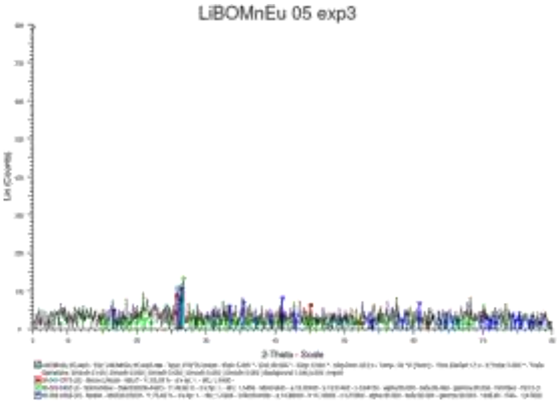

Figures 2 and 3 show emission spectra of LiBO:Mn doped with Eu (05 wt %) using lithium borate (LIBO) from Aldrich. The emission spectrum consists of multiple bands in the range of 350-700 nm with maximums at 398, 405, 408, 414, 417, 439, 566, 613 and 693 nm respectively. In Figure 3 show two bands, these are possibly associated with the emission of europium corresponding to the 613 and 693 nm; these are discussed in (M.M.A. Maqableh, 2014).

In the excitation spectrum, we can observe the presence of a broad band in the range of 280-380 nm and a smaller peak at about 640 nm, these are repeated for any emission wavelength, varying in intensity only.

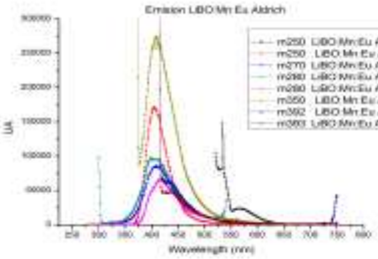

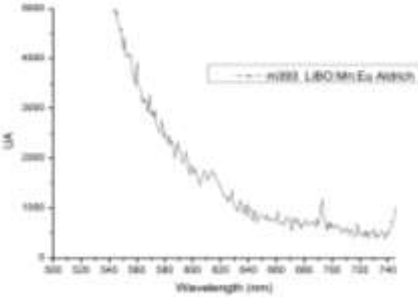

¡Error! No se encuentra el origen de la referencia.

Fig 2

Fig 3

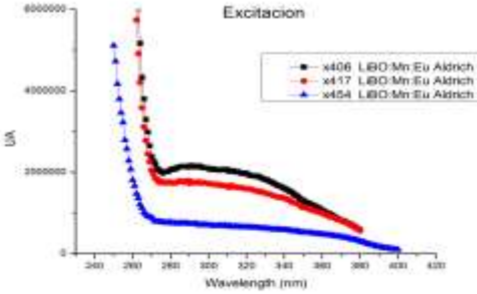

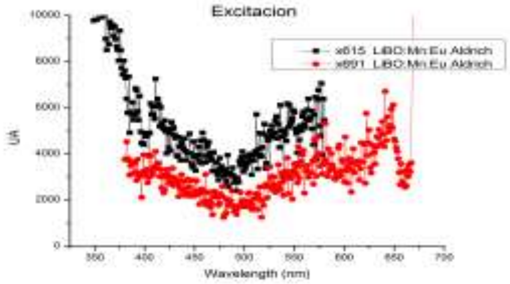

Fig 4

Fig 5

In the following figures are pointed out emission spectras of LIBO:Mn:Eu (0.03 wt % (fig. 6)) and (0.05 wt % (fig. 7)) with terminations m2 and m3 respectively. In this case we use LiBO synthesized in the laboratory. Comparing these spectras with the emission spectra of LIBO:Mn:Eu (LiBO Aldrich), it can be seen that in these, the emission bands at approximately 590 and 610 nm associated with europium does not appear. This fact leads to believe that the europium not properly joined to said sample.

It can be seen that the samples in which has been used LiBO synthesized in the laboratory of FCFM-BUAP, there is no significant difference in the spectras. It is observed in the range of 350-500nm a broad band with two maximums, these are related to LiBO Mn. In the range of 580-620 nm can be observed two bands with maximums at approximately 590 and 610 nm, these are repeated for any excitation wavelength, however, it can be seen two emission bands that are not presented to all wavelengths of excitation, i.e. the band with maximum at about 650 nm appears to m250-m2, m330-m2, m361-m3, m463-m3; and the band with maximum at 700 nm appears only for excitation wavelengths less than 400nm. Finally, in the spectra for m409 Libo:Mn:Eu m3 (Figure 7), it can be seen in the range of 550-700 nm a silhouette, possibly related to one of the emission bands of manganese.

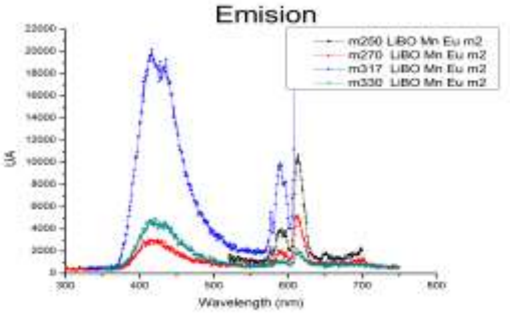

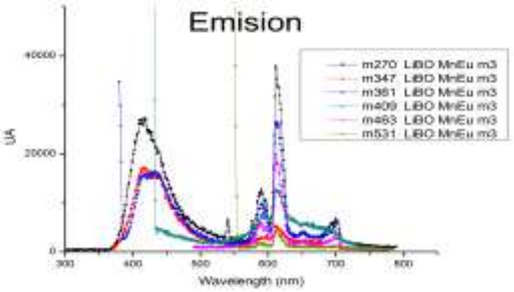

Caracterización mecánica por métodos ultrasónicos de vidrios ZnO-CdO-V_2O_5 dopados con Neodimio y Erbio

B. Manzanares-Martínez[1], E. Cervantes-Juárez[2], R. Lozada-Morales[2], Ma. E. Zayas-Saucedo[1]
[1]Universidad de Sonora, [2]Benemérita Universidad Autónoma de Puebla

Una manera de obtener de forma indirecta los parámetros mecánicos de materiales sólidos de un material tales como: Módulo de Young (E), Módulo de Corte (G), entre otros, es mediante la medición de las velocidades de sonido longitudinal y transversal del material (1) - (2). En las Tablas 1 y 2 están las composiciones de las muestras estudiadas. Como puede observarse en las tablas los porcentajes ZnO, CdO, V2O5 suman 100% a esta le llamamos composición nominal, referido al porcentaje en peso. Para el caso de las muestras de la Tabla 1 el 5% de este total, pertenece al compuesto $Er(NO_3)3{:}5H_2O$. Tal compuesto proporciona los iones Er^{3+}. Con respecto a las muestras de la Tabla 2 el 5% corresponde al compuesto $Nd(NO_3)_3{:}5H_2O$.

Tabla 2. Composición de muestras dopadas con Er.

Muestra	% V_2O_5	% CdO	% ZnO
M1	10	80	10
M2	20	70	10
M3	30	60	10
M4	10	70	20
M5	20	60	20
M6	30	50	20
M7	20	50	30
M8	30	40	30

Tabla 3. Composición de muestras dopadas con Nd.

Muestra	% V_2O_5	% CdO	% ZnO
M1	10	80	10
M2	20	70	10
M3	30	60	10
M4	10	70	20
M5	20	60	20
M6	30	50	20
M7	20	50	30
M8	30	40	30

En las Figuras 1 y 2 se exhiben las densidades de las muestras correspondientes a las Tablas 1 y 2, respectivamente. La medición de las densidades fue realizada mediante el método de Arquímedes utilizando una balanza Ohaus Pioneer de 0.001gr de resolución. Puede observarse que en general las muestras con Neodimio son ligeramente más densas que aquellas dopadas con Erbio. Por otra parte la disminución en el porcentaje de V_2O_5, y el aumento en el óxido de cadmio produce una disminución en la densidad de las muestras.

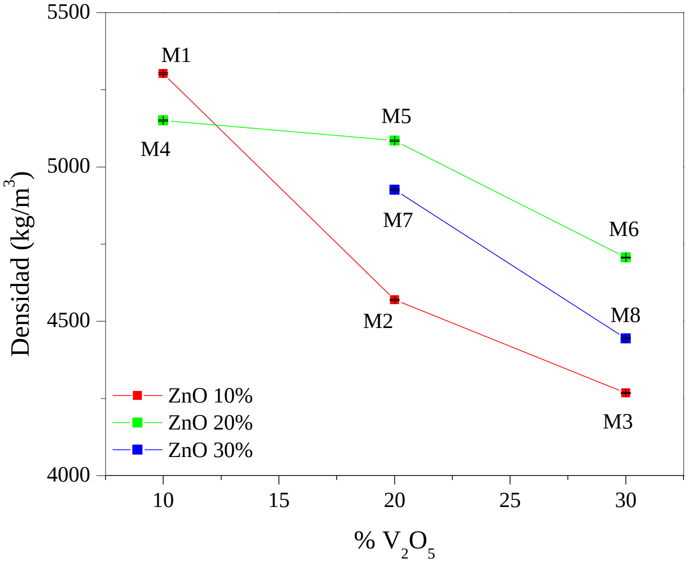

Figura 5. Densidad de las muestras dopadas con Er.

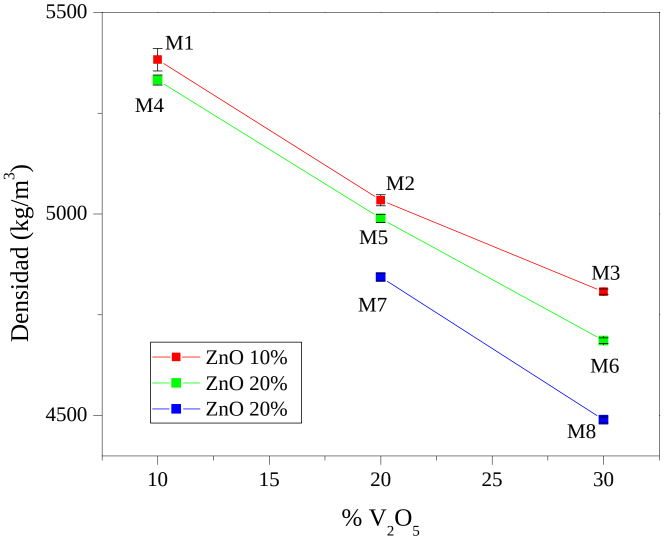

Figura 6. Densidad de las muestras dopadas con Nd.

Para el cálculo de las velocidades de sonido se utilizó la técnica de “Transmisión a través” (Trough-Transmission) con dos transductores de frecuencia central de 10MHz y 0.5 pulgadas de diámetro. Para la medición de la velocidad transversal se utilizó la técnica de pulso eco utilizando un transductor de haz normal de onda de corte de 0,25 pulgadas de diámetro, frecuencia central de 10MHz y línea de retardo integrada. Los resultados de las mediciones ultrasónicas se muestran en las Tablas 3 y 4. Las velocidades de sonido en las muestras con Er son en general ligeramente mayores que en las muestras con Nd, lo cual es consistente con la mayor densidad de las muestras con Er. Para la estimación de las incertidumbres de las velocidades de sonido se utilizó la metodología establecida por CENAM (3), esta cantidad está escrita en la columna denominada "Error" de cada una de las tablas.

Tabla 4. Velocidades de sonido en las muestras dopadas con Er.

Muestra	Velocidad Longitudinal (m/s)	Error (m/s)	Velocidad Transversal (m/s)	Error (m/s)
M1	4401.75	10.24	2347.14	0.37
M2	4621.72	20.31	2447.00	0.24
M3	4626.99	11.23	2537.16	2.12
M4	4477.90	6.73	2361.45	0.25
M5	4301.44	5.46	2257.16	1.18
M6	4313.74	7.66	2264.47	2.59
M7	4452.27	8.28	2327.67	0.61
M8	4464.72	11.94	2384.78	0.34

Tabla 5. Velocidades de sonido en las muestras dopadas con Nd.

Muestra	Velocidad Longitudinal (m/s)	Error (m/s)	Velocidad Transversal (m/s)	Error (m/s)
M1	4250.09	5.78	2283.70	1.11
M2	4329.90	4.74	2233.82	0.73
M3	4191.24	4.94	2202.33	0.83
M4	4528.91	5.41	2322.39	0.66
M5	4297.24	3.32	2297.90	0.87
M6	4180.56	5.25	2261.61	0.79
M7	4322.80	4.97	2375.88	0.36
M8	4296.18	3.00	2370.67	1.20

Para el cálculo de los módulos elásticos utilizaos las siguientes relaciones (4):

$$M = \rho c_l^2 ,$$

$$G = \rho c_t^2 ,$$

$$E = \frac{G(3M - 4G)}{M - G} .$$

El primer módulo *M* es llamado módulo longitudinal, *G* es el módulo de corte y *E* es el módulo de Young.

Puede observarse que el aumento de V_2O_5 en general disminuye el valor de los módulos elásticos en la muestra, con excepción de las muestras con 10% de ZnO en las muestras dopadas con Er, donde se presenta un mínimo de los módulos con 20% de V_2O_5.
El módulo de Young se relaciona a la resistencia a la elongación del material, el radio entre el esfuerzo y la deformación longitudinal en el material (5). Lo cual nos muestra que las muestras en general pierden "dureza" conforme aumenta el porcentaje de V_2O_5. De la misma manera, el módulo de corte, es decir, la resistencia a las deformaciones cizallantes disminuye con el aumento de V_2O_5.

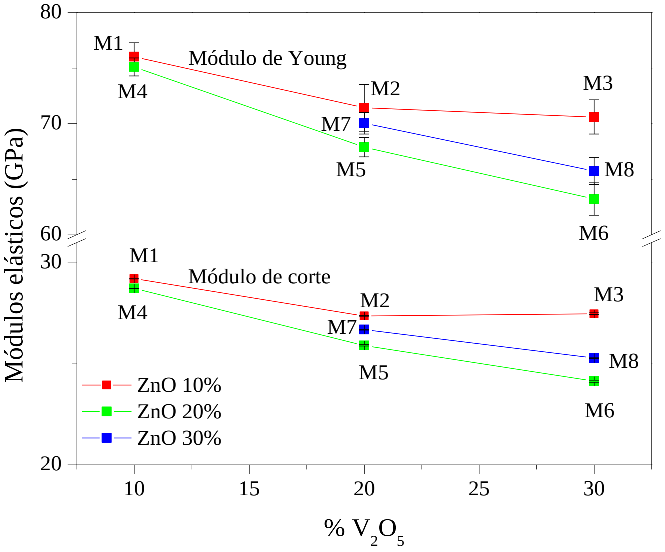

Figura 7. Módulos elásticos para las muestras dopadas con Er.

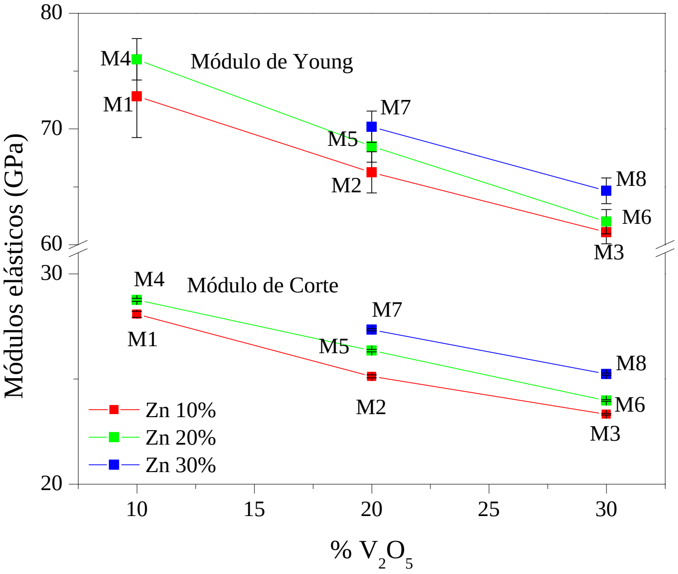

Figura 8. Módulos elásticos para las muestras dopadas con Nd.

Agradecimientos: Al proyecto CONACYT CB-2008/104151 por su financiamiento. Al Ing. Jorge Avila Diaz por el apoyo en la realización de las mediciones.

Bibliografía

1. **Kannappan AN., Thirumaran S., Palani R.** 2009, ARPN Journal of Engineering and Applied Sciences, Vol. 4, págs. 27-31.
2. **Oral I., Guzel H. y Ahmetl G.** 2011, Polym. Bull., Vol. 67, págs. 1893-1906.
3. **Schmid W., Lazos-Martinez R.** *Guía para la estimación de incertidumbre.* s.l. : Centro Nacional de Metrología, 2000.
4. **T., Kundu.** *Ultrasonic Nondestructive Evaluation.* s.l. : CRC Press, 2004. ISBN 0-8493-1462-3.
5. **Hua, Wang Wei.** 2012, Progress in Materials Science, Vol. 57, págs. 487–656.

Effective elastic constants for three-dimensional elastic metamaterials

E. Gutiérrez-Reyes* [1], J. Flores-Méndez [2], A. L. González [1], F. Perez-Rodríguez[1]

1. Instituto de Física, Benemérita Universidad Autónoma de Puebla, Apdo. Post. J-48, Puebla, Pue. 72570, México

2. Facultad de Ciencias de la Electrónica, Benemérita Universidad Autónoma de Puebla, Av. San Claudio y 18 Sur, C.U., Puebla, Pue. 72570, México

edahigr@ifuap.buap.mx

Abstract:

In this work we develop a method for finding the effective elastic constants for an elastic phononic crystal or elastic metamaterial. These effective constants are determined from the equation for the average elastic field or macroscopic field [1], which is derived by solving the system of equations that satisfy the elastic field composed of the displacement vector and the stress components $\vec{v} = (u_1, u_2, u_3, \sigma_1, \sigma_2, \sigma_3, \sigma_4, \sigma_5, \sigma_6)$. We have applied the Bloch theorem and obtained the equation that fulfills the mode $\vec{v}$ ($\vec{G}$ = 0) in the discrete Fourier expansion, which is equivalent to take a volume average over the unitary cell. From the equation for $\vec{v}$ ($\vec{G}$ = 0), it is possible to identify the effective elastic properties such as the density tensor and the stiffness matrix. We have calculated the elastic constants in the following cases: solid-solid, solid-liquid, liquid-solid, for the host and the inclusion respectively. We present numerical results for inclusions with the form of a rectangular parallelepiped in a 3D array.

1. The problem

The basic elasticity's equations that we are employing are the equation for the dynamics of the elastic displacement vector $\vec{u}(\vec{r})$ and the Hooke's law. This last gives the relation between the strain tensor and the stress tensor. They are respectively

$$-\omega^2 \rho(\vec{r}) u_i = \nabla_j \sigma_{ij}, \quad \sigma_{ij} = C_{ijkl}(\vec{r})\, \nabla_k u_l$$

Here we are supposing that the fields oscillate in time with frequency ω that is $\vec{u}(\vec{r},t) = \vec{u}\,(\vec{r}) e^{-i\omega t}$. Also, it is assumed that the density ρ($\vec{r}$) and the constants of elasticity $C_{ijkl}(\vec{r})$, taking into account the properties of the inclusion (a) and the host (b), are periodic functions of $\vec{r}$. We follow the Voigt's notation, i.e. a matrix notation to write the equations as

$$\bar{\bar{L}}(\vec{\nabla}) \cdot \vec{v} = \bar{\bar{\Omega}}\, \bar{\bar{A}} \cdot \vec{v} \quad where \ \bar{\bar{A}} = \begin{pmatrix} \rho(\vec{r}) \bar{\bar{I}}_3 & \bar{\bar{O}}_{3\times6} \\ \bar{\bar{O}}_{6\times3} & \bar{\bar{S}}(\vec{r}) \end{pmatrix},$$

$$\bar{\bar{L}}(\vec{\nabla}) = \begin{pmatrix} \bar{\bar{O}}_3 & \bar{\bar{L}}_{3\times6}(\vec{\nabla}) \\ \bar{\bar{L}}^T{}_{3\times6}(\vec{\nabla}) & \bar{\bar{O}}_6 \end{pmatrix}, \bar{\bar{L}}_{3\times6}(\vec{\nabla}) = \begin{pmatrix} \partial_x & 0 & 0 & 0 & \partial_z & \partial_y \\ 0 & \partial_y & 0 & \partial_z & 0 & \partial_x \\ 0 & 0 & \partial_z & \partial_y & \partial_x & 0 \end{pmatrix}, \ \bar{\bar{\Omega}} = \begin{pmatrix} -\omega^2 \bar{\bar{I}}_3 & \bar{\bar{O}}_{3\times6} \\ \bar{\bar{O}}_{6\times3} & \bar{\bar{I}}_6 \end{pmatrix},$$

$\vec{v} = (u_1, u_2, u_3, \sigma_1, \sigma_2, \sigma_3, \sigma_4, \sigma_5, \sigma_6)$, $\bar{\bar{O}}_3$ is a 3×3 zero matrix, $\bar{\bar{O}}_6$ is a 6×6 zero matrix, $\bar{\bar{I}}_3$ is the 3×3 identity matrix, $\bar{\bar{I}}_6$ is the 6×6 identity matrix. $\bar{\bar{S}}(\vec{r})$ Is the compliance matrix and is related with the stiffness matrix $\bar{\bar{C}}(\vec{r})$ being one the inverse of the other. As ρ($\vec{r}$) and $\bar{\bar{S}}(\vec{r})$ are periodic functions, we can write the Fourier expansion of the matrix $\bar{\bar{A}}(\vec{r})$ as

$$\bar{\bar{A}}(\vec{r}) = \sum_{\vec{G}'} \bar{\bar{A}}(\vec{G}') e^{i\vec{G}'\cdot\vec{r}} \quad , \qquad \bar{\bar{A}}(\vec{G}') = \frac{1}{V_c}\int \bar{\bar{A}}(\vec{r}) e^{-i\vec{G}'\cdot\vec{r}}\, d\vec{r},$$

where the summation ranges over the reciprocal lattice of the phononic crystal. In order to find a solution to the elasticity equations, we assume that the solution $\vec{v}$ $(\vec{r})$ satisfies the Bloch theorem $\vec{v}(\vec{r}) = e^{i\vec{k}\cdot\vec{r}} \sum_{\vec{G}} \vec{v}(\vec{G}) e^{i\vec{G}\cdot\vec{r}}$, that by substituting this Fourier expansions into the equations for the displacement we obtain the master equation for the phononic crystal written as

$$\sum_{\vec{G}'} \bar{\bar{D}}(\vec{k};\vec{G},\vec{G}')\cdot\vec{v}(\vec{G}') = 0 \quad \text{where} \quad \bar{\bar{D}}(\vec{k};\vec{G},\vec{G}') = -\left(\bar{\bar{L}}(\vec{k}+\vec{G})\delta_{\vec{G},\vec{G}'} + i\bar{\bar{\Omega}}\,\bar{\bar{A}}\,(\vec{G}-\vec{G}')\right) \qquad (1)$$

and

$$\bar{\bar{A}}\,(\vec{G}-\vec{G}') = \bar{\bar{A}}_b\delta_{\vec{G},\vec{G}'} + \Delta\bar{\bar{A}}F(\vec{G}-\vec{G}')\,, \qquad \Delta\bar{\bar{A}} = \bar{\bar{A}}_a - \bar{\bar{A}}_b, \quad F(\vec{G}) = \frac{1}{V_c}\int e^{-i\vec{G}\cdot\vec{r}}\; d\vec{r}$$

We define the average field as that given by the term $\vec{G} = 0$, $\vec{V}(\vec{r}) = \vec{v}(\vec{G} = 0)e^{i\vec{k}\cdot\vec{r}}$ where the wave vector $\vec{k}$ is restricted to the first Brillouin zone. It is possible to show that we can write $\vec{v}(\vec{G} \neq 0)$ in terms of $\vec{v}(0)$, and from the master equation, (1), with $\vec{G} = 0$ we get respectively

$$\vec{v}(\vec{G}') = -\bar{\bar{D}}^{-1}(\vec{k};\vec{G}',0)\{\bar{\bar{D}}^{-1}(\vec{k};0{,}0)\}^{-1}\cdot\vec{v}(0) \quad , \quad \bar{\bar{L}}(\vec{k})\,\vec{v}(0) + i\bar{\bar{\Omega}}\sum_{\vec{G}'}\bar{\bar{A}}\,(-\vec{G}')\cdot\vec{v}(\vec{G}') = 0 \qquad (2)$$

Identifying (2) as the equation for the average field and after some algebraic steps, we note that we can define the effective elastic properties of the phononic crystal as:

$$i\bar{\bar{\Omega}}\,\bar{\bar{A}}_{eff}(\vec{k}) = \left(\bar{\bar{L}}(\vec{k}) + \{\bar{\bar{D}}^{-1}(\vec{k};0{,}0)\}^{-1}\right)$$

We can calculate the term $\{\bar{\bar{D}}^{-1}(\vec{k};0{,}0)\}^{-1}$ by inverting, the infinite in principle, matrix $\bar{\bar{D}}(\vec{k};\vec{G},\vec{G}')$ and then taking the inverse of the 9×9 block $\bar{\bar{D}}^{-1}(\vec{k};0{,}0)$. Here we propose an alternative method to find $\{\bar{\bar{D}}^{-1}(\vec{k};0{,}0)\}^{-1}$ even though it is an approximation; the computational cost is largely reduced.

2. The finite volume approximation and the effective field approximation

In this section we show that it is possible to find an integral equation for $\bar{\bar{D}}^{-1}(\vec{k};\vec{G},0)$ in the real space. By solving this integral equation approximately, the computational cost of finding $\bar{\bar{D}}^{-1}(\vec{k};0{,}0)$ is considerably reduced. One can prove that the quantity $\bar{\bar{P}}(\vec{r}) = \sum_{\vec{G}'} e^{-i\vec{G}'\cdot\vec{r}}\bar{\bar{D}}^{-1}(\vec{k};\vec{G}',0)$ fulfills the following integral equation in the real space

$$\bar{\bar{P}}(\vec{r}) - i\bar{\bar{\Omega}}\,\Delta\bar{\bar{A}}\,\frac{1}{V_c}\int d\,\vec{r}\quad \bar{\bar{K}}(\vec{r}-\vec{r}')\bar{\bar{P}}(\vec{r}') = \bar{\bar{T}}^{-1}(0), \qquad (3)$$

$$\bar{\bar{T}}(\vec{G}) = -\bar{\bar{L}}(\vec{k}+\vec{G}) - i\bar{\bar{\Omega}}\,\bar{\bar{A}}_b \quad , \quad \bar{\bar{K}}(\vec{r}-\vec{r}') = \sum_{\vec{G}}\bar{\bar{T}}^{-1}(\vec{G})e^{i\vec{G}\cdot(\vec{r}-\vec{r}')}.$$

The integral equation (3) can be solved approximately by dividing the inclusion volume V_a in N identical cubes with centroid at $\vec{r}_j$ (the finite volume approximation), and taking a volume average at the cube i

defined as $\langle \bar{\bar{P}}_i \rangle = \frac{1}{V_{cube}} \int_{V_{cube}} d\vec{r}'' \bar{\bar{P}}(\vec{r}_j + \vec{r}'')$ $(V_{cube} \ll V_c)$. Afterwards, if we approximate $\bar{\bar{P}}(\vec{r}_j + \vec{r}''') = \langle \bar{\bar{P}}_j \rangle$ (the effective field approximation), then we get that

$$\langle \bar{\bar{P}}_i \rangle - i\bar{\bar{\Omega}}\, \Delta\bar{\bar{A}} \frac{V_c}{V_{cube}} \sum_j \sum_{\vec{G}} F_{cube}(\vec{G}) F_{cube}(-\vec{G}) \bar{\bar{K}}(\vec{G}) \langle \bar{\bar{P}}_j \rangle = \bar{\bar{T}}^{-1}(0) \quad \text{where} \quad \bar{\bar{K}}_{ij} = \bar{\bar{T}}^{-1}(\vec{G}) e^{i\vec{G}\cdot(\vec{r}-\vec{r}')},$$

and F_{cube} is the form factor of a cube with centroid at the origin and with the size of the partition. This is a linear system of equations for $\langle \bar{\bar{P}}_i \rangle$ that once solved we can calculate $\bar{\bar{D}}^{-1}(\vec{k}; 0,0)$ using the expression

$$\bar{\bar{D}}^{-1}(\vec{k}; 0,0) = \bar{\bar{T}}^{-1}(0) \left(\bar{\bar{I}} + i\bar{\bar{\Omega}}\, \Delta\bar{\bar{A}} \frac{V_{cube}}{V_c} \sum_j \langle \bar{\bar{P}}_j \rangle \right).$$

References

[1] J. Flores-Méndez and F. Pérez-Rodríguez, " Metasolid with anisotropic mass density ", EPL **103**, 54001 (2013).

Synthesis and characterization of titanium dioxide nanotubes by hydrothermal method assisted by microwave

J. A. Lima Flores, M. R. Palomino Merino, and E. Rubio Rosas

Facultad de Ciencias Físico-Matemáticas, Benemérita Universidad Autónoma de Puebla

Since 1991, in fundamental research laboratory NEC in Tsukuba Japan, Sumio Ijima discover through an electronic microscopy an strange nanometric fibers deposited on a speck of soot, those fibers were constituted with coal and have a great length and due to their shape he called it nanotubes [1]. The researches of those nanostructures prove to have interesting properties such as elasticity superlative, traction resistance and thermic stability so the interesting of their study and applications increase with the time and maintain until today. However this interest not only focus on the study of coal nanotubes but also in the possibility of synthesizes nanotubes of other compounds and with the time various researches would achieve obtain nanotubes of tungsten sulfide IV (WS2) [2], boron nitride (BN) [3], molybdenum disulfide (MoS2) [4] and niobium sulfide (NbS2) [5], each with its own properties.

Within these investigations to achieve obtain compounds with this particular morphology arise in 1996 titanium dioxide nanotubes, an event that would come into connection in the context of another intensive research had been developing for some time, that of improving a particular property having this compound, it´s photocatalytic efficiency. This property was discovered in 1967 by Akira Fujishima and would be later known as the Honda-Fujishima effect [6].

These investigations to improve photocatalytic titanium dioxide have long focused mainly on two points, integrating impurities of different ions on his structure to alter its wide band gap [7] and synthesize it with a different morphology to improve its adsorption capacity [8], therefore it was clear that a logical step was to try to synthesize with this morphological structure. Since this event titanium dioxide nanotubes have been highly studied and today it is possible to synthesize using three different techniques which include electrochemical methods [9] and hydrothermal methods [10].

This interest to improve its photocatalytic efficiency is due to the high impact would lead in the area of alternative energy because already previously been found possible to use this compound for various applications such as in the production of hydrogen for use as an alternative fuel to petroleum through the Honda-Fujishima effect [11], an effect that allows to break the water molecule via hydrolysis through a photocatalytic reaction, managing to make this process more efficient for mass production hydrogen. It is also possible to use for wastewater treatment in the decontamination technique known as heterogeneous photocatalysis and degrade complex mixtures of organic pollutants in waste water [12].

Today there are studies that confirm that the nanotube morphology improves the efficiency of photocatalytic titanium dioxide comparison of particle morphology [13], however the results have not yet managed to convince to start production at industrial level. The research focuses on improving the morphology of the nanotubes to produce structures with increasing lengths, the inclusion of other compounds to the structure of titanium dioxide such ions is also studied as did his predecessor [14] and of course in find the optimal conditions for their synthesis through three different techniques that exist to improve the times, processes and costs for obtaining it. For this purpose it became necessary to prove the synthesis of nanotubes from hydrothermal method assisted by microwave and heating equipment change based on electrical resistors, which eventually target would give satisfactory results [15]. Is now possible to find many jobs synthesis of nanotubes by microwave radiation by controlling the furnace power [16], but very few, if not null, work studying temperature ranges necessary to obtain them using this same technique.

In this work we synthesis and characterize titanium dioxide nanotubes by the hydrothermal method assisted by microwave. For this target we acquired commercial TiO2 Sigma-Aldrich Company that owns a structure with combination of anatase-rutile phase. Nanotubes of commercial TiO2 were obtained with temperatures no higher than 180 ° C and not lower than 160 ° C and were optimized using different ramps allow gradual heating and power digestion lower than 400 W. The nanotubes were observed by microscopy techniques SEM, TEM and AFM and its structure and composition was studied using the techniques of XRD and EDS. We also analyze how is the change of the phase of the nanotubes according with the increment of the temperature.

[1] S. Iijima, Nature -London 354, 56 ~1991.
[2] R. Tenne, L. Margulis, M. Genut, and G. Hodes, Nature ~London! 360,444 ~1992.
[3] N. G. Chopra, R. J. Luyken, K. Cherrey, V. H. Crespi, M. L. Cohen, S. G. Louie, and A. Zettl, Science 269, 966 ~1995.
[4] Y. Feldman, E. Wasserman, D. J. Srolovitz, and R. Tenne, Science 267, 222 ~1995.
[5] M. Nath and C. N. R. Rao, J. Am. Chem. Soc. 123, 4841 ~2001.
[6] Fujishima, Akira; Honda, Kenichi (1972). "Electrochemical Photolysis of Water at a Semiconductor Electrode". Nature 238 (5358): 37–8.
[7] Ying Yang, Congxue Tian, Res Chem Intermed (2012) 38:693–703.
[8] T. Suprabha, Haizel G. Roy, Jesty Thomas, K. Praveen Kumar, Suresh Mathew, Nanoscale Res Lett (2009) 4:144–152
[9] Xiu-Feng Xiao, Rong-Fang Liu, Tian Tian, Journal of Alloys and Compounds 466 (2008) 356–362.
[10] T. Kasuga, M. Hiramatsu, A. Hoson, T. Sekino, and K. Niihara, Langmuir 14, 3160 - 1998; Adv. Mater. 11, 1307 ~1999.
[11] Shahed U. M. Khan*, Mofareh Al-Shahry, William B. Ingler Jr., Science 27 September 2002: Vol. 297 no. 5590 pp. 2243-2245
[12] Soo-Ah Lee, Kwang-Ho Choo, Chung-Hak Lee, Ho-In Lee, Taegwhan Hyeon, Wonyong Choi, and Heock-Hoi Kwon, Ind. Eng. Chem. Res. 2001, 40, 1712-1719
[13] GH. Rajabzadeha, A. Firuzian, P. Hamzelahzadeh, Proceedings of the 4thInternational Conference on Nanostructures (ICNS4) 12-14 March, 2012, Kish Island, I.R. Iran
[14] G.K. Prasada, Beer Singha, K. Ganesana, Anirudh Batrab, Tushar Kumeriab, P.K. Gutcha, R. Vijayaraghavana, Journal of Hazardous Materials 167 (2009) 1192–1197.
[15] L. Cuia, K.N. Huib, K.S. Huia, S.K. Leec, W. Zhoud, Z.P. Wane, Chi-Nhan Ha Thucf, Materials Letters, Volume 75, 15 May 2012, Pages 175–178
[16] Xing Wu, Qi-Zhong Jiang, Zi-Feng Ma, Min Fu, Wen-Feng Shangguan, Solid State Communications 136 (2005) 513-517.

TiAlN thin films deposited by laser ablation

J. G. Quiñones-Galván[1], Enrique Campos[2], Stephen Muhl[3], Martín Flores[4]

[1] *Facultad de Ciencias Físico-Matemáticas, Benemérita Universidad Autónoma de Puebla, Puebla, México*
[2] *Instituto Nacional de Investigaciones Nucleares. Carretera México-Toluca s/n, La Marquesa, Ocoyoacac, Edo. de México, C. P. 52750, México.*
[3] *Instituto de Investigaciones en Materiales, UNAM, México, D.F. C.P. 04510*
[4] *Departamento de Ingeniería de Proyectos, CUCEI, Universidad de Guadalajara, Apdo. Postal 307, CP 45101, Zapopan Jalisco, Mexico*
erk_183@hotmail.com

The physical properties of titanium nitride (TiN) can be improved when aluminum is incorporated into the lattice to form the ternary compound TiAlN. In the present work thin films of TiAlN have been obtained by means of the simultaneous ablation of Ti and Al targets in a nitrogen containing atmosphere; the thin films were grown on silicon substrates at a deposition temperature of 200ºC. The dependence of the Al content on the laser produced plasma parameters was studied. The plasma parameters were measured using a Langmuir probe and optical emission spectroscopy. Results show a strong dependence of the quantity of incorporated Al on the plasma density. The mechanical and tribological properties depend on the Al incorporated into the TiN lattice.

TiN thin films exhibit very interesting physical and chemical properties such as: high hardness, good wear and corrosion resistance, low friction coefficient and high chemical inertness [1]. These properties make TiN thin films interesting for applications such as industrial tools due to their lifetime can be extended.

Besides the thermal stability, electrical conductivity and its characteristics as good diffusion barrier make TiN an interesting material for microelectronics applications [2].

TiN has the disadvantage that at temperatures above 550ºC it oxidizes forming a rutile TiO_2 phase component that induces a degradation of the mechanical and tribological properties of the thin films [1].

The incorporation of Al or Si substituting Ti into the TiN system forming the ternary compounds TiSiN or TiAlN have produced good results with respect to the oxidation and wear resistance. Atoms of Si or Al can substitute the atoms of Ti in the TiN lattice in several proportions forming different composition alloys. TiAlN coatings form a highly adherent aluminum oxide layer at the surface when it is heated preventing the oxygen diffusion trough the coated material. Additionally, the thermal conductivity is reduced, making the TiAlN system interesting for applications in protective coating of high speed cutting tools. The TiAlN compound enhances significantly the thermal, mechanical and wear resistance of TiN.

Thin films of titanium nitride have been grown using techniques such as laser ablation [1], sputtering [2] and arc evaporation [3]. When the laser ablation technique is used, thin films of high quality can be obtained at low temperatures due the high energetic species contained in the plasma.

The TiAlN thin films analyzed in the present work were grown by the laser ablation technique; a base pressure of $2x10^{-6}$ Torr was used. The films were deposited using a reactive atmosphere containing a mixture of 60/40 Ar/N_2 gases at a working pressure of $8x10^{-3}$ Torr. For the ablation process a Nd:YAG laser in the wavelength of 1064 nm was used, with pulse width of 5ns and 10 Hz frequency.

The TiAlN thin films were deposited with the simultaneous ablation of a Ti and an Al target. Fig. 1 shows a schematic diagram of the laser ablation deposition system used in the experiments. The distance between the Ti target and the substrate was 6 cm.

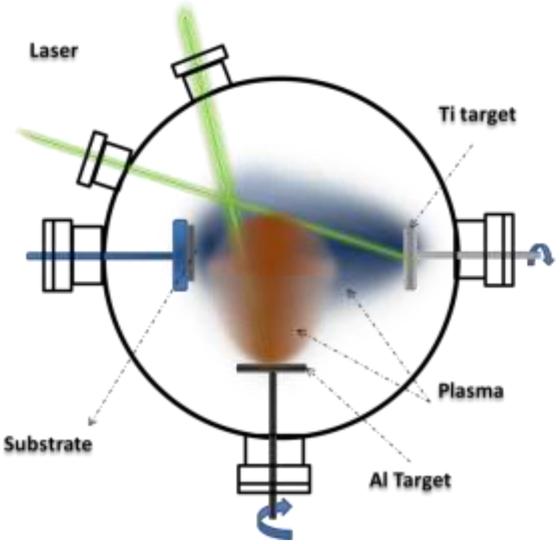

Fig. 1. Schematic diagram of the laser ablation deposition system

The thin films were grown at 200 ºC. The energy density incident in the Ti target was kept constant at 7 J/cm^2 in order to have the same kinetic energy and density of the Ti ions.

By means of optical emission spectroscopy measurements, the excited species generated during the ablation of the targets were analyzed

The mean kinetic energy and ion density of the plasma were measured using the time of flight technique obtained from a Langmuir probe of 6 mm of diameter. The chemical composition of the films was obtained by energy dispersive spectroscopy, the crystalline structure of the samples was analyzed by X-ray diffraction and Raman spectroscopy, the mechanical properties were determined by the nanoindentation technique.

References

1.- S. Acquaviva, E. D'Anna, L. Elia, M. Fernández, G. Leggieri, A. Luches, M. Martino, P. Mengucci, A. Zocco, Thin Solid Films 379, 45-49 (2000).
2.- L. García-González, M. G. Garnica-Romo, J. Hernández-Torres, F. J. Espinoza-Beltrán, Braz. J. Chem. Eng. 24(02), 249-257 (2007).
3.- S. Y. Chun, C. H. Lee, S. J. Lee, Properties of TiAl and TiAlN thin films by pulsed cathodic arc, Mater. Sci. Forum 534-536, 1413-1416 (2007).

Synthesis and modeling of SiO_2 opals with Fe inclusions

C.E. Ávila-Crisóstomo, E. Sánchez-Mora, F. Pérez-Rodríguez

Instituto de Física, Benemérita Universidad Autónoma de Puebla,
Apartado Postal J-48, Puebla, Pue., 72570, México
E-mail: cavila@ifuap.buap.mx

Introduction

Using the Stöber method, silica spheres were obtained and arranged in a fcc lattice. Fe is intended to be introduced into void spaces of the artificial opals by means of the reduction of $FeSO_4$ with $NaBH_4$. Fe changes the dielectric contrast between the SiO_2 spheres and the medium where they are embedded. Consequently, the position of the photonic band gap for waves propagating along the growth direction, namely the [111] direction, is altered. By applying a theoretical model for the artificial opals with metallic inclusions, optical spectra (reflectance, transmittance, and absorption), as well as magnetic properties (effective permeability) are meant to be calculated and compared with experimental data (SEM images, spectra of absorption, specular and diffuse reflection, magnetization curves). The comparison allows for the determination of the geometrical characteristics of the artificial opals as well as the observation of the effect of iron on optical spectra: a shift of the photonic band gap for modes propagating along the [111] direction.

Fabrication of tridimensional photonic crystals, with interesting optical properties in the visible or infrared spectrum is not an easy task. The most used techniques are lithography, holographic lithography or the preparation of artificial opals. The use of colloidal crystals is probably the cheapest and versatile alternative between all of the existent until now. Photonic crystals can be made out of different types of colloidal systems, taking advantage from the tendency of spherical particles, on the micron range, to order themselves in a compact fcc lattice. Tunning in photonic properties in a wide range of frequencies is possible by changing the size of the constituting spheres or by infiltration of another species.

Experimental Details

SiO_2 artificial opals were obtained by means of the hydrolysis of a silicon alkyl-alkoxide ($Si(OC_nH_{2n+1})_4$), tetraethyl orthosilicate (TEOS, $Si(C_2H_5O)_4$), in an alcoholic ammonia medium for the posterior condensation of the hydrolyzed species forming siloxane groups, also known as the Stöber method [1]. Two methods of sedimentation were performed in order to obtain the self-assembled fcc array of silica spheres. One of them consisted in the centrifugation of the colloidal solution at 3400 rpm for 15 minutes. However, this method was not suitable because of the low order of the array of the artificial opals, leading to an imprecise theoretical description of the optical behavior of our samples, due to its strong dependence on the periodicity. Specifically, the predicted photonic band gap for modes propagating along the [111] direction was not observed by reflectance measurements. The second method is based on gravitational sedimentation, which prevents some of the problems that generate disorder in the samples [2].

Zero-valent iron nanoparticles (ZVI) were synthesized by different methods, on the pursuit of achieving stability against oxidation and agglomeration. In the first attempts, sedimentation occurred almost after reaction was complete and oxidation few hours later. This led us to the search of alternative procedures to synthesize ZVI. In this work is described the one who gave better results. The process consists in the reduction of iron salt in aqueous solution.

Precursor of iron was $Fe(NH_4)_2(SO_4)_2{*}6H_2O$ and $NaBH_4$ served as a reductor. Carboxymethyl cellulose (CMC) played a crucial role in the stabilization of ZVI, acting as a surfactant to prevent agglomeration [3]. The general formula of iron 2+ salts reduction is as follows:

$$Fe(H_2O)_6^{2+} + 2BH_4^- \rightarrow Fe^0 \downarrow + 2B(OH)_3 + 7H_2$$

The ratio of CMC to Fe employed (w/w) was 5:1 and was added to the solution containing the iron salt. Stoichiometric amounts of NaBH4 were added dropwise to complete the reaction. Solutions consisted of deionized water previously degasified with a nitrogen flux during 40 minutes approximately. Also the entire process was carried out with a nitrogen flux to prevent oxidation.

Theoretical Description

The magnetic properties of the fabricated opals can be described within the framework of the homogenization theory developed in the work [4]. Such a theory provides explicit formulas for all the components of the permittivity and permeability tensors for a magnetodielectric photonic crystal in terms of the parameters of the inclusions and the host material. On the basis of this homogenization theory, we have elaborated a computing program to calculate the effective permittivity and permeability of the SiO_2 opals with Fe inclusions. The calculated effective parameters are useful for studying magnetic hysteresis loops of the fabricated opals.

References

[1] W. Stöber, F. Bohn, *J. Colloid Interface Sci.*, **26**, 62-69 (1968)

[2] P. Ni et al., *Adv. Mater.*, **13**, 437-441 (2001)

[3] Q. Wang et al., *J. Contam. Hydrol.*, **114**, 35-42 (2010)

[4] V. Cerdán-Ramírez et al., *J. Appl. Phys.* **106**, 103520 (2009)

MAGNETIC PROPERTIES OF NANOSTRUCTURED C-Co and C–Ni COMPLEXES

[1]V. Chabanenko, [1]E. Zubov, [2]R. Cortés-Maldonado, [2]F. Pérez-Rodríguez, [3]R. Escudero, [3]F. Morales, [4]R. Kochkanjan, [4]A. Zaritovskii, [1]O. Kuchuk, [1]S. Zolotar, [5]A. Nabiałek [1]O. Galkin Donetsk Institute for Physics and Engineering, NAS, Donetsk, 83114, Ukraine; [2]Instituto de Física, Benemérita Universidad Autónoma de Puebla, Apdo. Post. J-48, Puebla, Pue. 72570, México [3]Instituto de Investigaciones en Materiales, Universidad Nacional Autónoma de México, DF, México [4]Institute of Physico-Organic and Coal Chemistry NAS, 83114 Donetsk, Ukraine [5]Institute of Physics, PAS, al. Lotników 32/46, 02-668 Warsaw, Poland

Email: vikchabanenko@gmail.com

The novel chemical metallization method of graphite was used to obtain a nanostructured complex. For the synthesis of metal-carbon clusters, we used previously purified graphite and clusters of metals. Clusters were prepared by reducing the corresponding metal salts in the aqueous solutions of various reducing agents. The synthesis temperature was in the range 20-90º C. Powder of C-Co/Ni complexes was pressed into a plate with sizes 10x4x0.7 mm^3. Magnetic field was oriented along the longest edge of the plate. Zero fields cooled (ZFC) and field cooled (FC) magnetization vs temperature measurements in different fixed magnetic fields up to 2 T were performed with a SQUID magnetometer (Fig.1). Such behavior of magnetic characteristic of our C-Co complex is similar to those features that have been observed in Co nanoparticle systems prepared by co-sputtering or co-evaporation of Co with non-magnetic materials [1]. Temperature dependences of the magnetization M(T) reveal the effects of irreversibility. In particular, the blocking temperature T_B~300K. Using the characteristic measurement time τ_m~20 s and microscopic fluctuation time τ_0~10^{-10} s with anisotropy constant K_A=4.12*10^5 Jm^{-3} [2] for Co from relation $\tau_m = \tau_0 \exp(\frac{K_A V}{k_B T_B})$, we obtain the mean diameter d~8nm of the spherical nanoparticles. The low temperature anomaly in Fig.1 is assumed to be a manifestation of additional ordering on the surface of the magnetic nanoparticle.

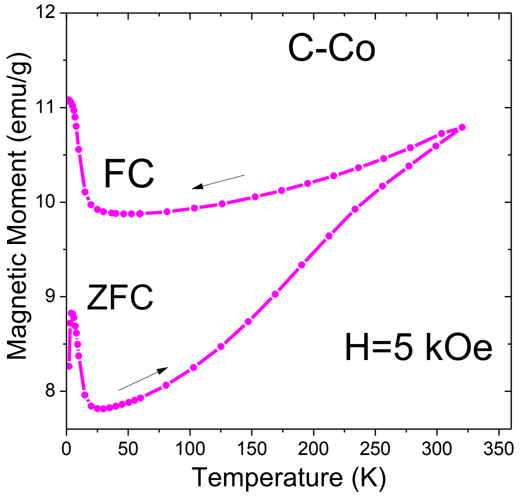

Fig.1

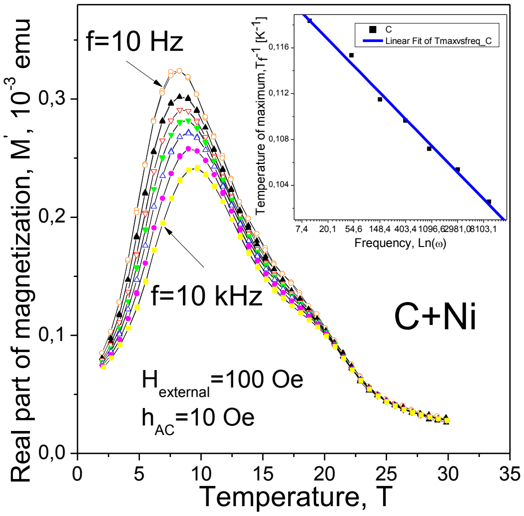

Fig.2

As for C-Ni Investigation of ZFC and FC magnetization has shown that pressed compound is a very weak paramagnetic. At lowering temperature, the material undergoes ordering and goes into a spin-glass state below T = 35 K. This is evidenced by a study of AC susceptibility (Fig.2). One can estimate the values of potential barrier, F_B, and relaxation time, τ_0, for a given spin-glass system. Indeed, the observation time $\tau=1/\omega$, where ω is the frequency of the AC magnetic field, is expressed as $\tau = \tau_0 \exp(\frac{F_B}{T})$ [3].

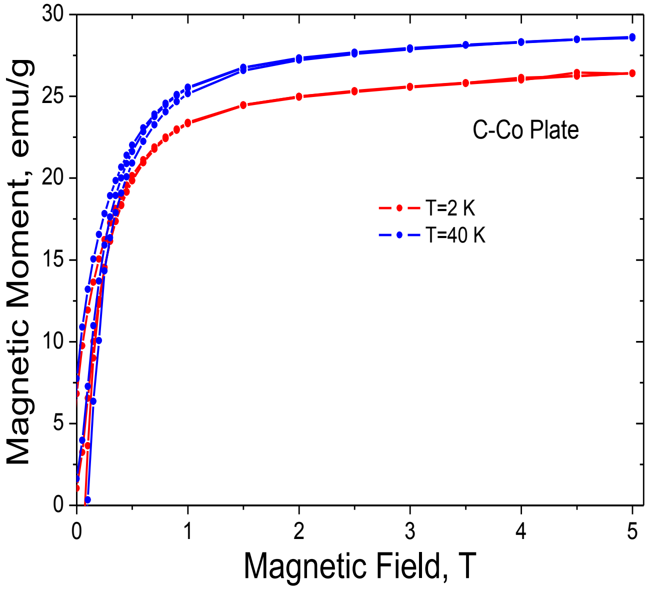

Fig.3

For the temperature of maximum of $M'(T)$, $T=T_f$, we have $1/T_f=-(\ln\omega+\ln\tau_0)/F_B$. From linear dependence of $1/T_f$ as a function of ω (see inset to Figure), we have found F_B=430.7 K and $\tau_0=7.3*10^{-24}$ s. Hysteresis phenomena between +/-2 T at various temperatures were investigated too. Irreversible effects in magnetic properties were observed in magnetic fields up to 5 kOe. Stronger fields lead to saturation of the magnetic characteristics (Fig.3).

References:

[1] M. Beerman, A. Pakhomov, Y. Bao, K. Krishnan. Univ.of Washington, Seattle, WA 98195, USA.
[2] A.P. Guimarães. Principles of Nanomagnetism/ Springer: Heidelberg. (2009) P.38.
[3]. I. Morgenstern. Long-time behavior of spin-glasses at low temperatures/ Phys.Rev.B.-V.27, N7.-P.4522-4525 (1983).

Holes drilling in gold and silver decahedral nanoparticles by the convergent beam electron diffraction electron beam.

Samuel Tehuacanero-Cuapa[1-2], José Reyes-Gasga[1],
Rodolfo Palomino-Merino[2] and Ramiro García-García[1].

[1]Instituto de Física, UNAM, Circuito de la investigación s/n, Cd. Universitaria, Coyoacán 04510, Mexico; [2]Facultad de Ciencias Físico-Matemáticas BUAP, Avenida San Claudio y 18 Sur, Colonia San Manuel, Puebla C.P. 72570, Mexico;

In this work, we comment on the drilling of holes observed in both the silver and gold decahedral particles of approximately 40 and 30 nm in diameter, respectively, when they are irradiated by the 200 kV electron beam in the CBED condition. However, although they are done under the same circumstances, the holes are shapeless in the silver and faceted in gold nanoparticles. The holes are closed during their high-resolution TEM observation in both materials. To comment their differences, displacement energy considerations are taken into account as function of the sputtering energy in order to modify the displacement cross-section of the processes(1). Drilling and closing of nano-holes assisted by electron beam is not exclusive of decahedrales nanoparticles. The same phenomenon was reported in foil samples of magnesium (2) and magnesium alloys (3).

Experimental procedure. The silver decahedral nanoparticles were synthesized by a silvercolloidal solution obtained in a reflux system using methoxy-ethanol (4). The gold decahedral nanoparticles were synthesized by the Brust method (5). The particles were deposited onto a 200-mesh copper grid previously covered by plastic collodion and carbon films for the transmission electron microscope (TEM) observation. A JEOL-2010F FASTEM electron microscope (Jeol, Japan) was used. TEM observations were performed in two stages. First, the particle was irradiated with the convergent electron beam in CBED conditions. This is the moment where the hole is done. Second, the particle is observed in HRTEM conditions. This is the moment where the hole is closed.

Results. After 3 min under the CBED electron beam, a hole of 8 nm in diameter approximately is observed in the silver decahedral particles at the incidence site. Around the hole, dark spots are observed. The fast Fourier transforms of the dark spots indicate that they correspond to the silver face centered cubic (FCC) structure(6). The same result was obtained in the gold decahedral nanoparticles, but with some differences. After 5 min of CBED irradiation time, a hole is also produced. However, these holes present any dark clusters around them, and they are of 3 nm in diameter approximately. Another difference is that the hole is highly faceted. The holes in silver and gold decahedral nanoparticles are closed during the HRTEM observation.

Conclusions. The 200 kV-FEG electron beam intensity focused in the CBED mode is able to drill holes in silver and gold decahedral nanoparticles. The shape and size differences of the produced holes, and the subsequent closing of the holes during the HRTEM observation, are subjects that require of further explanation. The closing of holes could be explained as function of the dynamic of surface diffusion of atoms which optimizes the geometry of the damage process.

Acknowledgements

We thank to Dr G. Mondragon-Galicia, Dr Velumani Subramaniam, and Ing. S. Tehuacanero Nuñez for experimental support. We also thank M. Monrroy, R. Hernandez, P. Mexia, A. Angeles and D. Quiterio for technical support. We thank to C. Guarneros Aguilar and J. C. Flores Garcia for the synthesis of silver samples.

References

(1) Samuel Tehuacanero-Cuapa, José Reyes-Gasga, Etienne F. Brès, Rodolfo Palomino-Merino, Ramiro García-García. Radiation Effects and Defects in Solids Vol. 169, Iss. 10, 2014.
(2) Xu,W.; Zhang, Y.; Cheng, G.; Jian,W.; Millett, P.C.; Koch, C.C.; Mathaudhu, S.N.; Zhu, Y. *Nat. Commun.* [Online] **2013**. www.nature.com/naturecom munications. DOI:10.1038/ncomms3288 (accessed April 1, 2014).
(3) Zheng, H.; Liu, Y.; Cao, F.; Wu, S.; Jia, S.; Cao, A.; Zhao, D.; Wang, J. *Sci. Rep.* [Online] **2013**.www.nature.com/scientificreports. DOI:10.1038/ srep01920 (accessed April 1, 2014).
(4) Flores, J.C.; Torres, V.; Popa, M.; Crespo, D.; Calderón-Moreno, J.M. *Colloids Surf. A* **2008,** *330,* 86–90.
(5) Brust, M.; Fink, J.; Bethell, D.; Schiffring, D.J.; Kiely, C. *J. Chem. Soc. Chem. Comm*. **1995,** *16,* 1655–1656.
(6) Tehuacanero-Cuapa, S.; Palomino-Merino, R.; Reyes-Gasga, J. *Radiat. Phys. Chem.* **2013,** *87,* 59–63.

Sesión 3

Absorption enhancement by lattice of perforated shells

Victor M. García-Chocano and **José Sánchez-Dehesa**
Grupo de Fenómenos Ondulatorios, Dpto. Ingeniería Electrónica,
Universitat Politècnica de Valencia,
Camino de Vera s.n. (Edificio 7F), 46022 Valencia, Spain.

Sonic crystals (SC) consist of periodic arrangements of scatterers embedded in a fluid or a gas. Due to their periodicity, SCs forbid the propagation of sound waves at specific ranges of frequencies called bandgaps. This feature leaded to its proposal as noise barriers [1]. Since then, several works have dealt with the improvement of the absorption by adding fibrous and porous materials to the scatterers [2,3]. The use of microperforated plates in the building units was also considered [4]. However no attention was paid for the case of large perforations where losses are expected to be low.

In this work we deal with square lattices of shells made from perforated plates (see Fig. 1a). Due to the perforation ratio and the size of the holes, the plates are almost acoustically transparent although they still present some absorption. Numerical calculations have been performed through the multiple scattering theory. Reflectance, transmittance and absorption spectra of slabs having 1 to 5 rows of shells are shown in Fig. 1b. The radius of the cylinders is $R=4cm$ and the lattice parameter is $a=11cm$. It is found an unusual enhancement of the absorption and reflectance around the diffraction limit of the lattice ($\lambda=a$). This result agrees with the experimental data reported in Reference [3].

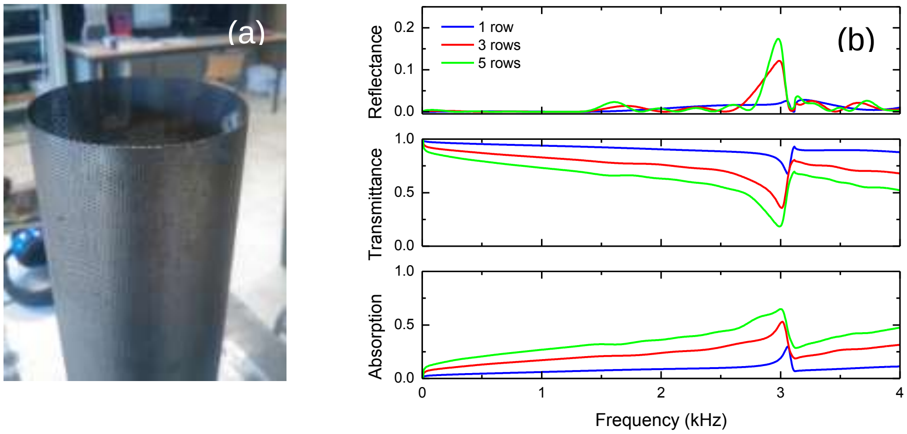

Figure 1: Photograph of a perforated shell (a). Reflectance, transmittance and absorption spectra of slabs with perforated shells having different number of rows (b).

When examining the pressure field inside the crystal, it is noticed that modes with components perpendicular to the impinging wave appear at the frequencies where absorption enhancement occurs. These modes deviates the energy through the axis of the slab, in such a manner that redirected waves travel through a lossy path and therefore absorption is enhanced. The redirection effect can be observed in Fig. 2a, where a Gaussian beam impinges on a finite slab of perforated shells. Apart from the transmitted beam, two additional beams leave the slab along the y-axis. The far field pressure of this simulation is illustrated in Fig. 2b as a function of the frequency. It is found that the forward scattering (θ=0º) presents a minimum at 3052Hz, whereas redirected waves at ±90º reach a maximum at this frequency.

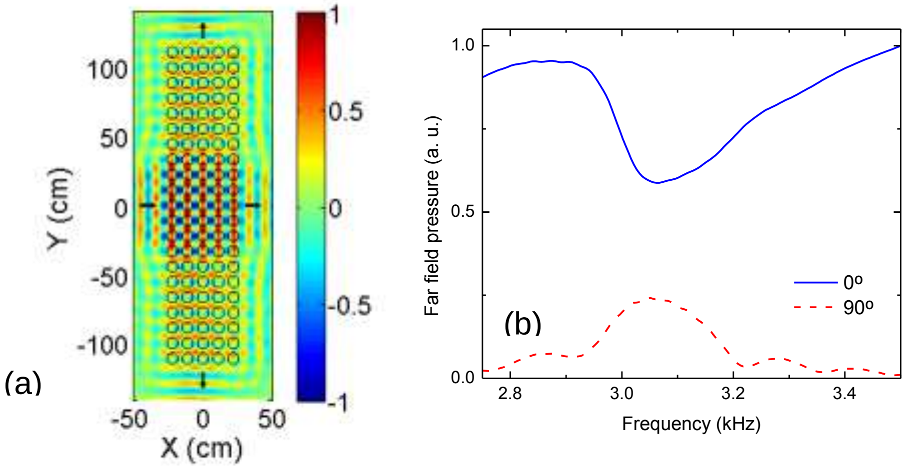

Figure 2: Gaussian beam impinging on a slab of perforated shells (a) and far field pressure for the transmitted (0º) and redirected (90º) waves (b).

The dispersion relation of the structure has been calculated through multiple scattering and 3D finite element simulations, obtaining a good agreement between both methods. Fig. 3a shows the band diagram compared to that of the free space. It is found that bands are similar in both cases, although a pseudogap is found in the region of interest. This phenomenon can be observed in Fig. 3b. The Bloch modes are included for the wavevector specified with a dashed line. It is found that modes from Bands 2 and 5 are similar to free space propagation while Bands 3 and 4 are hardly excited due to their symmetry.

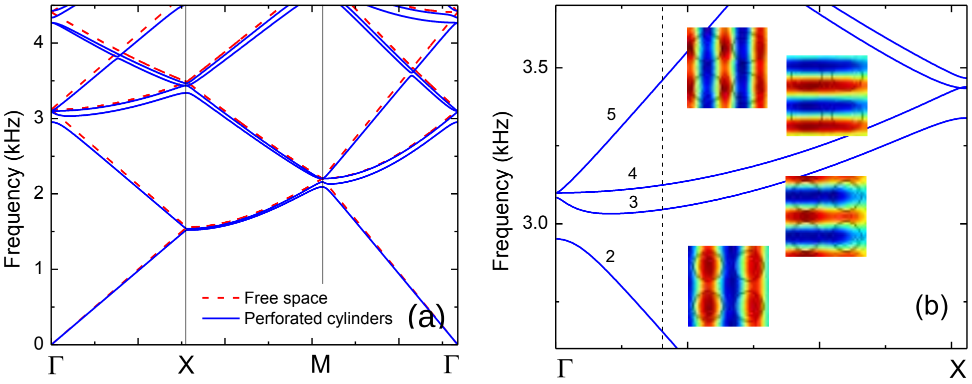

Figure 3: Dispersion relation of a lattice of perforated shells compared with free space (a) and zoom of frequency at the Γ-X direction (b). Bloch modes of the bands at the wavevector indicated with a dashed line are included.

References:

[1] J. V. Sánchez-Perez, D. Caballero, R. Martínez-Sala, C. Rubio, J. Sánchez-Dehesa, F. Meseguer, J. Llinares, and F. Gálvez, Phys. Rev. Lett. **80**, 5325 (1998).
[2] O. Umnova, K. Attenborough, and C. M. Linton, J. Acoust. Soc. Am. **119**, 278 (2005).
[3] J. Sánchez-Dehesa, V. M. García-Chocano, D. Torrent, F. Cervera, S. Cabrera, and F. Simón, J. Acoust. Soc. Am. **129**, 1173 (2011).
[4] V. M. García-Chocano and J. Sánchez-Dehesa, Appl. Phys. Lett. **101**, 1

Nystrom integral equation method for the propagation of 3D acoustic waves

F. Villa-Villa,[1] A. Mendoza-Suárez[2], H. Pérez-Aguilar[2] and F. Ramos-Mendieta[3]

[1]*Centro de Investigaciones en Optica, Loma del Bosque 115, Lomas del Campestre, León Gto. 37150 MEXICO.*
[2]*Facultad de Ciencias Físico-Matemáticas, Universidad Michoacana de San Nicolás de Hidalgo, Edificio "B", Ciudad Universitaria 58060, Morelia, Michoacán, México.*
[3]*Departamento de Investigación en Física de la Universidad de Sonora. Apdo. Post. 5-088, Hermosillo Sonora 83190, MEXICO.*

In present work we propose a numerical integral method based on the Green's function to solve the Helmholtz equation for acoustic waves to determine the scattered field by complex 3D objects when an incident wave interacts with a heterogeneous system composed of multiple objects.

Introduction. It is well known in the study of acoustic waves that there are many ways to formulate a wave equation in the stationary sate by assuming harmonic time variation on wave functions, that imply the scalar Helmholtz equation. We chose the formulation based on the divergence of the displacement function

$$\nabla^2\psi + k^2\psi = 0, \tag{1}$$

Where $\psi = \nabla \cdot \vec{u}$, being $\vec{u}$ the displacement of a point within the material as the wave perturbs the continuous medium while traveling in it, and *k* the magnitude of the propagation wave vector.

This equation has been solved in the past by different authors[1-2], by applying the integral method based on using the second Green's identity and the Green's function for two-dimensional problems, and only some few have formulated the solution for 3D systems by using different approaches for some specific cases.

$$\oint_S \left[G(\vec{r},\vec{r}\,')\frac{\partial\psi(\vec{r}\,')}{\partial n'} - \psi(\vec{r}\,')\frac{\partial G(\vec{r},\vec{r}\,')}{\partial n'} \right] dS' = \psi(\vec{r})\theta(\vec{r}) + \psi^{inc}(\vec{r}). \tag{2}$$

The Green's function in this case will be

$$G(\vec{r},\vec{r}\,') = aR^{-1}e^{qR}, \tag{3}$$

where $a = 1/4\pi$, $q = ik$, $\vec{R} = \vec{r} - \vec{r}\,'$ being $\vec{r}$ the point where the field is measured and $\vec{r}\,'$ the vector that spans the surface *S*.

$$\theta(\vec{r},\vec{r}\,')=\begin{cases}1 & if \quad \vec{r}\in S\\ 0 & if \quad \vec{r}\notin S\end{cases}. \tag{4}$$

In this work, we propose a new approach based on using the method of Nystrom, which was originally proposed to solve integral equations whose integrand is not singular. As the Green's function and its normal derivative are inherently singular in our case, a regularization scheme is proposed in order to solve the problem numerically.

The Nystrom method for integral equations. Let us assume that we have a single object limited by the surface *S* with an outward normal, and we want to determine the scattered field outside *S*. By dividing the surface in *N* patches

$$\sum_{i=1}^{N}\oint_{S_i}\left[G(\vec{r},\vec{r}\,')\frac{\partial\psi(\vec{r}\,')}{\partial n'}-\psi(\vec{r}\,')\frac{\partial G(\vec{r},\vec{r}\,')}{\partial n'}\right]dS'=\psi^{inc}(\vec{r}). \tag{5}$$

Then, the idea behind the Nystrom's method consists on evaluating the integrals on the *i*-th patch at P_i points

$$\sum_{i=1}^{N}\sum_{j=1}^{P_i}w_j\oint_{S_i}\left[G(\vec{r},\vec{r}_j\,')\frac{\partial\psi(\vec{r}_j\,')}{\partial n'}-\psi(\vec{r}_j\,')\frac{\partial G(\vec{r},\vec{r}_j\,')}{\partial n'}\right]dS'=\psi^{inc}(\vec{r}) \tag{6}$$

determined by the Gauss quadrature rule of a given order with the weight factors w_j.

As it is well known, the Gauss quadrature method works properly when the integrands are not singular. So, Ec. (6) will give good results always that $\vec{r}\neq\vec{r}\,'$. The method to manage the singular case presents some challenges that will be presented in the conference.

References

1.- S. Zhi-Jie, W. Yue-Sheng, and Z. Chuan-Zeng, Appl. Math. Engl. **34** 1123-1144 (2013).
2.- P. O. Hsie, W. Tsung-Tsong, and Jia-Hong, IEEE Trans. On Ultrasonics and Freq. Control **53** 148-158 (2006).

Bloch oscillations in elastic systems

Rafael A. Méndez-Sánchez[a], G. Báez[b], M. Cobián, A. Arreola, J. Sánchez-Dehesa, and F. Cervera

[a]Instituto de Ciencias Físicas, Universidad Nacional Autónoma de México, A.P. 48-3, 62251 Cuernavaca, Morelos, México.

[b]Departamento de Ciencias Básicas, Universidad Autónoma Metropolitana-Azcapotzalco, Av San Pablo 180, Col. Reynosa Tamaulipas, 02200 México DF, México.

Bloch oscillations are ubiquitous in nature. They were predicted several years ago in a periodic potential subject to a static electric field. Nowadays they have been found in several wave systems [1-7]. In this work we present numerical evidence of Bloch oscillations of torsional waves in a beam with notches. In the model used the lengths between notches vary according to a simple rule with decreasing lenghts that depend on a parameter "γ" [8,9]. The simulations were done with the transfer matrix method applied to a finite rod [10]. Several normal modes of the beam were calculated. When γ vanishes, the periodic system is obtained and bands and gaps appear. When the γ is small, but different from zero, the Wannier-Stark ladders appear showing a equidistant spectrum. The dynamics of a wave-packet was also studied in a scattering simulation. To do this the wave-packet was expanded in the normal modes of the beam calculated numerically. When γ=0, the wave-packet shows the well-known dynamics of a periodic system: It crosses the structure when the central frequency of the wave-packet lies inside the band but it is completely reflected by the structure when its central frequency is inside the gap (See Fig. 1). When $\gamma \neq 0$, the Bloch oscillations appear. An experimental verification of this phenomenon is expected in the short term.

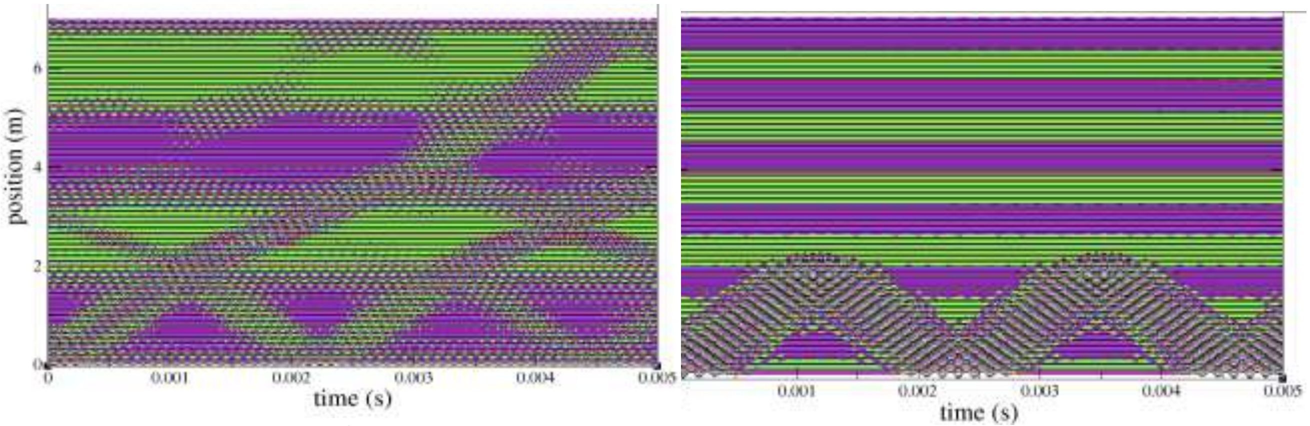

Fig. 1. Dynamics of a torsional wave-packet in an aluminum beam with a locally periodic structure with of 20 cells

each of 10 cm of length. (Left) The central frequency of the packet is inside a band and the wave-packet crosses the structure. (Right) The central frequency of the packet lies inside a gap; then the wave-packet is completely reflected by the structure.

References

[1] L. S. Kuzmin and D. B. Haviland, Observation of the Bloch oscillations in an ultrasmall Josephson junction, Phys. Rev. Lett. 67, 2890 (1991).

[2] Christian Waschke, Hartmut G. Roskos, Ralf Schwedler, Karl Leo, Heinrich Kurz, and Klaus Köhler, Coherent submillimeter-wave emission from Bloch oscillations in a semiconductor superlattice, Phys. Rev. Lett. 70, 3319 (1993).

[3] V. Agarwal, J. A. del Río, G. Malpuech, M. Zamfirescu, A. Kavokin, D. Coquillat, D. Scalbert, M. Vladimirova, and B. Gil, Photon Bloch Oscillations in Porous Silicon Optical Superlattices Phys. Rev. Lett. 92, 097401 (2004).

[4] Riccardo Sapienza, Paola Costantino, Diederik Wiersma, Mher Ghulinyan, Claudio J. Oton, and Lorenzo Pavesi, Optical Analogue of Electronic Bloch Oscillations Phys. Rev. Lett. 91, 263902 (2003).

[5] G. Ferrari, N. Poli, F. Sorrentino, and G. M. Tino, Long-Lived Bloch Oscillations with Bosonic Sr Atoms and Application to Gravity Measurement at the Micrometer Scale, Phys. Rev. Lett. 97, 060402 (2006).

[6] Henrike Trompeter, Wieslaw Krolikowski, Dragomir N. Neshev, Anton S. Desyatnikov, Andrey A. Sukhorukov, Yuri S. Kivshar, Bloch Oscillations and Zener Tunneling in Two-Dimensional Photonic Lattices, Thomas Pertsch, Ulf Peschel, and Falk Lederer Phys. Rev. Lett. 96, 053903 (2006).

[7] Helios Sanchis-Alepuz, Yuriy A. Kosevich, and José Sánchez-Dehesa, Acoustic Analogue of Electronic Bloch Oscillations and Resonant Zener Tunneling in Ultrasonic Superlattices, Phys. Rev. Lett. 98, 134301 (2007).

[8] L. Gutiérrez, A. Díaz-de-Anda, J. Flores, R. A. Méndez-Sánchez, G. Monsivais, and A. Morales, Wannier-Stark Ladders in One-Dimensional Elastic Systems, Phys. Rev. Lett. 97, 114301 (2006)

[9] G. Monsivais, R. A. Méndez-Sánchez, A. Díaz-de-Anda, J. Flores, L. Gutiérrez, and A. Morales, “Elastic Wannier-Stark Ladders in Torsional Waves”, Journal of Mechanics of Materials and Structures 2 (2007) 1629-1638.

[10] A. Morales, J. Flores, L. Gutiérrez, and R. A. Méndez-Sánchez, “Compresional and Torsional Wave Amplitudes in Rods with Periodic Structures”, Journal of the Acoustical Society of America 112, (2002) 1961-1967.

Sesión 4

Designing the plasmonic response of metallic nanoparticles

Cecilia Noguez
Instituto de Física, Universidad Nacional Autónoma de México,
Apartado Postal 20-364, México D.F., 01000 MÉXICO

Metal nanoparticles (NPs) exhibit remarkable physical and chemical properties which are morphology-dependent. Particular interest has been paid in the optical response of NPs because their surface plasmon excitations strongly couple with external light. At the nanoscale, this physical property conducts to new phenomena because these surface plasmon resonances are localized and consequently they enhance the near electromagnetic field. This latter can be control for increasing significantly the sensitivity of optical spectroscopies. In this presentation, we discuss surface plasmon in metal NPs, their localization, the electromagnetic field enhancement of such plasmons and their application in the so-called tip-enhanced Raman spectroscopy (TERS) [1].

[1] Noguez, C., Villagómez, C. J. and González, A. L. (2014), Plasmonics of multifaceted metallic nanoparticles, field enhancement, and TERS. Phys. Status Solidi B. doi: 10.1002/pssb.201350416

Diffraction of Light by Two Dimensionally Structured Metallic Surfaces

Raúl García-Llamas

Departamento de Investigación en Física, Universidad de Sonora
Apdo. Postal 5-88, Hermosillo, Sonora, México
email:ragal@cifus.uson.mx

Abstract: The problem of the diffraction of light, based on the Rayleigh criterion, by two-dimensionally structured metallic surfaces is solved. Then, the flux of surface plasmons at the surface is analyzed.

Introduction: Surface Plamons (SP) are electromagnetic modes that are localized at the interface between a metal and a dielectric medium. Its amplitude decay exponentially as function of the distance perpendicular to the surface and it exist for frequencies below the plasma frequency divided by the squared root of 2. Several approaches have been used in order to solve the problem of diffraction of light by bigratings [1-7]. On the other hand, studies about the scattering, interference and controlling of SP by surface defect and other type of structure have been published, from the experimental point of view [8-11] as well as the theoretical one[12]. This field of research is known as “plasmonics”.

In this paper, the problem of the diffraction of light by structured metallic surfaces is solved. Two types of surfaces are studied; the simple bisinusoidal surface shown in fig. 1a, and the planar and smooth surface with Gaussian shaped defects shown in fig 1b. On both cases, a matrix (integral) equation is found; it relates the scattered amplitudes to the incident one. In the first case, the surface is a 2-dimensional periodic function which is separating a metallic region of a dielectric medium. When the light impinges this surface, the specular reflection as a function of the angle of incidence and frequency shows minima produced by the coupling between photons and SP via the bigrating, and two branches of its optical relation dispersion are displayed, Fig. 2a. The near-field intensity in strong resonant condition, which corresponds to a zero of the specular reflection, has a sinusoidal shape in the direction perpendicular to the plane of incidence and its period is half of the corresponding wavelength of the SP, Fig 2b. The shape is associated to the excitation of two SPs with wave vectors almost perpendicular to the plane of incidence.

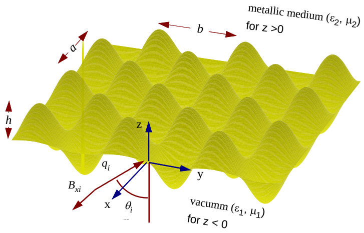

Fig. 1a. The bigrating.

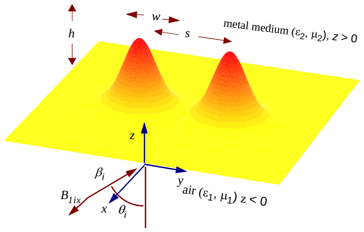

Fig. 1b. Unit cell with two Gaussian wells.

Besides, a near-field intensity enhancement is found, which depends on the coupling strength between photons and SPs. In resonant conditions, the intensity is dominated by the second order contribution to the near field intensity.

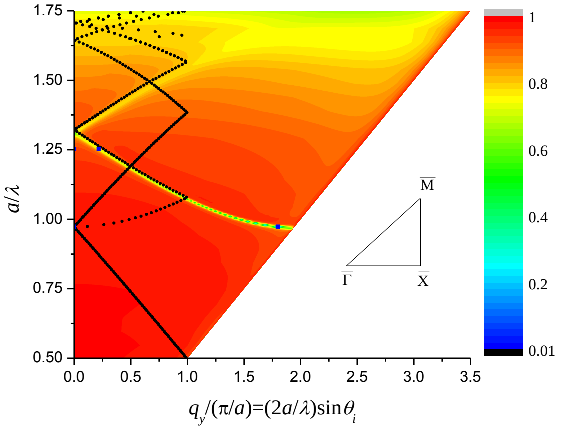

Fig. 2a. The optical relation dispersion of SP (specular reflection) as a function of angle of incidence and the wavelength.

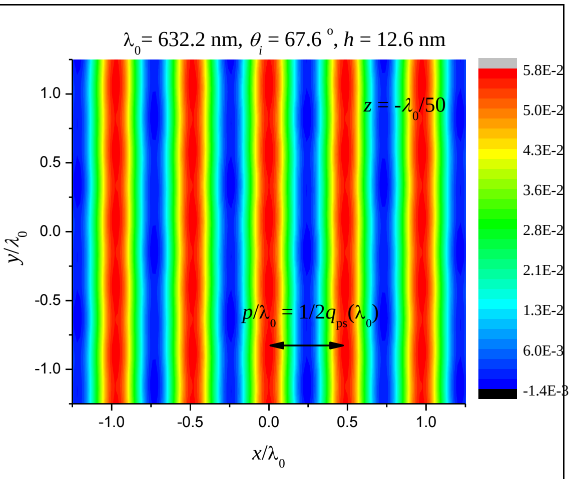

Fig. 2b. The squared root of the magnetic field projected on the plane x-y, at z=13nm, at resonant condition.

In the second case, a study of the scattering of electromagnetic waves from two-dimensional defects on planar and smooth surface separating a metallic region from vacuum is presented. Numerical results are obtained using Gaussian-shaped defects. The near-field intensity shows that the defect acts as radiating dipole surface nano-antenna if the width of the defect is less than a fourth of wavelength; a nano-sized defect. This is due to the coupling of light with surface plasmons. As the number of the defects is increased other shapes of surface radiation antenna are shown, and besides a confinement of energy between them is displayed. The numerical results of this case will be presented at the meeting.

References

R. Petit, *Ed. Electromagnetic Theory of Gratings* (Springer Verlag, New York 1980).
G. H. Derrick, R. C. McPhedran, D. Maystre, and M. Nevière, Appl. Phys. **18**, 39-52 (1979)
D. Maystre and M. Nevière, J. Opt. (Paris). **9**, 301-306 (1978)
N. E. Glass, A. A. Maradudin, and V. Celli, Phys. Rev. B **27**, 5150-5153, (1983).
J. J. Greffet, C. Baylard, and P. Versaevel, Opt. Lett. **17**, 1740-1742 (1992).
J. B. Harris, T. W. Preist, J. R. Sambles, R. N. Thorpe, and R. A. Watts J. Opt. Soc. Am. A **13**, 2041-2049 (1996).
T. Matsuda, D. Zhou, and Y. Okuno, J. Opt. Soc. Am. A **19,** 695-701 (2002).
B. Hecht, H. Bielefeldt, L. Novotny, Y. Inouye, D. W. Pohl. Phys. Rev. Lett. **77**, 1890.
Igor I. Smolyaninov, David L. Mazzoni, and Chistopher C. Davis. Phys. Rev. Lett. **77**, 3877.
Sergey I. Bolzhevolnyi and Fedor A. Pudonin. Phys. Rev. Lett. **78**, 2824-2826 (1997).
J. R. Krenn, A. Dereux, J. C. Weeber, E. Bourillot, Y. Lacroute, J. P. Goudonnet, G. Schider, W. Gotschy, A. Leitner, F. R. Aussenegg, and C. Girard. Phys. Rev. Lett. **82**, 2590-2593.
A. V. Shchegrov, I. V. Novikov, and A. A. Maradudin. Phys. R

Metal-2D Photonic Crystal Interface: Surface Modes interacting with Waveguide Modes

Jorge A. Gaspar-Armenta,[1*] F. Villa-Villa,[2]
[1]*Departamento de Investigación en Física, Universidad de Sonora, Apdo. Postal 5-88, Hermosillo, Son. 83190 México*
[2]*Centro de Investigaciones en Óptica, A. C. Loma del Bosque 115, Lomas del Campestre, León, Gto. 37150 México.*
**corresponding author: jgaspar@cifus.uson.mx*

Abstract: Dispersion relation of surface modes in a metal-two dimensional photonic crystal interface are obtained using the finite difference time domain method. We study the conditions for the interactions of the interface modes with waveguide modes inside the phtonic crystal. .

OCIS codes: (230.5298) Photonic crystals;(240.6690) Surface waves; (240.6680) Surface plasmons

1. Introduction.

Photonic crystals (PC) have been under intense research during the last twenty five years [1], owing to their potential for development of integrated circuits. As they become part of a complex circuit, their interfaces interact with other components of the system. Since the beginning of PCs, interface and defect modes have been studied [2], and they have been important as a way to concentrate energy at surfaces or to guide a signal through the PC. We have studied recently the interface waves for a metal-2DPC for transverse electric (TE) polarization [3], and discussed the possibility of using them to inject energy into a waveguide inside a 2DPC [4]. For transverse magnetic polarization, with the magnetic field pointing along the axis of the 2DPC, a more complex situation happens, since then we have the possibility of also excite surface plasmons.

In this work we study the interface modes for a metal-2DPC system in TE and TM polarization. We use the finite difference time domain method (FDTD) to compute the dispersion relation of the modes and the plane wave method for the band structure. The coupling of the interface modes with a waveguide of defects inside the 2DPC are explored as a way to inject light to the waveguide.

2. System and Methods of calculation.

The two dimensional photonic crystal considered has a square unit cell of side L. Two systems are considered, for TE polarization, the core is a square of side d, for TM polarization we use a cylindrical core of radius R such that the fraction of the circle to the square cell is given by $f = \pi R^2 / L^2$. The cells form a square array of side L. The bulk band structure of the 2DPC was computed used either a plane-wave method or FDTD. Then the projected band structure into one of the sides of the square of the first Brillouin zone was obtained. For the metal we used a Drude model dielectric constant given by

$$\varepsilon(\omega) = 1 - \frac{\omega_p^2}{\omega^2 + i\nu\nu} \quad , \qquad (1)$$

with the plasma frequency $\omega_p = 5.89x10^{15}$ 1/sec and the damping frequency $\nu = \omega_p / 100$. In order to look for interface waves, there should be at least one band gap below the plasma frequency, because for those conditions light can not propagate inside the 2DPC or the metal. We choose the size of the unit cell $L = \lambda_p = 320nm$. In the following we will use normalized frequencies $\varpi = \omega / \omega_L \omega$. We computed the effect of truncation of the surface cells on the dispersion relation of the modes. The truncation τ is defined as the fraction truncated to the surface cells, for example, $\tau = 0.05$ means that the side perpendicular to the surface of the cell was reduced by 5% or a distance 0.05 L.

3. Results.

Our results for the coupling of the interface modes with the waveguided modes for TE polarization are show in the figure 1, where the projected band structure with the allowed bands correspond to the blue symbols. The interface waves with a truncations of tau=0.55 are shown as the blue dash line, and the waveguide as the green dotted line, each computed alone. When both, interface and waveguides are computed together, i. e. the 2DPC with metal and with a line of defects, the red dotted line is obtained.

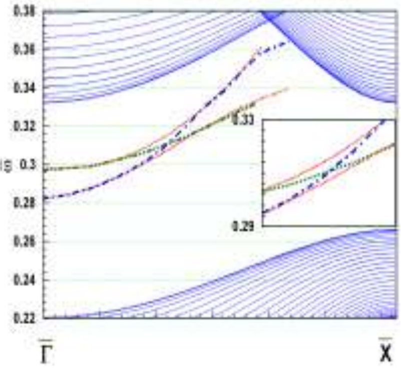

Fig. 1.The blue dot symbols are the projected bandstructure for TE polarization of a 2DPC. The red, blue and red lines inside the bandgap correspond to dispersion relations of interface modes as described in text.

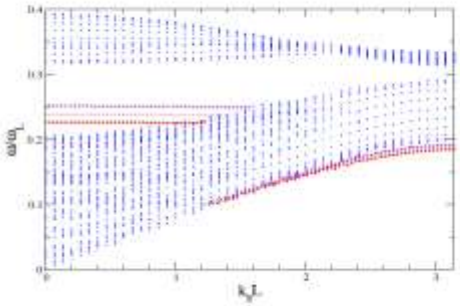

Fig. 2.The blue plus symbols are the projected bandstructure for TM polarization of a 2DPC. The red, brown and violet symbols correspond to dispersion relations of interface modes as described in text.

In figure 2, we show results for the interface waves for TM polarization, the blue crosses are the projected bulk band structure, and the complete surface line of cells are shown as red diamonds. The brown crosses corresponds to a truncation of 0.05 L of the surface cells, and the violet plus signs corresponds to a truncation of 0.10L.The dispersion relation curves that end at about $\varpi = 0.18\omega$ for the three truncations, corresponds to surface plasmons, with light confined to the interface because it can not propagate in the metal or in any of the two dielectrics forming the unit cell. The electromagnetic fields for these modes decays exponentially away from the interface. On the other hand, the curves inside the band gap corresponds to interface modes confined by the metal and by the 2DPC band gap. These curves show a very small dispersion for the whole range of wave vectors inside the band gap. The electromagnetic fields of these modes decay also exponentially away from the interface but they have superimposed the periodicity of the 2DPC.

4. References

[1] E. Yablonovitch, “Inhibited spontaneous emission in solid-state physics and electronics,” Phys Rev Lett **58,** 2059-2062 (1987).

[2] Robert D. Meade, Karl D. Brommer, Andrew M. Rappe, and J. D. Joannopoulos, “Electromagnetic Bloch waves at the surface of a photonic crystal” Phys Rev B **44**, 10961-10964 (1991).

[3] J. A. Gaspar-Armenta and F. Villa-Villa, “Electromagnetic surface waves at a metal 2D photonic crystal interface,” JOSA B **30**, 2271-2276 (2013).

[4] J. A. Gaspar-Armenta and F. Villa-Villa, “Couping of a 2D photonic crystal-metal surface wave to photonic crystal waveguide mode” J OPT **16**, 035501 (2014).

Understanding the origin of core-shell mode interactions in plasmonic tubes

J. M. Nápoles-Duarte[1*], M. A. Chavez-Rojo[1], M. E. Fuentes-Montero[1], L. M. Rodríguez-Valdez[1],
R. García-Llamas[2] and J. A. Gaspar-Armenta[2]

[1]*Universidad Autónoma de Chihuahua, Facultad de Ciencias Químicas*
Apartado Postal 669, Chihuahua, Chihuahua, 31125 México
[2]*Departamento de Investigación en Física, Universidad de Sonora*
Apartado Postal 5-88, Hermosillo, Sonora, 83190 México.
e-mail address: jnapoles@uach.mx

In this work we study the core shell mode interactions in silver tubes by writing the dispersion relation of a tube in terms of the corresponding radius for cylinders and holes. We have found that the determinant can be decomposed in terms of smaller determinants which have the form corresponding to cylinders and holes plus two new forms that include the interactions between the internal and external walls.

As it is known, the dispersion relation of infinite circular cylinders is obtained by solving a transcendental equation and very complete studies have been developed by authors like Novotny and Pfeiffer [1,2]. In this work, we are interested in the plasmon modes of infinite tubes for the two-dimensional transverse electric (TE) case and their dependence on the ratio of the internal and external radiuses. First we briefly present the theoretical derivation of the dispersion relation for cylinders and holes, and tubes.

Numerical studies of the efficiency of excitation of surface plasmon-polaritons by compact surface structures

Eugenio R. Méndez and Sergio de la Cruz
División de Física Aplicada,
Centro de Investigación Científica y de Educación Superior de Ensenada, B.C.
Carretera Ensenada-Tijuana No. 3918, Ensenada, B.C., 22860 México.

Although the basic properties of surface plasmon-polaritons (SPPs) have been known for some time, their importance for nano-photonic applications has produced a renewed interest on the subject. For the case of a flat metal surface in contact with vacuum, it is well known that SPPs cannot be excited directly by volume waves propagating in vacuum. Similarly, SPPs behave as guided waves that cannot escape from the metal vacuum interface.

The classical methods for exciting SPPs, like the Otto and Kretschmann configurations [1], are well-suited for the use of broad, highly collimated beams, but their implementation can be problematic in confined or miniaturized spaces. As the recent literature suggests [2-6], the coupling efficiency of propagating volume waves into SPP constitutes an important problem in the field of plasmonics. Defining the coupling efficiency as the ratio of the power in the excited SPP to the power of the incident beam, the best efficiencies obtained so far are around 50%. An improvement of this value is essential for the development of surface plasmon photonic circuits.

Here, we present calculations of the coupling efficiency of compact surface structures, such as steps, modified steps, grooves and ridges, as functions of their defining parameters (see Fig. 1). The calculations are based on an integral equation formulation of the scattering problem [6,7]. Based on the results for grooves, we have considered the coupling efficiency of surfaces that contains sequences of optimized grooves.

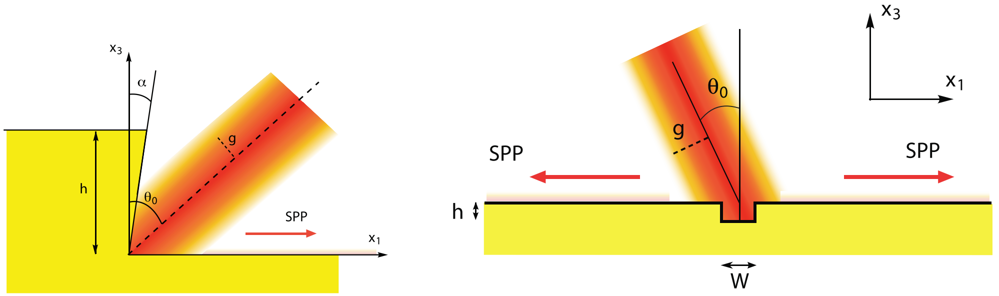

Fig. 1. Examples of compact structures for the excitation of SPPs. Angled corner (left) and groove (right).

The results show the efficiency of excitation depends strongly on the wavelength and the metal involved. So, besides considering the question of the optimal surface structure for the excitation of SPPs it also is interesting to consider the effect of dispersion and the optical properties of the materials. To address this question, we have also carried out calculations in which the wavelength is fixed, but the dielectric constant of the metal is varied over a realistic range. An example is shown in Fig. 2, where we present an efficiency map as a function of the real and imaginary parts of ε for an angled corner. From this kind of map, it is possible to choose the optimal wavelength for a given material or to choose between two different materials for a given wavelength.

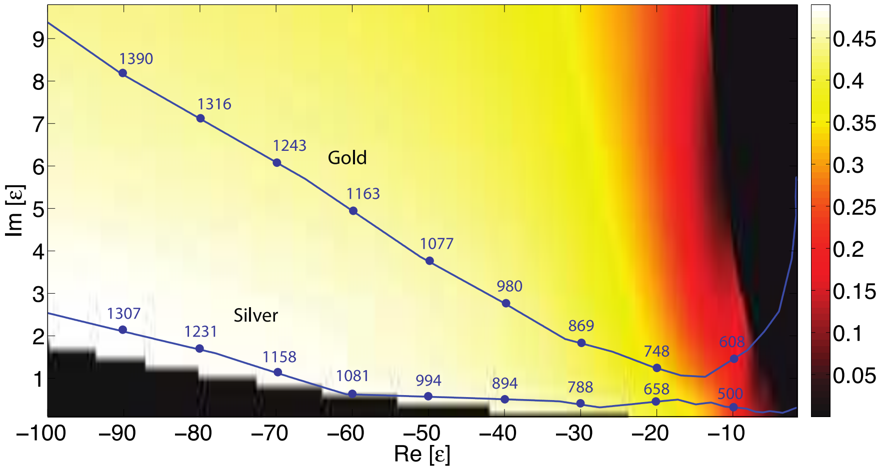

Fig. 2. Efficiency of excitation as a function of the real and imaginary parts of ε for an angled corner with $\alpha=18^0$. The labels in the curves for gold and silver represent the wavelength in nanometers.

References

[1] H. Raether, *Surface Plasmons on Smooth and Rough Surfaces and Gratings* (Springer-Verlag, Berlin, 1988).

[2] J. Lu, C. Petre, E. Yablonovitch, J. Conway, J. Opt. Soc. Am. B **24**, 2268 (2007).

[3] H. Liu, P. Lalanne, X. Yang, and J-P. Hugonin, IEEE J. Sel. Top. Quantum Electron. **14**, 1522 (2008).

[4] I. P. Radko, S. I. Bozhevolnyi, G. Brucoli, L. Martín-Moreno, F. J. García-Vidal, and A. Boltasseva, Opt. Expr. **17**, 7278 (2009).

[5] S. de la Cruz, E. R. Méndez, D. Macías, R. Salas-Montiel, and P. M. Adam, Phys. Status Solidi B **249**, 1178 (2012).

[6] X. Huang and M. L. Brongersma, Nano Lett. **13**, 5420 (2013).

[7] A. A. Maradudin, T. Michel, A. R. McGurn, and E. R. Méndez, Ann. Phys. (N. Y.) **203**, 255 (1990).

[8] A. Mendoza-Suárez and E. R. Méndez, Appl. Opt. **36**, 3521 (1997).

Sesión 5

Two-dimensional dispersive photonic crystals from the plane wave method

E. Guevara-Cabrera[1], M.A. Palomino-Ovando[1],
B. Flores-Desirena[1], ¤ and J. A. Gaspar-Armenta[2]

[1]Facultad de Ciencias Físico Matemáticas, Benemérita Universidad Autónoma de Puebla.
Apdo. Post. 165, Puebla, Pue. 72000, México.
[2]Centro de Investigación en Física de la Universidad de Sonora Apdo. Post.
5-088, Hermosillo Sonora 83190 México.

In this work we calculate the band structure of a two (2D)-dimensional photonic crystal (PC) which is characterized by a dispersive permittivity $\varepsilon(\boldsymbol{r},\omega)$ and permeability $\mu(\boldsymbol{r},\omega)$. From Maxwell's equations we find the dispersion relation for both polarizations, i.e., transverse magnetic polarization (TM) and transverse electric (TE) either the electric field or the magnetic field lie along the axis of the cylinders respectively. In calculating eigenvalues equation proceed similarly as in [1]. The eigenvalue equations for polarizations TM and TE are given by:

$$K^2+\mu_{\bar{G}-\bar{G}'}\mu^{-1}_{\bar{G}'-\bar{G}''}(\bar{G}'+\bar{G}'')\cdot\bar{K}+\mu_{\bar{G}-\bar{G}'}\mu^{-1}_{\bar{G}'-\bar{G}''}\bar{G}'\cdot\bar{G}''-k_0^2\,\mu_{\bar{G}-\bar{G}'}\varepsilon_{\bar{G}'-\bar{G}''}=0 \qquad (1)$$

$$K^2+\epsilon_{\bar{G}-\bar{G}'}\epsilon^{-1}_{\bar{G}'-\bar{G}''}(\bar{G}'+\bar{G}'')\cdot\bar{K}+\varepsilon_{\bar{G}-\bar{G}'}\varepsilon^{-1}_{\bar{G}'-\bar{G}''}\bar{G}'\cdot\bar{G}''-k_0^2\,\varepsilon_{\bar{G}-\bar{G}'}\mu_{\bar{G}'-\bar{G}''}=0 \qquad (2)$$

where the eigenvalues $\bar{K}$ are the Bloch wave vectors, $\bar{G}$ are the reciprocal lattice vectors, k_0 is the magnitude of the wave vector in vacuum and $\varepsilon_{\bar{G}-\bar{G}'}$, $\mu_{\bar{G}-\bar{G}'}$, $\epsilon^{-1}_{\bar{G}-\bar{G}'}$and $\mu^{-1}_{\bar{G}-\bar{G}'}$ are the Fourier coefficients of the permittivity, permeability and their inverses respectively. From the Eqs. (1) and (2) we can determine the eigenvalues $\bar{K}$ for a given frequency, whereby dispersive materials can be considered in the unit cell. With this method we have calculated the dispersion relation of one (1D)- and 2D-dimensional PCs with dispersive material and we have compared with those obtained from transfer matrix method for 1D PC, as can be from Figure 1 and the finite-difference time-domain method (FDTD) for 2D-PC, which is shown in Figure 2, we have obtained excellent agreement. We apply this method to calculate the band structure of a 2D PC of polar material rods on a metallic background, when the cross section of the array forms a square or triangular lattice. The optical responses of both polar material and metal are modeled through the Lorentz and Drude dielectric functions. We discuss the behavior of the effective plasma frequency and the gap-midgap ratio as function of the filling fraction.

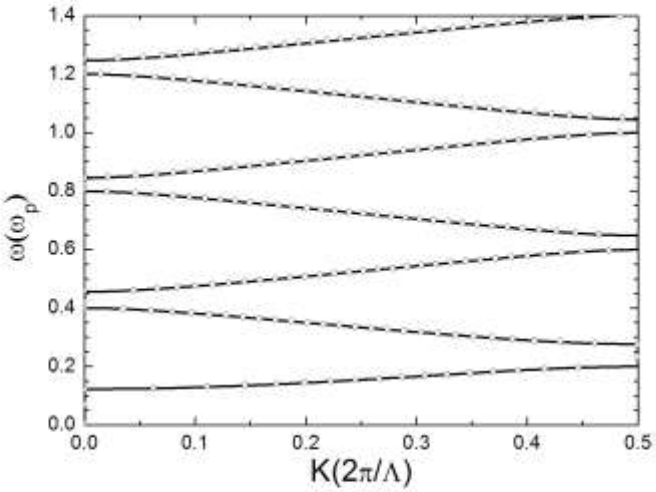

Figure 1. The photonic band structure of a 1D PC formed by alternating layers of metal and dielectric. The permittivity constant of dielectric is *2.25*, the metallic dielectric function is given by the Drude model and the filling fraction is *f = 5/105*. The solid curve corresponds to the calculation from the transfer matrix as in [2] and circles correspond to our calculation with nine waves.

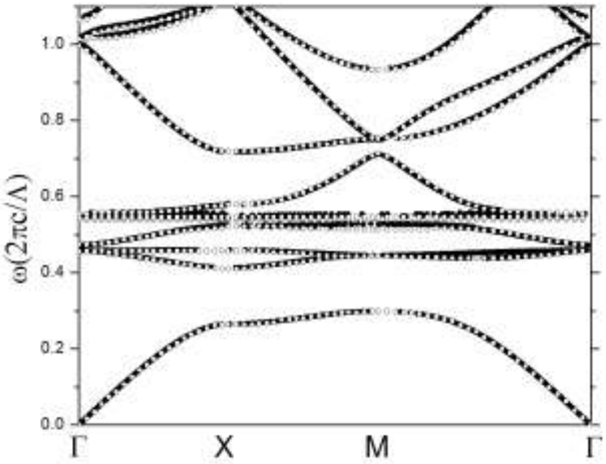

Figure 2. The photonic band structure of a 2D PC cylinders polar material formed of MgO distributed in a square lattice in air background with *f = 0.1*. We compare our results (solid line) with that obtained in [3] by the FDTD method (circles). A total of 289 plane waves are used in the Fourier series

[1] E. Istrate, A.A. Green, and E. H. Sargent, “Behavior of light at photonic crystal interfaces”, Phys. Rev. B **71**, 195122 (2005)

[2] X. Xu, Y. Xi, D. Han, X. Liu, J. Zi, and Z. Zhu, "Effective plasma frequency in one-dimensional metallic-dielectric photonic crystals", Appl. Phys. Lett. **86**, 091112 (2005)
[3] A. H. B. Ghasemi, S. Mandegarian, H. Kebriti and H. Latifi, "Bandgap generation and enhancement in polaritonic cylinder square-lattice photonic crystals" J. Opt. **14**, 055103 (2012)

Mid-infrared Otto Excitation of Transverse Electric Surface Plasmons in Doped Graphene

F. Ramos-Mendieta

Departamento de Investigación en Física, Universidad de Sonora
Apartado Postal 5-088, Hermosillo, Sonora, 83190 México

Transverse electric (TE) surface plasmons (SPs) are particular plasma excitations supported by doped graphene in frequency ranges where the imaginary component of the dynamical conductivity, $\sigma(\omega,\mu,T)$, is negative.[1] These are self-sustained current oscillations that result from the unique behavior of graphene as a gapless semiconductor with a conical point in the band structure.[2] For doped graphene of Fermi level μ, the Dirac theory of massless fermions with the Random-Phase Approximation or the Kubo formalism predict carrier transport with *intraband* and *interband* contributions.[3-5] TE SPs can exist only in a narrow frequency region just below the threshold of interband absorption $\hbar\omega = 2\mu$. Without a metallic counterpart, TE SPs are excitations free of induced charge — the total electric field that lies in the graphene plane is perpendicular to the plasmon wave vector. Therefore, TE SPs are physically different from the ordinary transverse magnetic (TM) SPs supported by metals - and by graphene itself.

In this talk I present the dispersion relation of these TE modes; particular analysis is made for the boundary conditions of the electromagnetic fields in presence of the planar surface current produced by the graphene conductivity and the electric field of the wave. Then, with Attenuated Total Reflection simulations we show the complicated reality to detect these extremely extended surface modes whose dispersion relation almost overlay the light line of vacuum.

For the graphene conductivity we use the function[1]

$$\sigma(\omega,\mu,\tau) = \frac{i}{\pi}\frac{e^2}{\hbar}\left[\frac{\mu}{\hbar(\omega+i\tau^{-1})} - \frac{1}{4}\ln\left(\frac{2\mu+\hbar(\omega+i\tau^{-1})}{2\mu-\hbar(\omega+i\tau^{-1})}\right)\right], \qquad (1)$$

where τ is the phenomenological relaxation time, e is the charge of an electron, $\hbar$ is the reduced Planck´s constant and μ is the Fermi level. TE surface plasmons exist only in the frequency region where the imaginary part of σ is negative. For example, with τ = 1 ps, we find that the imaginary component of Eq. (1) takes negative values within the frequency (wavelength) ranges: 80.6 THz < f < 96.6 THz (3.10 - 3.72μm) and 120.8 THz < f < 144.9 THz (2.0 – 2.48 μm), for μ = 0.2 eV and μ = 0.3 eV, respectively.

With graphene laying on the *x,y* plane, the Maxwell Equations predict the next connections of the fields on both sides ($z=0^-$ and $z=0^+$) of the graphene layer:

$$\hat{k}\times(\vec{E}_2-\vec{E}_1)=0, \qquad (2)$$

$$\hat{k}\times(\vec{H}_2-\vec{H}_1)=\sigma E_y\hat{j}, \qquad (3)$$

where $\hat{k}$ and $\hat{j}$ are the unit vectors on the z and y directions. In terms of the field components, these equations take the forms

$$E_{2y}-E_{1y}=0, \qquad H_{2x}-H_{1x}=\sigma E_{2y}. \qquad (4)$$

With Eqs. (4) we obtain the next dispersion relation of the TE SPs in a monolayer free-standing graphene: $q_z=-\frac{\omega\mu_0}{2}\sigma$. In general the product $\mu_0\sigma$ is small; thus, the SP wavevector approximates to $q_x\sim q_0(1+\frac{\eta_0^2\sigma_i^2}{8})$.

On the other hand, for the reflectivity of the system n_p/air/graphene/air (the Otto´s configuration) the corresponding system of four coupled equations can be manipulated algebraically to obtain the reflection coefficient

$$r=-\frac{r_{12}+r_{23}e^{2iq_{2z}d}}{1+r_{12}r_{23}e^{2iq_{2z}d}}, \qquad (7)$$

where $r_{12}=(q_{2z}-q_{1z})/(q_{2z}+q_{1z})$ and $r_{23}=(q_{3z}+\omega\mu_0\sigma-q_{2z})/(q_{3z}+\omega\mu_0\sigma+q_{2z})$. A series of results summarizing the physical properties of the TE SPs is presented in the conference.

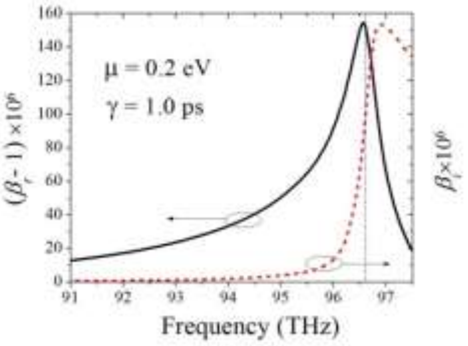

Figure 1. Dispersion relation of the TE SPs for doped graphene. $\beta=q_{xr}/q_0+iq_{xi}/q_0$. The scale of the two vertical axes is the same.

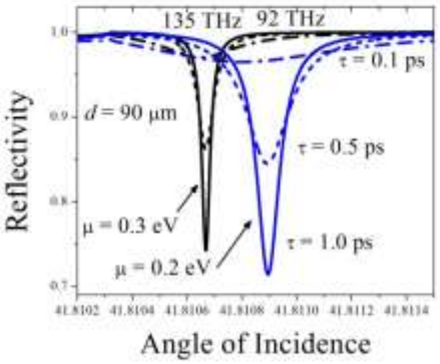

Figure 2. ATR profiles for free-standing graphene for two doping levels. With n_p = 1.5, the critical angle is $\theta_c=41.81031°$. Note the tiny angular window beyond the critical angle where the SPs are excited.

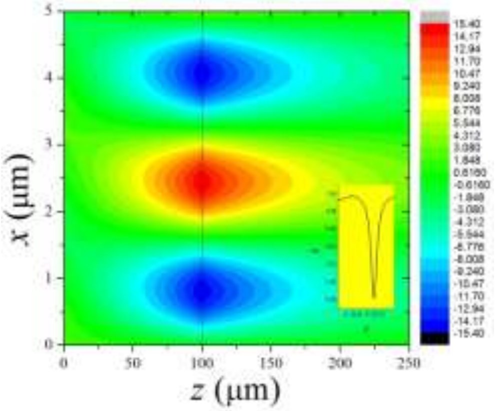

Figure 3. Electric field profile of a TE SP. The prism occupies the region $z < 0$. Note that this is an extremely extended mode of confinement distance around 50 times the plasmon wave length.

References:

1. S. A. Mikhailov and K. Ziegler, Phys. Rev. Lett. **99**, 016803 (2007)
2. M. I. Katsnelson, *Graphene: Carbon in Two Dimensions* (Cambridge University Press, New York, 2012).
3. T. Stauber, N. M. R. Peres, ans A. K. Geim, Phys. Rev. B **78**, 085432 (2008).
4. L. A. Falkovsky and S. S. Pershoguba, Phys. Rev. B **76**, 153410 (2007).
5. G. W. Hanson, J. Appl. Phys. **103**, 064302 (2008).

Fractal-like structure of magnetic field penetration into superconducting NbTi disc: stochastic jumps of flux bundles and Meissner holes

V. V. Chabanenko[1], E. I. Kuchuk[1], A.E. Philippov[1], V.F. Rusakov[2], O.M. Chumak[1,2], R. Cortés-Maldonado[3], F. Pérez-Rodríguez[3], I. Abal'osheva[4], A. Nabiałek[4]

[1]A. Galkin Donetsk Institute for Physics and Engineering, NASU, Donetsk, 83114, Ukraine
[2]Donetsk National University, 24 Universitetskaya str., 83001, Donetsk, Ukraine
[3]Instituto de Física, Benemérita Universidad Autónoma de Puebla, Puebla, México
[4]Institute of Physics, PAS, 02-668 Warsaw, Poland

e-mail: vikchabanenko@gmail.com

The magneto-optical technique [1] was used for the experimental study of the penetration of magnetic field into superconducting NbTi disc.

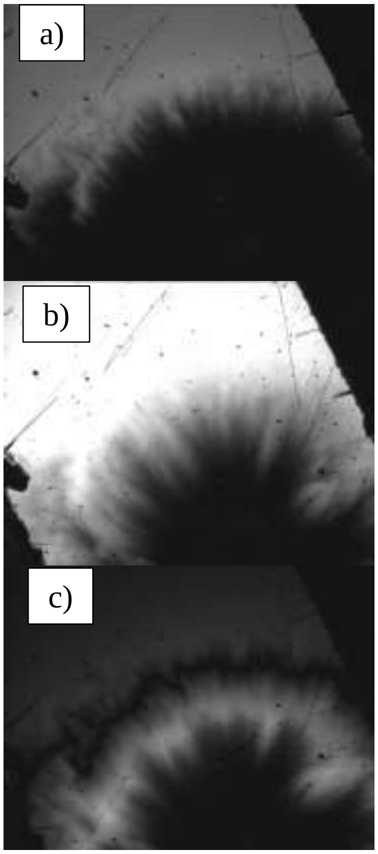

Fig. 1: Magneto-optical images of magnetic flux penetration into SC NbTi disc at the next magnetic field H: a)- 200G; b)- 600 G; c)- trapped flux; 0 G

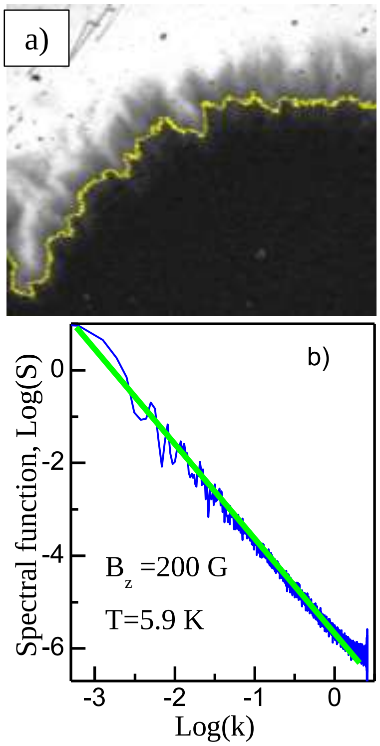

Fig. 1: a) - Flux pattern and profile near the flux front; b)- spectral function S(k).

This method provides a measure of the normal component of the induction B_z. Such a research can become a test of the self-organized criticality of vortices in a superconductor [2]. We observed the dynamics of the magnetic flux penetration into the superconducting NbTi disc at remagnetization in the range $0\rightarrow+600G\rightarrow0\rightarrow-600G\rightarrow0$ within the temperature interval 4,5K - 6K. The detail analysis of magneto-optical images of the vortex dynamics (Fig. 1a)-c)) reveals inhomogeneities and stochastic jumps of magnetic flux forming a rough penetration front. The local intensity is proportional to the B_z value. The next main features of the penetrated flux structure can be seen here:

a) The surface of induction inside the superconductor has a complicated (the “ridge” type) 3D-structure;

b) The boundary between Meissner and mixed states has a bending relief structure; it may be a consequence of vortices self-organized criticality [2];

c) There is a gate and a local flux entry channel associated with weak place in the superconductor as a result of material inhomogeneities (square on the image a));

d) The boundary between two oppositely magnetized portions of the disk is a black line of a certain thickness (presumably, this is Meissner hole [3, 4]), bending under certain conditions (image c).

The scaling analysis of flux profiles behind the front was done. Fast Fourier transformation of flux profile data *k* (Fig. 2a) yielded the spectral function *S*(*k*) of the surface. It has a power dependence on *k* (Fig 2b), similar to the results [2]. The roughness exponent α [5, 6] can be obtained from the tilt of dependence log*S(k)* vs log*(k)*. The Housdorff dimension of the rough surface D was defined using the obtained value *α*. Roughness exponent values are in the range 0.47-0.54 for the magnetic induction 150-400 *G*. As for Housdorff dimension, it lies in the range of 1.46-1.53, respectively. According to our analysis we can conclude that the penetration front of the magnetic flux into superconducting NbTi disc has fractal-like structure [2,7].

Thermomagnetic avalanches - critical state instability **-** are commonly observed in type-II hard superconductors (SC). The key quantity characterizing flux jump is the applied field, B_{fj}, when the first jump occurs in a ZFC superconductor [8,9]. The important features of stability in the fields less than B_{fj} are monotonously decreasing critical current density as function of magnetic field, the flux front (flat profile of induction) into the superconductor is essentially flat and so on. According to Fig. 1 the induction profile is not flat, but a "rocky mountain" slope. Consequently, the transformation from the straight current flow parallel to the specimen edge in the case of flat profile to the bending streamlines will occur [2]. As a result of concentric current flow lines the sharp peaks of increasing and decreasing in the magnetic flux distribution along bending streamlines will originate. The conventional theory of the thermomagnetic instability [8,9] predicts "uniform" flux jumps, where the flux front is essentially flat. In this announcement the role of induction (flux front) relief on the upper shielding limit of full critical state stability was discussed.

Acknowledgments. This work was partially supported by SEP-CONACYT (Mexico) under grant CB-2012-01-183673 and Polish National Science Center grant 2011/01/B/ST3/00462.

References

1. Ch. Jooss, J. Albrecht, H. Kuhn, S. Leonhardt and H. Kronmuller. / Magneto-optical studies of current distributions in high-Tc superconductors. // Rep. Prog. Phys. **65**, 651–788 (2002).
2. V. K. Vlasko-Vlasov U. Welp, V. Metlushko, and G. W. Crabtree. // Phys. Rev. B **69**, 140504(R), (2004).
3. V. K. Vlasko-Vlasov, U. Welp, G. W. Crabtree, et al. // Phys. Rev. *B* **56**, 5622 (1997).
4. E. H. Brandt. // Phys. Rev. B **58**, 6506 (1998).
5. J.M. Lopez and J. Schmittbuhl. // Phys. Rev. E **57**, 6405 (1998).
6. J.J. Ramasco, J.M. Lopez, and M.A. Rodriguez. // Phys. Rev. Lett. **84**, 2199 (2000).
7. T. Vicsek, Fractal Growth Phenomena (World Scientific, Singapore, New Jersey, 1992); A.-L. Barabasi and H.E. Stanley, Fractal Concepts in Surface Growth (Cambridge University Press, Cambridge, 1995); P. Meakin, Fractals, Scaling and Growth Far from Equilibrium (Cambridge University Press, Cambridge, 1998).
8. S. L. Wipf. // Phys. Rev. **161**, 404 (1967).
9. R.G. Mints, A.L. Rakhmanov. / Critical state stability in type-II superconductors and superconductor-normal-metal composites. // Rev. Mod. Phys. **53**, 551–592 (1981).

Posters II

Dynamical Modeling of the Radiation Emitted by a Luminescent Dye embedded in a slab

Y. J. Rodriguez-Viveros, B. Manzanares-Martinez, and P. Castro-Garay
Departamento de Fisica, Universidad de Sonora,
Blvd. Luis Encinas y Rosales, Hermosillo, Sonora 83000, Mexico
D. Moctezuma-Enriquez
Centro de Investigacion en Materiales Avanzados (CIMAV),
Miguel de Cervantes 120, Chihuahua 31109, Mexico
C. I. Ham-Rodriguez and J. Manzanares-Martinez
Departamento de Investigacion en Fisica, Universidad de Sonora,
Apartado Postal 5-088, Hermosillo, Sonora 83000, Mexico

The radiation emitted by a luminescent dye embedded in a planar waveguide is studied in the framework of the Classical Electrodynamics. The spontaneous emission of the luminescent dye is modeled as a Gaussian source of electromagnetic field. If the Gaussian source is placed at the center of the waveguide, a strong enhancement along the waveguide is obtained for the even modes. However, the odd modes can not be exited because for this case, the symmetries of the source and the modes are different. We have observed that when multiple even modes can be exited by the Gaussian source, the eigenmodes travels at distinct velocity along of the planar waveguide according to their group velocity. In this study we have proceeded in two steps. In the first step we consider he stationary case to determine the waveguide dispersion relation. The phase and group velocity have been numerically calculated directly from this dispersion relation. In a second step we model the propagation of the electromagnetic field by using the Finite Difference Time-Domain Method.

Inhomogeneous fields for Surface Plasmon Excitation

L. A. Mayoral-Astorga[1], J. A. Gaspar-Armenta[2], F. Ramos-Mendieta[2]

[1]Posgrado en Ciencias (Física), Universidad de Sonora, Blvd. Luis Encinas y Rosales S/N , Col., Hermosillo, Sonora, México.
[2]Departamento de Investigación en Física de la Universidad de Sonora, Blvd. Luis Encinas y Rosales, S/N, Hermosillo, Son. México.

Point sources of polarized light generate inhomogeneous fields at the surface of a metallic slab localized at its vicinity. The associated k-spectrum contains wave vectors larger than those corresponding to free oscillations. A surface plasmon arriving to the edge of a metal slab produces radiation of the corner in a way similar as a point source. Using the finite difference time domain method (FDTD), we analize the excitation of surface plasmons due to the inhomogeneous field of the radiating corner, on second contiguous metallic slab.

In a two dimensional system, a radiating cylindrical source produces surface projected electromagnetic fields that are highy inhomogeneous when the source is close to the surface. The spectrum of the wave vector parallel to the surface contains wave vectors that are larger than the vacuum wave vector for a given frequency. As a consecuence, localized sources close to the surface of a metal can produce surface plasmons (Ref. 1)

A surface plasmon arriving to the edge of a metallic slab, produces radiation from the corner of the slab as shown in the figure 1. The radiation is highly directional in the direction of the SP, with a weak cylindrical component.

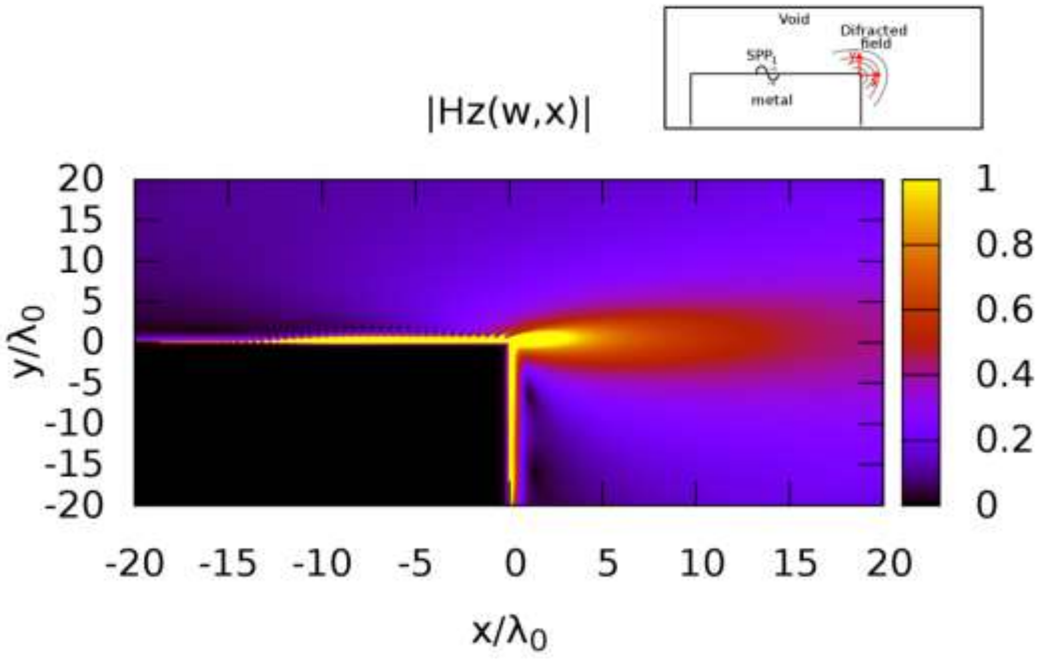

If we locate a second slab close to the first, forming a slit of thickness d, as shown in the inset of figure 2, when a SP arrives at the corner, a SP is observed on the second slab. The mechanism for the formation of the SP on the second slab is explained as follows. The radiation of the corner due to the first SP induces that the corner of the second slab starts radiating and its inhomogeneous fields at the surface produces the SP. Even when the inhomogeneous field of the first corner may produce SP, the radiating of the second corner dominates because the inhomogenity is on-site.

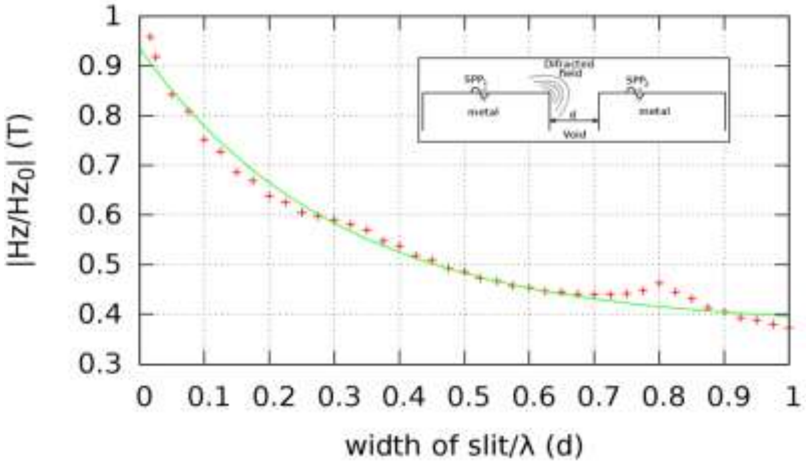

In this figure, we show the intensity of the H field at a fixed point at the surface of the second slab, as a function of the thickness of the slit. The intensity of the filed decays because of the radiation arriving at the second corner is smaller as the slit thickness increases.

In the following figure we show the H field from a FDTD simulation of a SP diffracting in the corner, and when another metal plane is located as shown in the inset, a distance 0.5 λ_0 , where λ_0 is the wavelength of the light in vacuum.

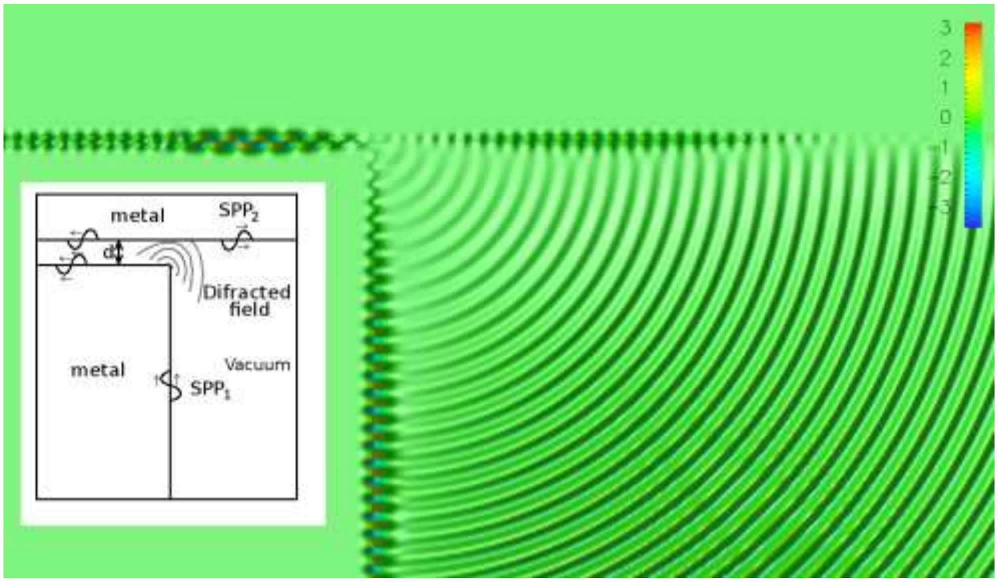

References.
1.J. Gaspar-Armenta, L. A. Mayoral-Astorga, F. Ramos-Mendieta, Proc. of SPIE Vol. 8011 80115I-1

In-plane vibrations of a rectangular plate: plane-wave expansion modelling and experiment

A. Arreola-Lucas[a] , G. Báez[a] , J. A. Franco-Villafañe[b], R. A. Méndez-Sánchez[b]

[a]Departamento de Ciencias Básicas, Universidad Autónoma Metropolitana-Azcapotzalco, Av San Pablo 180, Col. Reynosa Tamaulipas, 02200 México DF, México.
[b]Instituto de Ciencias Físicas, Universidad Nacional Autónoma de México, A.P. 48-3, 62251 Cuernavaca, Morelos, México.

The in-plane vibrations of plates have gained interest recently since it has been shown that they appear in digital storage systems when following narrow data tracks [1]. It has been also shown in the design of ship hulls that in-plane vibrations are strongly related with the high-frequency noise [2]. In this work experimental results for in-plane vibrations of a uniform rectangular plate with free boundary conditions are shown [3]. For the modelling the plane wave expansion method is used [3-5]. The experimental setup uses electromagnetic-acoustic transducers and a vector network analyzer [6]. Some measured normal-mode wave amplitudes are compared with the theoretical predictions; very good agreement is observed. The excellent agreement of the classical theory of in-plane vibrations confirms its reliability up to very high frequencies

The experiments were realized using the technique known as resonant acoustic spectroscopy [6]. In the latter a one-frequency signal is sent to the plate, to produce vibrations and its response is measured. The frequency is sweept and a characteristic spectrum of the plate is obtained. The experimental setup is shown in Fig. 1. It consists of a Vector Network Analyzer (VNA Anritsu MS4630B), a high-fidelity audio amplifier (Cerwin-Vega CV900), and two electromagnetic-acoustic transducers (EMATs). The VNA produces a sinusoidal signal of frequency *f* which is sent to the audio amplifier that works in the frequency range from 20 Hz up to 20 kHz. After the amplification stage, the signal is sent to the EMAT-exciter which produces a vibration on the plate. The response of the plate is measured by the EMAT-detector whose output is sent to the VNA. The VNA extracts the response at the frequency *f* using the lock-in amplifier technique. The VNA is controlled by a workstation through the GPIB port and the norm and phase of the response are digitalized there.

The EMATs are transducers highly selective to the different kinds of vibrations [7]. Each transducer consists of a coil and a magnet. We used two different configurations to excite and detect in-plane vibrations. In the first one, the coil exciter axis coincide with the magnet axis and both exciter axes lie on the plane of the plate (See the inset of Fig. 1) in the long side of the plate; the detector axes also lie on the plane of the plate in a orthogonal direction to the exciter axes. In the second configuration, used to measure the normal-mode wave amplitudes, the exciter axes are as in the previous configuration and the detector axes are perpendicular one to each other and both to the normal to the plate.

To obtain a theoretical prediction, the equations for in-plane vibrations were used among with a plane wave expansion. The plate was surrounded by a matrix plate to form a unit cell that is repeated periodically. Using Bloch's theorem a generalized eigenvalue problem, solved numerically, is obtained.

The measured spectrum is shown in Fig. 2 from 500 Hz to 20 kHz. The plane-wave expansion prediction is also given in the upper part of the same figure with the vertical lines. The shape of the normal-modes was also measured (See Fig. 3). It was obtained fixing the frequency of the signal generated by the VNA to a resonant peak of Fig. 2. The data were collected in a quarter of plate only. To obtain the full wave amplitude the measurements were reflected in both sides. The theory shows an excellent agreement with the experiment both in the spectrum and wave amplitudes.

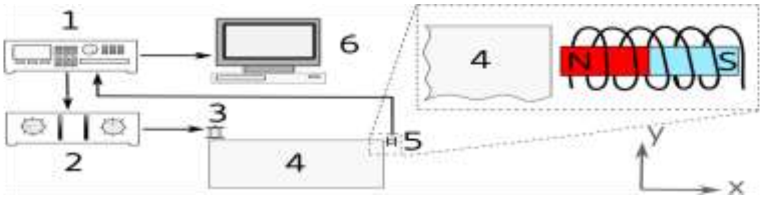

Figure 1: Block diagram of the setup. The Vector Network Analyzer or VNA (1) generates a sinusoidal voltage that is sent to the high-fidelity audio amplifier (2). The output of the amplifier is sent the EMAT exciter (3) which produces in-plane vibrations in the plate (4). The vibrations are measured by the EMAT detector (5) whose output comes back to the VNA. The measured signal is digitalized by a workstation (6) through a GPIB port. A detail of the EMAT is given in the inset.

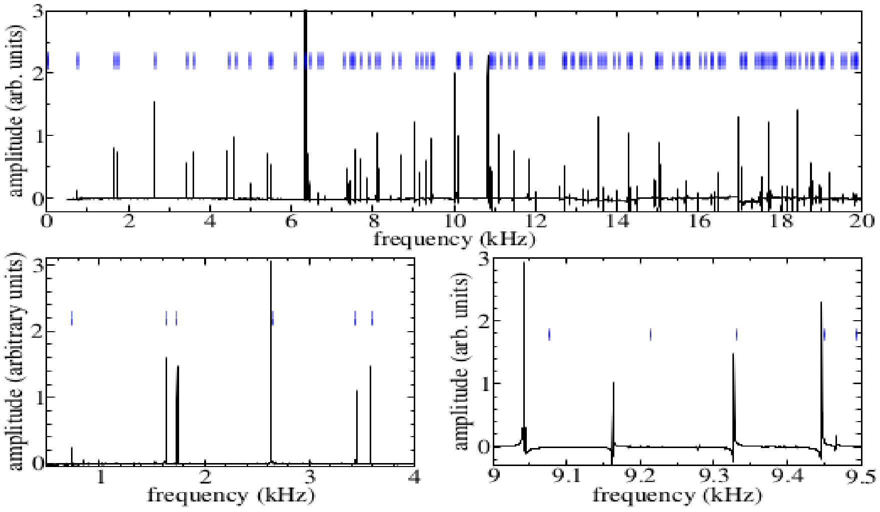

Figure 2: Resonant spectrum for in-plane vibrations of a rectangular aluminum plate of 1474 mm X 355 mm X 6.35 mm..

The continuous line is the experimental result while the vertical lines in the upper part correspond to the plane wave expansion. In the lower part zooms of the spectrum are given.

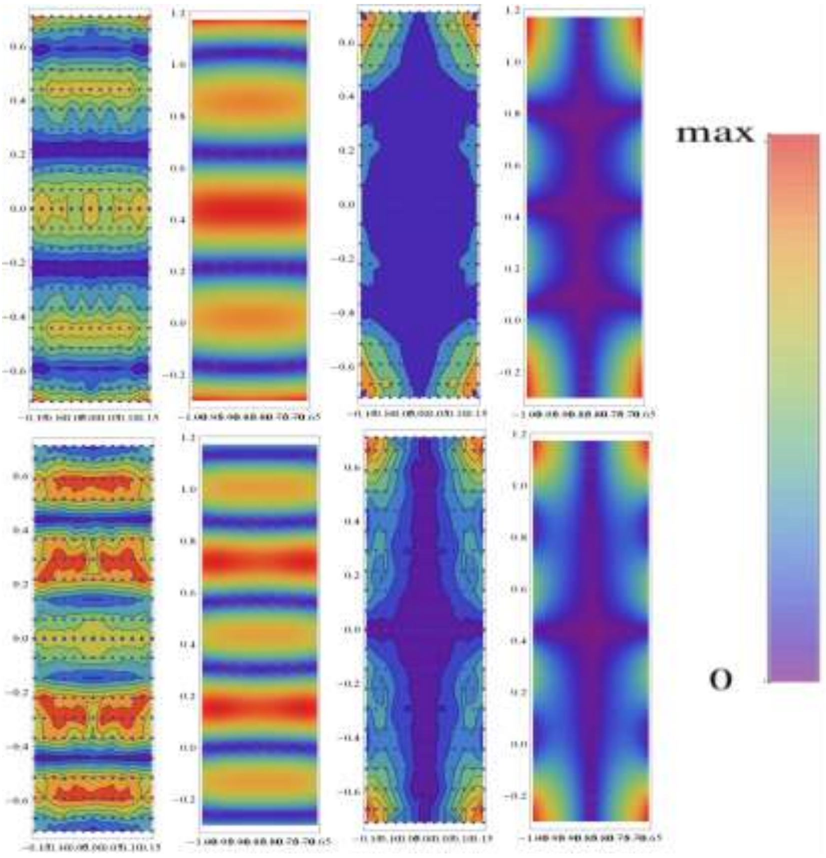

Figure 3: Measured and computed wave amplitudes for the normal modes of the rectangular plate. In the upper and lower parts are given the mode shapes for resonances with frequencies 2634 Hz and 4434 Hz, respectively. In the first and second columns the displacement in the horizontal direction is given while in the third and fourth columns the displacement in the vertical direction is given. The first and third columns correspond to experimental results while the second and fourth columns to numerical results. In the right part the scale of displacements is given.

References

[1] K. Hyde, J.Y. Chang, C. Bacca, J.A. Wickert, Parameter studies for plane stress in-plane vibration of rectangular plates, Journal of Sound and Vibration 247 (2001) 471--487.

[2] D.J. Gorman, Free in-plane vibration analysis of rectangular plates by the method of superposition, Journal of Sound and Vibration 272 (2004) 831--851.

[3] In-plane vibrations of a rectangular plate: plane wave expansion modelling and experiment
A. Arreola-Lucas , J. A. Franco-Villafañe, G. Báez, and R. A. Méndez-Sánchez, Journal of Sound and Vibration (*in press*).

[4] B. Manzanares-Martínez, J. Flores, L. Gutiérrez, R.A. Méndez-Sánchez, G. Monsivais, A. Morales, F. Ramos-Mendieta, Flexural vibrations of a rectangular plate for the lower normal modes, Journal of Sound and Vibration 329 (2010) 5105--5115.

[5] B. Manzanares-Martínez, F. Ramos-Mendieta, A. Baltazar, Ultrasonic elastic modes in solid bars: An application of the plane wave expansion method, Journal of the Acoustical Society of America 127 (2010) 3503--3510.

[6] J.A. Franco-Villafañe, E. Flores-Olmedo, G. Báez, O. Gandarilla-Carrillo and R.A. Méndez-Sánchez, Acoustic resonance spectroscopy for the advanced undergraduate laboratory, European Journal of Physics 33 (2012) 1761--1769.

[7] A. Morales, L. Gutiérrez, J. Flores, Improved eddy current driver-detector for elastic vibrations, American Journal of Physics 69 (2001) 517--522.

In-plane vibrations of a rectangular plate: plane-wave expansion modelling and experiment

A. Arreola-Lucas[a] , G. Báez[a] , J. A. Franco-Villafañe[b], R. A. Méndez-Sánchez[b]

[a]Departamento de Ciencias Básicas, Universidad Autónoma Metropolitana-Azcapotzalco, Av San Pablo 180, Col. Reynosa Tamaulipas, 02200 México DF, México.
[b]Instituto de Ciencias Físicas, Universidad Nacional Autónoma de México, A.P. 48-3, 62251 Cuernavaca, Morelos, México.

The in-plane vibrations of plates have gained interest recently since it has been shown that they appear in digital storage systems when following narrow data tracks [1]. It has been also shown in the design of ship hulls that in-plane vibrations are strongly related with the high-frequency noise [2]. In this work experimental results for in-plane vibrations of a uniform rectangular plate with free boundary conditions are shown [3]. For the modelling the plane wave expansion method is used [3-5]. The experimental setup uses electromagnetic-acoustic transducers and a vector network analyzer [6]. Some measured normal-mode wave amplitudes are compared with the theoretical predictions; very good agreement is observed. The excellent agreement of the classical theory of in-plane vibrations confirms its reliability up to very high frequencies

The experiments were realized using the technique known as resonant acoustic spectroscopy [6]. In the latter a one-frequency signal is sent to the plate, to produce vibrations and its response is measured. The frequency is sweept and a characteristic spectrum of the plate is obtained. The experimental setup is shown in Fig. 1. It consists of a Vector Network Analyzer (VNA Anritsu MS4630B), a high-fidelity audio amplifier (Cerwin-Vega CV900), and two electromagnetic-acoustic transducers (EMATs). The VNA produces a sinusoidal signal of frequency *f* which is sent to the audio amplifier that works in the frequency range from 20 Hz up to 20 kHz. After the amplification stage, the signal is sent to the EMAT-exciter which produces a vibration on the plate. The response of the plate is measured by the EMAT-detector whose output is sent to the VNA. The VNA extracts the response at the frequency *f* using the lock-in amplifier technique. The VNA is controlled by a workstation through the GPIB port and the norm and phase of the response are digitalized there.

The EMATs are transducers highly selective to the different kinds of vibrations [7]. Each transducer consists of a coil and a magnet. We used two different configurations to excite and detect in-plane vibrations. In the first one, the coil exciter axis coincide with the magnet axis and both exciter axes lie on the plane of the plate (See the inset of Fig. 1) in the long side of the plate; the detector axes also lie on the plane of the plate in a orthogonal direction to the exciter axes. In the second configuration, used to measure the normal-mode wave amplitudes, the exciter axes are as in the previous configuration and the detector axes are perpendicular one to each other and both to the normal to the plate.

To obtain a theoretical prediction, the equations for in-plane vibrations were used among with a plane wave expansion. The plate was surrounded by a matrix plate to form a unit cell that is repeated periodically. Using Bloch's theorem a generalized eigenvalue problem, solved numerically, is obtained.

The measured spectrum is shown in Fig. 2 from 500 Hz to 20 kHz. The plane-wave expansion prediction is also given in the upper part of the same figure with the vertical lines. The shape of the normal-modes was also measured (See Fig. 3). It was obtained fixing the frequency of the signal generated by the VNA to a resonant peak of Fig. 2. The data were collected in a quarter of plate only. To obtain the full wave amplitude the measurements were reflected in both sides. The theory shows an excellent agreement with the experiment both in the spectrum and wave amplitudes.

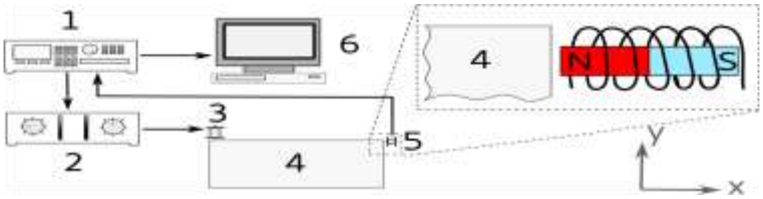

Figure 1: Block diagram of the setup. The Vector Network Analyzer or VNA (1) generates a sinusoidal voltage that is sent to the high-fidelity audio amplifier (2). The output of the amplifier is sent the EMAT exciter (3) which produces in-plane vibrations in the plate (4). The vibrations are measured by the EMAT detector (5) whose output comes back to the VNA. The measured signal is digitalized by a workstation (6) through a GPIB port. A detail of the EMAT is given in the inset.

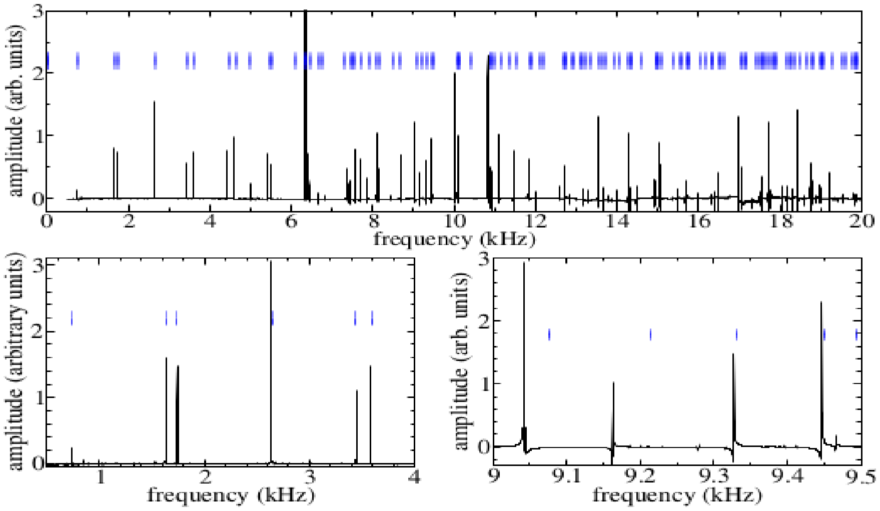

Figure 2: Resonant spectrum for in-plane vibrations of a rectangular aluminum plate of 1474 mm X 355 mm X 6.35 mm.. The continuous line is the experimental result while the vertical lines in the upper part correspond to the plane wave expansion. In the lower part zooms of the spectrum are given.

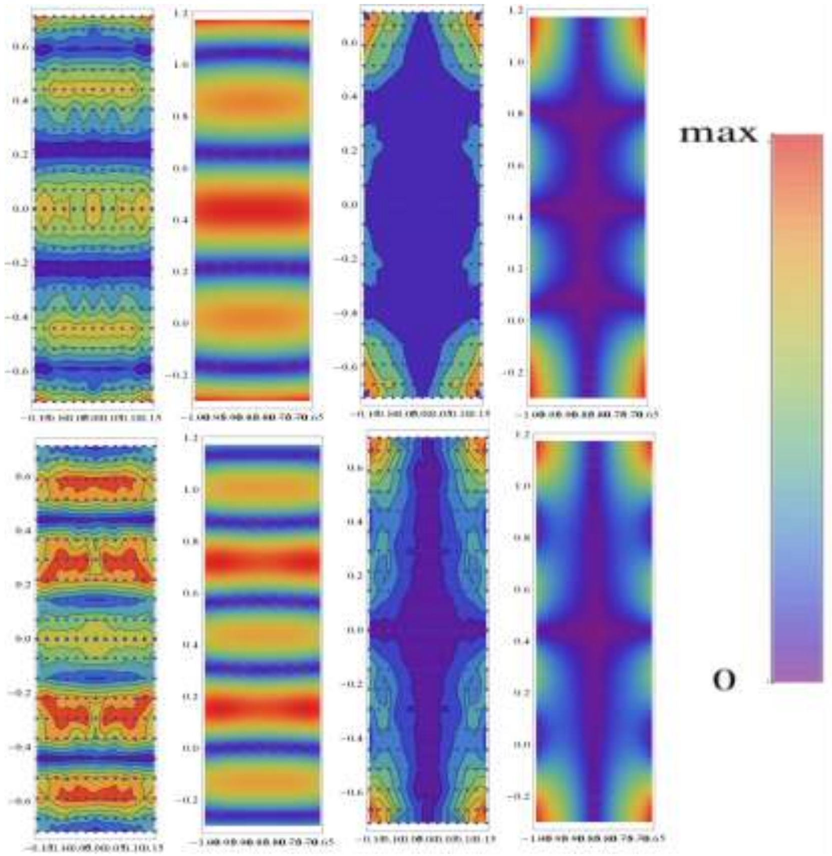

Figure 3: Measured and computed wave amplitudes for the normal modes of the rectangular plate. In the upper and lower parts are given the mode shapes for resonances with frequencies 2634 Hz and 4434 Hz, respectively. In the first and second columns the displacement in the horizontal direction is given while in the third and fourth columns the displacement in the vertical direction is given. The first and third columns correspond to experimental results while the second and fourth columns to numerical results. In the right part the scale of displacements is given.

References

[1] K. Hyde, J.Y. Chang, C. Bacca, J.A. Wickert, Parameter studies for plane stress in-plane vibration of rectangular plates, Journal of Sound and Vibration 247 (2001) 471--487.

[2] D.J. Gorman, Free in-plane vibration analysis of rectangular plates by the method of superposition, Journal of Sound and Vibration 272 (2004) 831--851.

[3] In-plane vibrations of a rectangular plate: plane wave expansion modelling and experiment
A. Arreola-Lucas , J. A. Franco-Villafañe, G. Báez, and R. A. Méndez-Sánchez, Journal of Sound and Vibration (*in press*).

[4] B. Manzanares-Martínez, J. Flores, L. Gutiérrez, R.A. Méndez-Sánchez, G. Monsivais, A. Morales, F. Ramos-Mendieta, Flexural vibrations of a rectangular plate for the lower normal modes, Journal of Sound and Vibration 329 (2010) 5105--5115.

[5] B. Manzanares-Martínez, F. Ramos-Mendieta, A. Baltazar, Ultrasonic elastic modes in solid bars: An application of the plane wave expansion method, Journal of the Acoustical Society of America 127 (2010) 3503--3510.

[6] J.A. Franco-Villafañe, E. Flores-Olmedo, G. Báez, O. Gandarilla-Carrillo and R.A. Méndez-Sánchez, Acoustic resonance spectroscopy for the advanced undergraduate laboratory, European Journal of Physics 33 (2012) 1761--1769.

[7] A. Morales, L. Gutiérrez, J. Flores, Improved eddy current driver-detector for elastic vibrations, American Journal of Physics 69 (2001) 517--522.

Cristal fotónico 1-D de componentes magnetoreológicas sintonizable con campo magnético

D. Marquez-Ruiz[1], F. Ramos-Mendieta[2],
B. Manzanares-Martínez[3]

[1]Posgrado en Nanotecnología, Universidad de Sonora. [2]Departamento de Investigación en Física, Universidad de Sonora. [3]Departamento de Física, Universidad de Sonora

Un cristal fonónico es una estructura conformada por dos o más materiales dispuestos de forma periódica. El sistema está definido por una celda unitaria compuesta por materiales elásticos, la cual es repetida en los puntos de una red de Bravais. La propagación de ondas mecánicas en un cristal fonónico depende de la geometría de la celda unitaria y de parámetros tales como la densidad, el módulo de corte y el módulo de Young. La principal característica de los cristales fonónicos es que presentan una estructura de bandas para la propagación de ondas elásticas. La existencia de las bandas de frecuencias prohibidas se debe a la variación periódica de la densidad (ρ), velocidad de sonido longitudinal (c_l) y transversal (c_t) en el sistema [1].

Es posible diseñar cristales fonónicos en los cuales se tenga la posibilidad de sintonizar sus bandas de frecuencias prohibidas mediante la aplicación de estímulos externos evitando el contacto directo con la muestra es variando la temperatura del cristal [2], mediante su exposición al campo eléctrico [3] o bien al campo magnético [4].

Estudiaremos la propagación de ondas elásticas en cristales fonónicos de periodicidad unidimensional en las cuales una de las componentes es magnetoreológica, es decir, sus propiedades son susceptibles de variación con el campo magnético [5]. Un fluido magnetoreológico (MRE) es aquel que tiene partículas suspendidas en el rango de los 100nm-10μm [6].

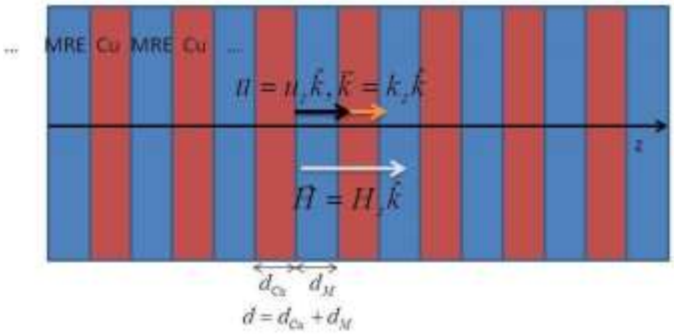

Figura 1. Esquema del problema de estudio. El eje z es paralelo al eje de la multicapa periódica conformada por placas de cobre alternadas con un material magnetoreológico. Las ondas longitudinales se propagan paralelas al eje de la superred al tiempo que un campo magnético en dirección *z* es aplicado.

En la Figura 1 se ilustra la situación a estudiar, el sistema consiste de capas de cobre de anchura d_{Cu}, alternadas con capas de un fluido magnetoreológico (MRE) de anchura d_M. Esta celda unitaria de anchura $d = d_{Cu} + d_M$ se repite en el espacio conformando un sistema de periodicidad unidimensional.

Analizaremos las ondas longitudinales cuyo vector de onda tienen dirección normal a las capas del cristal fonónico. Para el presente trabajo utilizamos el MRE propuesto por M. A. Bramantya et al en la referencia [6] consistente en partículas de hierro de 3-10µm suspendidas en un aceite de hidrocarbonos; cuya fracción del volumen entre las partículas y el fluido es 0.32. Los parámetros materiales para el sistema sin campo magnético externo son:

$$\begin{aligned} \rho_{Cu} &= 8930 kg/m^3, \\ c_{Cu} &= 4660 m/s, \\ \rho_M &= 3080 kg/m^3, \\ c_M &= 803.79 m/s. \end{aligned} \tag{1}$$

El factor de llenado $f = 0.5$. Los valores para el cobre fueron tomados de la Ref. [7] , estos no se ven alterados por variaciones en el campo magnético en el rango que manejaremos. Por otra parte, consideraremos despreciables los cambios de la densidad del MRE, atendiendo únicamente los efectos que el campo ejerce sobre la velocidad de sonido longitudinal. Esta dependencia está representada en la Figura 2 donde tenemos los valores de la velocidad de sonido longitudinal para el fluido MRE conforme aumenta el valor del campo magnético aplicado, estos valores se estimaron considerando los resultados presentados en la Ref. [6].

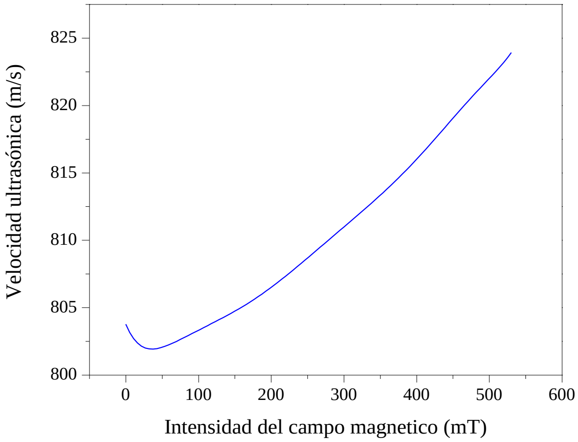

Figura 2. Dependencia de velocidad de sonido longitudinal con el campo magnético en el fluido magnetoreológico.

Para estudiar el sistema utilizaremos la segunda ley de Newton en el marco de la Mecánica del Medio Continuo:

$$\rho \frac{\partial^2 u_i}{\partial t^2} = \frac{\partial \sigma_{ij}}{\partial x_j}. \tag{2}$$

Donde u_i es la amplitud de la oscilación elástica en la dirección iésima y σ_{ij} es el tensor de esfuerzos. Cuando se considera la interacción magnetoelástica hay varias maneras de abordar la ecuación (2), una de las más apropiadas para el cálculo en sistemas periódicos es el del modelo que considera al material sensible al campo magnético a manera de un "piezomagnético" [8].

En el sistema que estamos estudiando, mostrado en la Figura 1, adoptamos una visión más simplificada del problema tal como han hecho otros autores es geometrías similares [9], la ecuación a resolver se simplifica entonces a:

$$\rho \frac{\partial^2 u_z}{\partial t^2} = \frac{\partial}{\partial z}\left(\overline{\rho c_l^2}\, \frac{\partial u_z}{\partial z}\right). \qquad (4)$$

En la ecuación anterior $\overline{\rho c_l^2}$ corresponde a un módulo elástico [10] que contiene los efectos del campo magnético sobre el mismo. El valor de $\overline{\rho c_l^2}$ para cada valor del campo magnético externo lo obtenemos a partir de los parámetros mostrados en (1) y la velocidad de sonido graficada en la Figura 1.

Para resolver la ec. (4) utilizamos el Método de Desarrollo en Ondas Planas el cual consiste en escribir los parámetros materiales del sistema de la siguiente manera:

$$\begin{aligned} \rho(z) &= \sum_{z} \rho(G_z) e^{iG_z z}, \\ \overline{\rho(z) c_l^2(z)} &= \sum_{z} \Lambda(G_z) e^{iG_z z}. \end{aligned} \qquad (5)$$

Donde $G_z = \frac{2\pi}{d} n$ es el vector de la red recíproca unidimensional. Estos desarrollos serán sustituidos en la ecuación de onda (4). Debido a la periodicidad del sistema buscamos soluciones que cumplan con el teorema de Bloch. Es decir, el desplazamiento elástico tendrá la forma $u_z(z,t) = e^{i(k_z z - \omega t)} u_k(z)$, donde $u_k(z) = u_k(z+d)$ y k_z es el vector de Bloch. Desarrollando u_k en ondas planas la solución final toma la forma:

$$u_z(z,t) = e^{i(k_z z - \omega t)} \sum_{G_z} u_k(G_z) e^{iG_z z}. \qquad (6)$$

Sustituyendo las ecs. (5) y (6) en (4) ¿, se puede llegar a la ecuación de eigenvalores

$$\mathrm{M}_{zz} \mathrm{u}_k(G'_z) = \omega^2 \mathrm{N} \mathrm{u}_k, \qquad (7)$$

donde u_k son las componentes del desplazamiento del desarrollo en ondas planas, M_{zz} y N son matrices que son funciones del vector de onda de Bloch, G_z. G'_z y los desarrollos (5). Las bandas mostradas en la Figura 3 fueron calculadas con una base de 301 ondas planas.

En la Figura 3 tenemos la sexta, séptima y octava bandas longitudinales del sistema. Se puede observar un aumento del 67% en el ancho de la banda prohibida entre la séptima y octava banda, comparando su punto más angosto ubicado en 37mT y su punto más ancho en 530mT . Por otra parte, el ancho del gap entre la sexta y la séptima banda tiene una disminución del 15%, comparando los valores en 37mT y 530mT.

En conclusión, es posible construir cristales fonónicos con materiales magnetoreológicas cuyas bandas sean dependientes del campo magnético. Por otra, se abre una serie de posibilidades de estudio, como son los efectos de la histéresis, el análisis de la anisotropía generada en el material magnetoreológico al aplicar el campo magnético y su efecto en la estructura de bandas, entre otras.

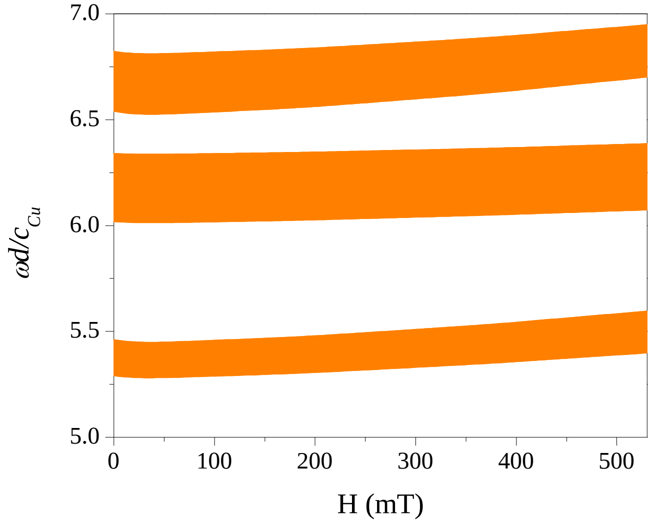

Figura 3. Dependencia de la estructura de bandas de las ondas longitudinales con el aumento del campo magnético externo aplicado.

Agradecimientos: Al proyecto CONACYT CB-2008/104151 por su financiamiento.

Bibliografía

1. SIGALAS M.M., E. E. N. Band structure of elastic waves in two-dimensional systems. **Solid State Commun.**, v. 86, p. 141-143, 1993.
2. HUANG Z. G., W. T. T. Temperature Effect on the Bandgaps of Surface and Bulk Acoustic Waves in Two-Dimensional Phononic Crystal. **IEEE Transactions on Ultrasonics, Ferroelectrics and Frequency Control**, v. 52, p. 365 - 370, 2005.
3. G., S. Electrostatically tunable band gaps in finitely extensible dielectric elastomer. **International Journal of Solids and Structures**, v. 50, p. 680.
4. MATAR, O. B. E. A. Band gap tunability of magneto-elastic phononic crystal. **Journal of Applied Physics**, v. 111, p. 054901, 2012.
5. RODRIGUEZ-LOPEZ, J. E. A. Ultrasonic velocity and amplitude characterization of magnetorheological fluids under magnetic fields. **Journal of Magnetism and Magnetic Materials**, v. 324, p. 222-230, 2012.
6. BRAMANTAYA, M. A. E. A. Ultrasonic propagation velocity in magnetic and magnetorheological fluids due to an external magnetic field. **J. Phys.: Condens. Matter**, v. 22, p. 324102, 2010.
7. TRIBIKRAM, K. **Ultrasonic Nondestructive Evaluation**. [S.l.]: CRC Press, 2003.
8. BOU MATAR, O. E. A. Band gap tunability of magneto-elastic phononic crystal. **Journal of Applied Physics**, v. 111, p. 054901, 2012.
9. XU, Z. Elastic band gaps of magnetorheological elastomer vibration isolators. **Journal of Intelligent Material Systems and Structures**, p. 1-7, 2014.
10. DING, R. E. A. Tunability of longitudinal wave band gaps in one dimensional phononic crystal with magnetostrictive material. **Journal of Applied Physics**, v. 115, p. 074104, 2014.

Excitation of surface plasmons on graphene via ATR and multilayer graphene study for TM polarization

J. Alejandro Hernández-López[1], M. A. Palomino-Ovando[1] and F. Ramos-Mendieta[2]

[1] Facultad de Ciencias Físico-Matemáticas. Benemérita Universidad Autónoma de Puebla. Puebla, Puebla, México.
[2] Centro de investigación en Física. Universidad de Sonora. Hermosillo, Sonora, México.

Graphene consists of a hexagonal arrangement of carbon atoms whose thickness is of the order of the diameter of an atom ($10^{-9}\,m$). For the study of its optical and electrical properties, graphene is characterized by a surface conductivity,σ, described by the Kubo formalism in the limit of low energies, $\hbar\omega \ll \mu_c$, for high doped graphene [1]

$$\sigma_{intra} = \frac{ie^2}{\pi\hbar}\frac{1}{\Omega+i\nu},$$

$$\sigma_{inter} = \frac{e^2}{4\hbar}\left[1+\frac{i}{\pi}ln\frac{\Omega+i\nu-2}{\Omega+i\nu+2}\right],$$

where, $\sigma = \sigma_{intra} + \sigma_{inter}$, $\Omega = {}^{\hbar\omega}/_{\mu_c}$, $\nu = {}^{\hbar\tau^{-1}}/_{\mu_c}$. Due to the properties of this conductivity, there are regions of frequency (Figure 1) where surface waves of TE and TM polarization can exist.

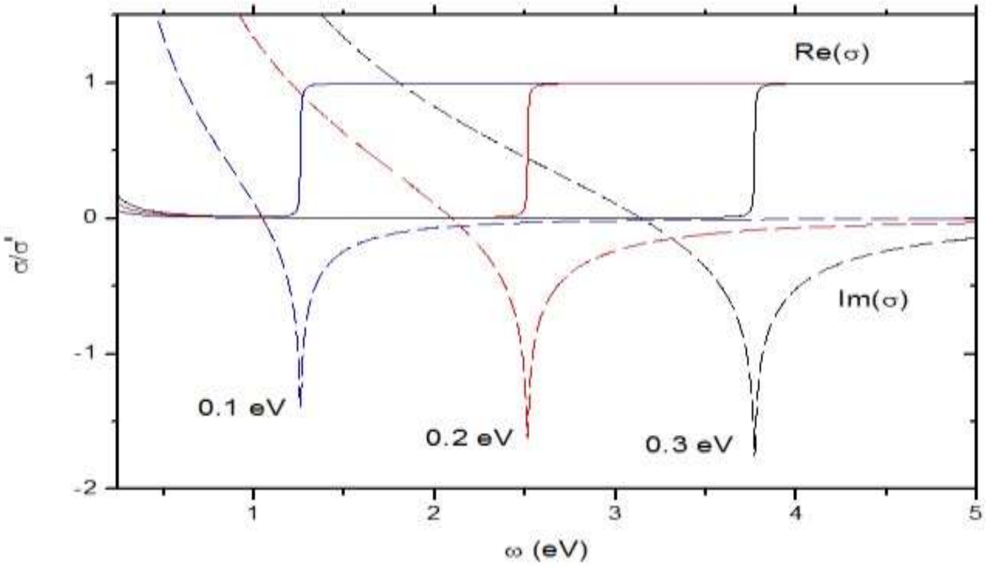

Figure 1. The dynamical conductivity of graphene, in units of $\sigma' = e^2/4\hbar$, for different doping levels. The relaxation time is $\tau = 1\,ps$. TM surface modes exist in the region where $Im(\sigma) > 0$, while TE surfaces modes exist in the region where $Im(\sigma) < 0$.

Recently it has reported the excitation of SPs for a monolayer graphene sandwiched between two dielectric media for TM polarization via the ATR technique [2]; experimentally TM SPs have been detected in the terahertz regime [3], [4], [5]. On the other hand, TE SPs in graphene have been only predicted theoretically [6], so far [7]. In this work, we describe theoretically the excitation of SPs for TM polarization via ATR using an Otto configuration. It is important to mention that ATR graphene-based systems can be used as efficient components for enhancing optical absorption at specific wavelengths, hence the importance of its study. It is found that once the SP is excited it remains within a short range of variations of the air gap d, where d is the distance between prism and graphene.

Additionally, in this work we analize the reflection and transmission spectra of a multilayer graphene-dielectric system only for TM polarization. It is found that when the number of graphene layers is large, for example ten layers, band structure is observed in these spectra because the gaps are seen clearly. Besides, it is observed that these gaps depend on the dielectric thickness.

It is important to mention that all the calculations and results are obtained from the slab graphene approximation, i.e., it is taken that each graphene sheet has effective thickness, $t_g \sim 0.5\,nm$ and an equivalent dielectric constant given by the following equation

$$\varepsilon_g = 1 + \frac{i\sigma}{\omega\varepsilon_0 t_g} \quad .$$

S

o that the boundary conditions are given by the simple form

$$E_{j+1} - E_j = 0$$

$$H_{j+1} - H_j = 0 \quad .$$

References:

[1] C. H. Gan, H. S. Chu, and E. P. Li, Phys. Rev. B **85, 125431 (2012).**

[2] F. Ramos-Mendieta, J. A. Hernandez-Lopez, and M. Palomino Ovando, AIP Advances **4, 067125 (2014).**

[3] L. Ju, B. Geng, J. Horng, C. Girit, M. Martin, Z. Hao, H. A. Bechtel, X. Liang, A. Zettl, Y. R. Shen, and F. Wang, Nat. Nanotechnol **6, 630 (2011).**

[4] Z. Fei, A. S. Rodin, G. O. Andreev,W. Bao, A. S. McLeod, M.Wagner, L. M. Zhang, Z. Zhao,M. Thiemens, G. Dominguez, M. M. Fogler, A. H. Castro-Nieto, C. N. Lau, F. Keilmann, and D. N. Basov, Nature **487, 82 (2012).**

[5] X. Zhu, W. Yan, P. U. Jepsen, O. Hansen, N. A. Mortensen, and S. Xiao, Appl. Phys. Lett. **102, 131101 (2013).**

[6] S. A. Mikhailov and K. Ziegler, Phys. Rev. Lett. **99, 016803 (2007).**

[7] F. Ramos-Mendieta **(work in process).**

[8] Choon How Gan, Appl. Phys. Lett. **101, 111609 (2012).**

Presenting author's email: alejandro.hernandez058@gmail.com

Influence of metal conductivity on the chirality of metamaterials with twisted U-shaped resonators

Anatolii Konovalenko[1]*, Jorge A. Reyes-Avendaño[2], and Felipe Pérez-Rodríguez[1]

[1] *Instituto de Física, Benemérita Universidad Autónoma de Puebla, Apdo. Post. J-48, Puebla, Pue. 72570, Mexico*
[2] *Escuela de Ingeniería y Tecnologías de Información, Tecnológico de Monterrey, Campus Puebla, Puebla, Pue. 72800, Mexico*
*E-mail: anatolii@ifuap.buap.mx

Abstract

A high interest in the area of metamaterials is given to the *negative index metamaterials* (NIM), usually meaning that their dielectric permittivity and magnetic permeability are both negative. However, it is possible to fabricate NIM using chiral structures which, by definition, differ from their mirror image. In metamaterials, the chirality comes from their structure and, therefore, emerges even if the components (e.g. metal and dielectric) do not possess such a property. As a consequence, electromagnetic waves with left-handed and right-handed polarizations, propagating in chiral metamaterials, have different complex refraction index.

To describe the optical properties of metamaterials, it is convenient to use the effective bianisotropic response having four tensors: permittivity, permeability, and two crossed magneto-electric ones. The latter tensors are connected with the effective chiral response of the artificial metal-dielectric structures. There exist various homogenization approaches to calculate the elements of the bianisotropic-response tensors. The homogenization theory developed in [1,2] is based on the Fourier formalism and provides explicit expressions for all the components of the effective metamaterial response for homogenized photonic crystals of any type of Bravais lattice and arbitrary form of the inclusions.

Recently [3], a chiral metamaterial structure consisting of 4 planes per one elementary cell was proposed. Each plane has a periodic array of U-shaped metal resonators, oriented in the same direction inside the plane. Every further resonator plane is rotated clockwise 90° with respect to the

previous plane (see Fig.1). Applying the homogenization approach [1,2] and using a real metal conductivity, the elements of the effective bianisotropic tensors for structures with twisted U-shaped resonators were calculated in Ref. [3]. The metamaterial exhibits a strong chiral response.

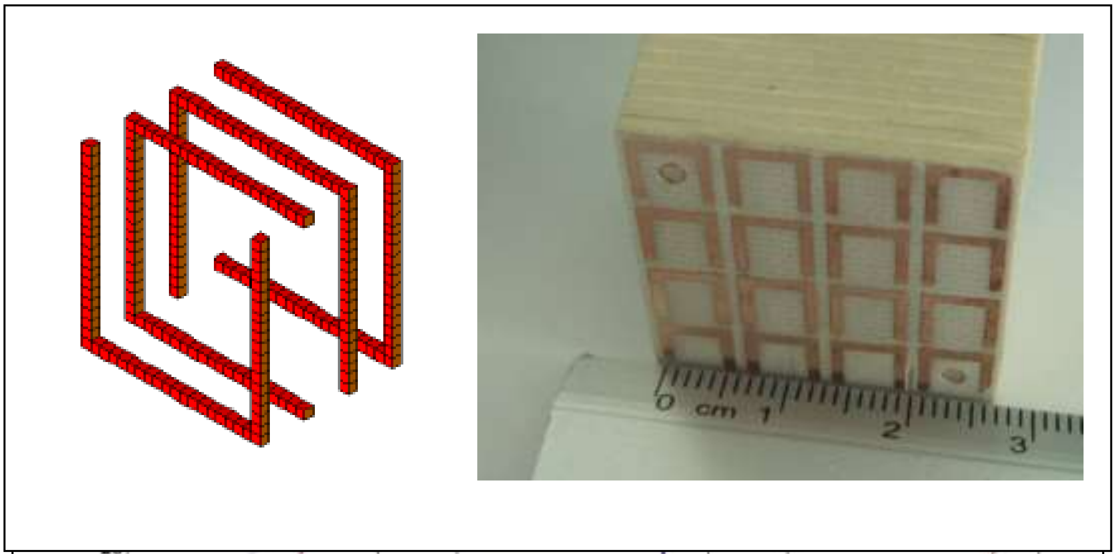

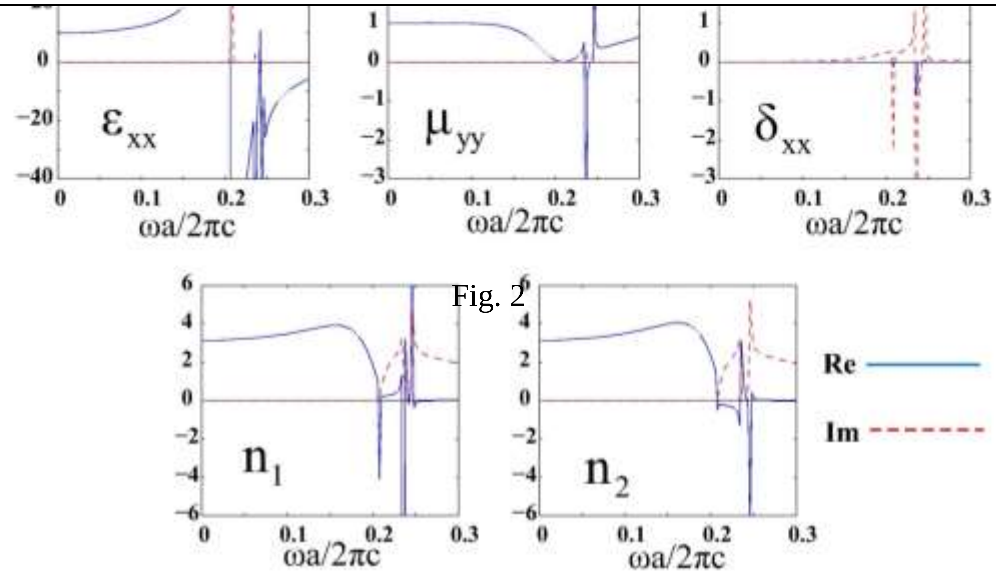

Fig. 2

Also in Ref. [3], it was shown that four circularly-polarized eigenmodes can propagate along the metamaterial growth direction. Two of them, decaying along the positive direction of the z-axis which is assumed to be perpendicular to the planes of U-shaped resonators, are identified by the sign of the imaginary part of the wave numbers. The identification is ambiguous within certain frequencies intervals where the imaginary parts of the wave numbers are equal to zero. In principle, this kind of ambiguity may be avoided if the losses are increased.

In contrast to the work [3], we use the Drude model for the metal conductivity. Moreover, we analyze the frequency dependences of the diagonal elements of the permittivity, permeability, and magnetoelectric tensors for metamaterials composed of Cu (Fig. 2) and Al. The use of a realistic complex conductivity allowed us to eliminate the ambiguity in choosing the circularly-polarized electromagnetic eigenmodes, decaying along the positive direction of the z-axis. Consequently, the frequency intervals, where their refractive indexes (n_1 and n_2 in Fig. 2) are negative and the losses are relatively small, are well identified. We have also studied the effect of the metal conductivity on the position of the frequency bands where the metamaterial exhibits strong chirality.

This work was partially supported by PRODEP-BUAP-CA-250 and SEP-CONACYT (grant No. CB-2011-01-166382).

References

1. J.A. Reyes-Avendao, U. Algredo-Badillo, P. Halevi, F. Pérez-Rodríguez, “From photonic crystals to metamaterials: the bianisotropic response”, New J. Phys. **13**, 073041, 1–33 (2011).
2. J. A. Reyes-Avendaño, M. P. Sampedro, E. Juárez-Ruiz, F. Pérez-Rodríguez, “Bianisotropic metamaterials based on twisted asymmetric crosses”, J. Opt. **16**, 065102, 1–14 (2014).
3. F. Pérez-Rodríguez, A. Konovalenko, and J. A. Reyes-Avendaño, "Chiral metamaterials based on twisted U-shaped inclusions," in Latin America Optics and Photonics Conference, OSA Technical Digest (online) (Optical Society of America, 2014), paper LM4A.33.

Transport of mechanical vibrations in 2D elastic chaotic cavities

Enrique Flores-Olmedo[a], G. Báez[a], M. Martínez-Mares[b], and R. A. Méndez-Sánchez[c]

[a]Departamento de Ciencias Básicas, Universidad Autónoma Metropolitana-Azcapotzalco, Av San Pablo 180, Col. Reynosa Tamaulipas, 02200 México DF, México.
[b]Departamento de Física, Universidad Autónoma Metropolitana-Iztapalapa, A.P. 55-534, 09340 México D.F., Mexico
[c]Instituto de Ciencias Físicas, Universidad Nacional Autónoma de México, A.P. 48-3, 62251 Cuernavaca, Morelos, México.
[a]Departamento

Wave scattering of systems with chaotic ray dynamics has motivated intense research activity in recent years. Among others we should mention quantum dots[1], microwave cavities [2], and elastic systems [3]. In all these systems the transport properties, as the reflection and transmission coefficients, fluctuate with tunable parameters as the energy, the frequency, the shape, or the intensity of an external magnetic field. The elastic systems, which we study, offer a not very expensive alternative to study these kind of systems.

In this work we give preliminary results of the fluctuation properties of the transmission of elastic waves through a chaotic cavity. The scattering systems consists of a plate with the shape of the Sinai billiard with two connected leads (See Fig. 1). To measure the transmission spectrum, acoustic resonance spectroscopy was used [4]. As can be seen in Fig. 1, this technique is used with a vector network analyzer, a high-fidelty audio amplifier and two electromagnetic-acoustic transducers (EMATs) [5]. The transmission is measured locating the driver in one lead and the detector in the other lead.

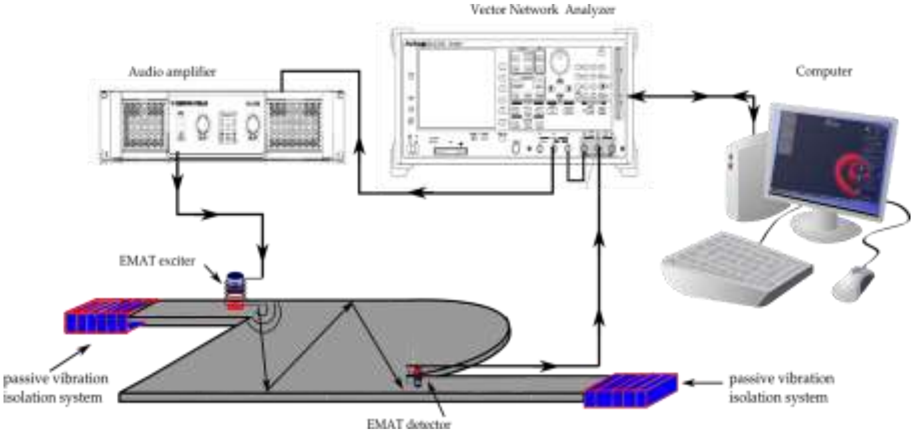

Fig. 1. Setup used to measure the transmission spectrum of an elastic 2D cavity (plate). In order to absorb the waves at the ends of the leads, a passive vibration isolation system was used.

The frequency was varied from 1.0 Hz up to 9.4 kHz, exciting and detecting out-of-plane vibrations in two points: in the center and in one side of the lead. Since the leads have free-boundary conditions, the opening of the first channel is at 0 Hz. The opening of the third channel was found around 3.4 kHz. From the measured results the distribution of the transmission was obtained and compared with the random matrix theory predictions [6]. The distributions have a reasonable agreement with the theory and also show the presence of direct processes coming from a prompt response [7].

References

[1] C. M. Marcus, A.J. Rimberg, R.M. Westervelt, P. F. Hopkins y A. C. Gossard, Conductance fluctuations and chaotic scattering in ballistic microstructures, Phys. Rev. Lett. **69**, 506 (1992).

[2] E. Doron, U. Smilansky, and A. Frenkel, Phys. Rev. Lett. **65**, 3072 (1990).

[3] G. Báez, M. Cobián-Suárez, A.M. Martínez-Argüello, M. Martínez-Mares, and R.A. Méndez-Sánchez, “Scattering of Elastic Waves in a Quasi-One-Dimensional Cavity: Theory and Experiment”, Acta Physica Polonica A **124**, 1069-1073 (2013).

[4] J.A. Franco-Villafañe, E. Flores-Olmedo, G. Baéz, O. Gandarilla-Carrillo y R.A. Méndez-Sánchez, Acoustic resonance spectroscopy for the advanced undergraduate laboratory, Eur. J. Phys. **33**, 1761 (2012).

[5] A. Morales, L. Gutiérrez, J. Flores, Improved eddy current driver-detector for elastic vibrations, American Journal of Physics 69 (2001) 517--522.

[6] P.A. Mello, N. Kumar, Quantum Transport in Mesoscopic Systems: Complexity and Statistical Fluctuations, Oxford University Press, New York 2005.

[7] U. Kuhl, M. Martínez-Mares, R. A. Méndez-Sánchez, and H.-J. Stöckmann, Phys. Rev. Lett. **94**, 144101 (2005).

Reducción de los efectos de absorción en la propagación de la radiación electromagnética en cristales fotónicos unidimensionales construidos con materiales izquierdos y derechos.

H. Kinto Ramírez
Facultad de Ciencias Físico-Matemáticas
Benemérita Universidad Autónoma de Puebla

En este trabajo se estudian las propiedades ópticas (estructuras de bandas, coeficientes de transmisión y reflexión, etc.) de cristales fotónicos unidimensionales construidos a partir de alternar materiales con índice de refracción negativa (materiales izquierdos) y dieléctricos (aire). El método usado en los cálculos es el método de la matriz de transferencia, el cual permite conectar los campos eléctricos y magnéticos a través de la estructura. Aun cuando se consideran efectos de absorción y dispersión para la permitividad dieléctrica y la permeabilidad magnética, se demuestra la presencia de modos oscilatorios y de tunelamiento. Se presentan resultados donde se observa que las ondas electromagnéticas se propagan mejor en los modos de tunelamiento que en los modos oscilatorios, sin embargo, el tiempo de propagación es mayor en los modos de tunelamiento que en los oscilatorios.

Detección de modos guiados en guías de onda acústica

Ham-Rodríguez C. I.[1], *Moctezuma-Enríquez D.*[2], *Manzanares-Martínez J.*[3], *Manzanares-Martínez B.*[4]

[1]Posgrado en Ciencias (Física) de la Universidad de Sonora, [2]Centro de Investigación en Materiales Avanzados, [3]Departamento de Investigación en Física de la Universidad de Sonora, [4]Departamento de Física de la Universidad de Sonora.

Se presenta un ejercicio teórico-experimental para estudiantes de licenciatura y de posgrado en Física. El trabajo se concentra en la dispersión de onda en guías acústicas. Se calcula la relación de dispersión de la guía de ondas acústicas conformada por dos medios semiinfinitos de material sólido que rodean una capa de grosor *d* de un fluido ideal, que en este caso es agua tal como se muestra en la Figura 1. Se estudia el efecto de la relación de los modos de propagación de sistema en la transmisión de señales ultrasónicas, utilizando la herramienta matemática de la Trasformada de Fourier de Tiempo Corto (STFT Short Time Fourier Transform).

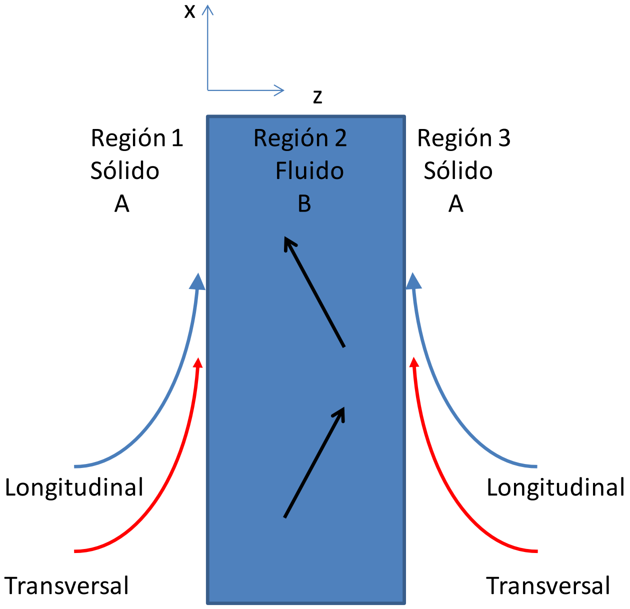

Figura 1. Sistema de estudio consistente en una capa de fluido ideal de grosor *d* en contacto con dos medios semiinfinitos de material sólido a través de interfaces planas paralelas al plano *x*-*y*.

El material A está caracterizado por la densidad ρ_a, con velocidades de sonido longitudinal y transversal c_{la} y c_{ta}, respectivamente. El medio fluido B está caracterizado por densidad ρ_b

y velocidad de sonido c_b. En los materiales sólidos es posible la existencia de dos tipos de onda, las transversales cuya amplitud de oscilación es perpendicular a la dirección de propagación y las longitudinales donde la oscilación es paralela a la propagación. Por otra parte, en un fluido ideal solo las oscilaciones de tipo longitudinal pueden propagarse.
Para que pueda darse la propagación a través medio fluido es necesario que la onda elástica decaiga en el material sólido, tal como se muestra en la Figura 1. Bajo esta perspectiva la forma de la solución de la ecuación de onda para cada región del sistema está dada por:

$$
\begin{aligned}
u_{1x} &= A_1^{l-}\frac{k_x c_{la}}{\omega}\exp\left(\alpha z + ik_x x\right) + A_1^{t-}\frac{i\beta c_{ta}}{\omega}\exp\left(\beta z + ik_x x\right),\\
u_{1z} &= -A_1^{l-}\frac{i\alpha c_{la}}{\omega}\exp\left(\alpha z + ik_x x\right) + A_1^{t-}\frac{k_x c_{ta}}{\omega}\exp\left(\beta z + ik_x x\right),\\
u_{2x} &= A_2^{+}\frac{k_x c_b}{\omega}\exp\left[i\left(k_x x + k_2 z\right)\right] + A_2^{-}\frac{k_x c_b}{\omega}\exp\left[i\left(k_x x - k_2 z\right)\right],\\
u_{2z} &= A_2^{+}\frac{k_2 c_b}{\omega}\exp\left[i\left(k_x x + k_2 z\right)\right] - A_2^{-}\frac{k_2 c_b}{\omega}\exp\left[i\left(k_x x - k_2 z\right)\right],\\
u_{3x} &= A_3^{l+}\frac{k_x c_{la}}{\omega}\exp\left(-\alpha z + ik_x x\right) + A_3^{t+}\frac{i\beta c_{ta}}{\omega}\exp\left(-\beta z + ik_x x\right),\\
u_{3z} &= A_3^{l+}\frac{i\alpha c_{la}}{\omega}\exp\left(-\alpha z + ik_x x\right) - A_3^{t+}\frac{k_x c_{ta}}{\omega}\exp\left(-\beta z + ik_x x\right).
\end{aligned}
$$

Donde $A_n^{\mu\pm}$ denota la amplitud de onda en la región $n = 1,2,3$, de tipo $\mu = l$ para la onda longitudinal o $\mu = t$, que se propaga hacia la dirección $+z$ o $-z$. Para la región 2 se omite μ dado que ahí la onda es necesariamente longitudinal. k_x es el vector de onda paralelo al eje x, k_2 es el vector de onda paralelo al eje z en la Región 2, mientras que:

$$
\alpha = \sqrt{k_x^2 - \frac{\omega^2}{c_{la}^2}},
$$

$$
\beta = \sqrt{k_x^2 - \frac{\omega^2}{c_{ta}^2}},
$$

se definen de esta forma con la finalidad de asegurar el decaimiento de las ondas longitudinales y transversales en las regiones 1 y 3 del sistema.

Después de aplicar las condiciones de frontera consistentes en:

1) Continuidad del desplazamiento normal a las interfaces en $z=0$:

$$u_{1z}\big|_{z=0} = u_{2z}\big|_{z=0}$$

2) Continuidad del desplazamiento normal a las interfaces en $z=d$:

$$u_{2z}\big|_{z=d} = u_{3z}\big|_{z=d}$$

3) Continuidad del esfuerzo normal a las interfaces en $z=0$:

$$\sigma_{zz}^{1}\big|_{z=0} = \sigma_{zz}^{2}\big|_{z=0}$$

4) Continuidad del esfuerzo normal a las interfaces en $z=d$:

$$\sigma_{zz}^{2}\big|_{z=d} = \sigma_{zz}^{3}\big|_{z=d}$$

5) Anulación del esfuerzo tangencial en $z=0$ [ver ecuación (31)]:

$$\sigma_{xz}^{1}\big|_{z=0} = 0$$

6) Anulación del esfuerzo tangencial en $z=d$ [ver ecuación (31)]:

$$\sigma_{xz}^{3}\big|_{z=d} = 0$$

Donde se aplica la definición de tensor de esfuerzos para el caso isotrópico:

$$\sigma_{ik} = 2\rho c_t^2 u_{ik} + (\rho c_l^2 - 2\rho c_t^2) u_{ll} \delta_{ik}$$

Donde el tensor de deformación u_{ik} es:

$$u_{ik} = \frac{1}{2}\left(\frac{\partial u_i}{\partial x_k} + \frac{\partial u_k}{\partial x_i}\right).$$

Después de aplicar las condiciones de frontera obtenemos un sistema de 6 ecuaciones con 6 incógnitas que resolvemos numéricamente.

En la Figura 2 mostramos la relación de dispersión que se obtiene para una guía de agua rodeada de aluminio, con los siguientes parámetros:

$$\rho_a = 2.7433 gr/cm^3,$$
$$c_{la} = 6.411 \times 10^5 cm/s,$$
$$c_{ta} = 3.132 \times 10^5 cm/s,$$
$$\rho_b = 0.9934 gr/cm^3,$$
$$c_b = 1.504 \times 10^5 cm/s.$$

Como puede observarse en la Fig. 2 los modos guiados se ubican por debajo de las líneas de sonido del aluminio del aluminio y por encima de la línea del agua, correspondiendo a ondas que viajan en el fluido y decaen en el sólido. En el panel (a), de izquierda a derecha las líneas azules corresponden a las líneas de sonido para la onda longitudinal del aluminio, la transversal en aluminio y el sonido en el agua. La velocidad de grupo es mostrada en el panel (b). El panel (c) muestra los tiempos de arribo calculados para una distancia de 50cm, es decir $t = 50cm / v_g$.

Los resultados obtenidos son consistentes con otros mostrados en la literatura (1), solo que en ese caso se estudiaron soluciones de distinta geometría a la onda plana. Para estudiar los efectos de la relación de dispersión de los modos guiados en la transmisión de ondas en una guía se realizó el montaje experimental mostrado en la Figura 3. Se utilizó un transductor de inmersión de 1MHz para emitir pulsos ultrasónicos que viajaron a lo largo de la guía de ondas acústicas. La guía tiene una longitud de 50cm, manejando distancias *d* en el orden de milímetros. La onda recibida por el transductor receptor, también de 1MHz de inmersión es enviadas a un osciloscopio para su digitalización y posterior procesamiento. También se realizaron mediciones con trasductores de 500kHz.

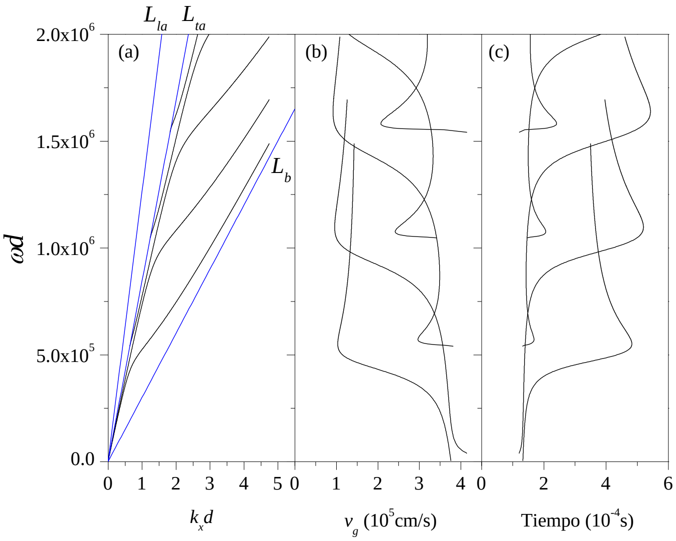

Figura 2. (a) Relación de dispersión de una guía de agua rodeada de aluminio. (b) Velocidad de grupo de los modos de oscilación. (c) Tiempos de arribo calculados para una distancia de 50cm.

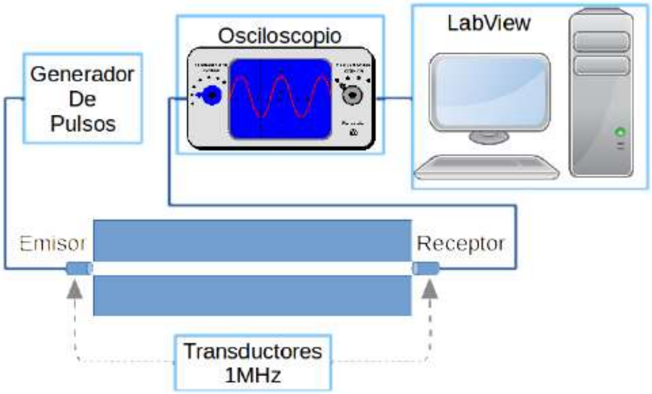

Figura 3. Montaje experimental para el análisis de la transmisión de ondas ultrasónicas en una guía.

En la Figura 4 mostramos la señal obtenida en el espacio del tiempo en el receptor tal como se obtiene al realizar el experimento, en este caso se trata de una medición para una $d \approx 4mm$.

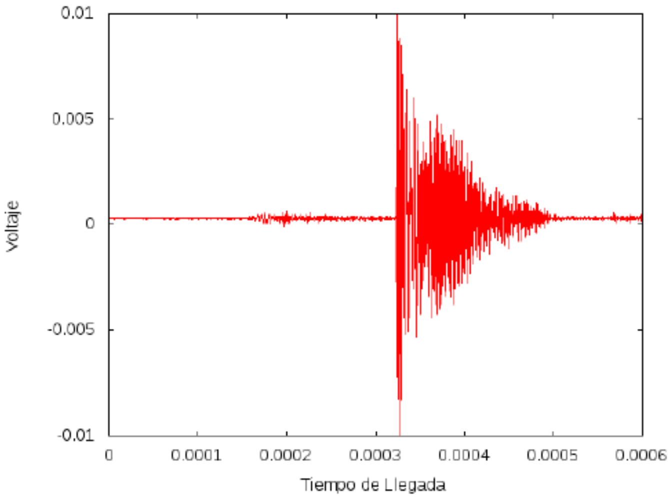

Figura 4. Señal obtenida por el transductor receptor para una medición con una guía de $d \approx 4mm$.

Aplicamos un procesamiento de Transformada de Fourier de Tiempo Corto a las señales obtenidas por el transductor receptor, similares a la que se puede observar en la Fig. 4.

En la Figura 5 mostramos la STFT para una separación $d \cong 3.2mm$ medida con un transductor de 500kHz. Puede observarse que el resultado del procesamiento de datos es un tipo de “huella dactilar” de la señal obtenida, las zonas más claras corresponden a zonas donde se obtiene una mayor intensidad de señal para un tiempo de arribo al transductor para cada frecuencia.

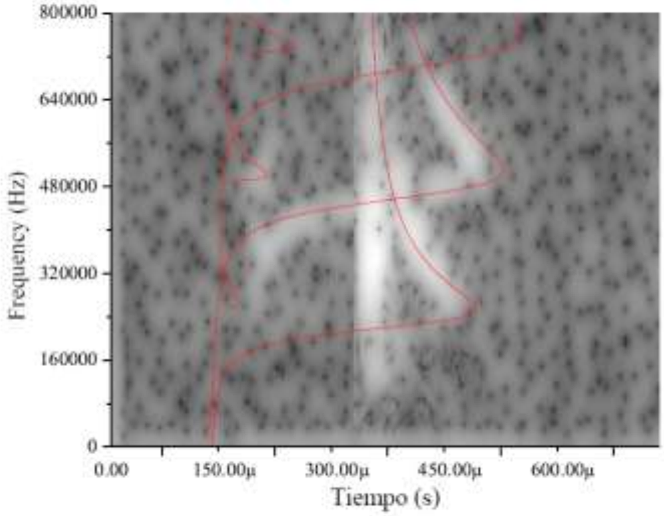

Figura 5, Transformada de Fourier de Tiempo Corto de una señal obtenida con transductores de 500kHz en una guía de $d \cong 3.2mm$. La línea corresponde al cálculo de los tiempos de vuelo obtenidos de forma numérica.

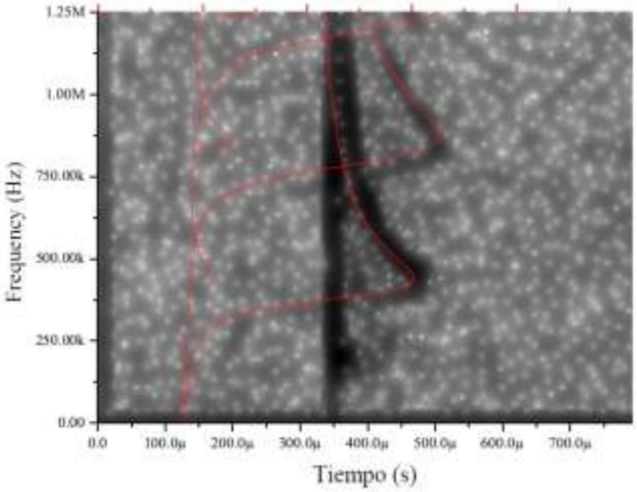

Figura 6. Transformada de Fourier de Tiempo Corto de una señal obtenida con transductores de 1MHz en una guía de $d \cong 2mm$. La línea corresponde al cálculo de los tiempos de vuelo obtenidos de forma numérica.

Vemos que es posible interpretar la transmisión de ondas del sistema experimental en término del análisis de la relación de dispersión de la guía de onda acústica.

Estos resultados pueden ser utilizados tanto como experimento didáctico como una herramienta de análisis de investigación (2).

Bibliografía

1. *Elastic wave guided by a fluid layer, a new type of ultrasonic propagation.* **Wang, C. et al.** 1970, Applied Physics Letters, Vol. 16, pág. 291.

2. *Relationships between Existence of Negative Group Velocity and Physical Parameters of Materials for Lamb-Type Waves in Solid/Liquid/Solid Structure.* **al, Kojiro Nishimiya et.** 2008, Jpn. J. Appl. Phys., Vol. 47, pág. 3855.

Surface modes coupling in one-dimensional metamaterial photonic crystals with defects

J. E. Pérez-Rodríguez[1], M. A. Palomino-Ovando[1], Gregorio H. Cocoletzi[2]

[1]Benemerita Universidad Autónoma de Puebla, Facultad de Ciencias Físico-Matemáticas, Puebla, México
[2]Benemerita Universidad Autónoma de Puebla, Instituto de Física, Apartado Postal J-48, Puebla 72570, México
jepr_777@yahoo.com.mx,marthap@fcfm.buap.mx,cocoletz@ifuap.buap.mx

Abstract

We study surface plasmon propagation at one-dimensional (1D) metamaterial-dielectric photonic crystals (PC) applying the attenuated total reflectivity (ATR) technique. In addition we consider the presence of defects in inner layers to explore the coupling of the surface plasmons with modes associated to the defect.

The condition for plasmon propagation at the interface between two nonmagnetic media is that one medium should exhibit a positive while the other a negative dielectric constant as in the interface dielectric-metal. In addition materials with both negative dielectric permeability and magnetic permeability (metamaterials) [1] may also support surface or interface plasmon modes. Therefore the dielectric-metamaterial interface is suitable for plasmon propagation. Metamaterials or left hand materials [LHM] are not available in nature however they may be fabricated to yield artificial structures with both negative dielectric permeability and magnetic permeability values in some particular frequency regime, as suggested by Veselago [2] and recently realized experimentally by Pendry [3]. The dispersive characteristics together with the magnetic contributions by LHM may induce novel phenomena such as the presence of plasmon polaritons which could help to increase the microscopies resolutions, the LEDs efficiency, the chemical and biological device sensitivities [4 -6].

A one-dimensional (1D) superlattice (photonic crystal) made up of alternating layers of a dielectric and a metamterial may support modes at the interfaces. The condition of interface modes existence is that the dielectric material should exhibit a positive dielectric constant and the metamaterial should have both negative dielectric permeability and magnetic permittivity [7,8]. These structures display novel properties such as zero energy gaps [9,10] which are not manifested in metal-dielectric superlattices. Recent studies have demonstrated that in the frequency gap the light-plasmon coupling is weak reducing the plasmon polariton modes to plasmons of dielectric or magnetic characteristics [8].

For our study we consider the interface composed by a material with positive refraction index *n* and a multilayer system formed by alternating a layer of positive refraction index and a layer with negative refraction index (metamaterial). In the metamaterial both the dielectric permittivity ε_2 and magnetic permeability μ_2 are dispersive and absorptive with negative real parts. P (TM) or S (TE) polarized light interacts with the layer structure in the attenuated total reflectivity geometry. ε_2 and μ_2 are described by a Drude [9] type model as shown in the following equations (1) and (2)

$$\varepsilon_2 = 1.21 - \frac{\omega_p^2}{\omega(\omega + i\gamma)} \tag{1}$$

$$\mu_2 = 1 - \frac{\omega_p^2}{\omega(\omega + i\gamma)} \tag{2}$$

where $\omega_p = 10c/\Lambda$ with $\Lambda = d_v + d_{LHM}$, d_v and d_{LHM} are the thicknesses of the right hand and left hand layers, respectively, and γ is the damping factor. In this work the right hand material is taken as vacuum with $\varepsilon_1 = \mu_1 = 1$. In this work we used the method of the transfer matrix to calculate the band structure, the internal fields and reflection spectra. And we present surface mode in a one-dimensional (1D) photonic crystals for both S and P polarized waves, we discuss the amplification of the electric field in the defect leyer, and investigate the coupling of the incident light with the surface modes using the attenuated total reflectivity geometry in both Otto and Kretchmann arrangements. To account for the impurity we consider a vacuum gap of different widths. The field amplitude enhancement has been described noting that the smaller defect layer thickness the stronger interactions appear between the adjacent multilayer structures, in contrast as the defect layer thickness increases the layer fields interaction is prevented and the filed is more localized at the defect site.

Referencias

[1] Stefan Alexander Maier," Plasmonics Fundamentals and aplications" , Springer, (2007).

[2] Veselago, V. G., "The electrodynamics of substances with simultaneously negative values of ε and μ," Sov. Phys. Usp., Vol. 10, 509–514, 1968.

[3] Pendry, J. B., "Negative Refraction Makes a Perfect Lens" Phys. Rev. Lett., Vol. 85, No. 18, 3966, (2000).

[4] Ozbay E., " Plasmonics: Merging Photonics and Electronics at Nanoscale Dimensions", Science, Vol. 311, 189, 2006.

[5] Dolling G. Enkrich C. Wegener M. Soukoulis C. M. and Linden S.," Low-loss negative-index metamaterial at telecommunication wavelengths", Opt Lett., Vol. 31, 1800, 2006.

[6] Reyes-Gómez, E., D. Mogilevtsev, S. B. Cavalcanti, C. A. de Carvalho and L. E. Oliveira, "Plasmon polaritons in photonic superlattices containing a left-handed material," EPL Journal, Vol. 88, 24002, 2009.

[7] Villa-Villa, F., J. A. Gaspar-Armenta and A. Mendoza-Suárez, "Surface Modes in one dimensional photonic crystal that included left handed materials," J. of Electromagn. Waves and Appl., Vol. 21, 485-499, 2007.

[8] Mogilevtsev, D., E. Reyes-Gómez, S. B. Cavalcanti, C. A. A. de Carvalho and L. E. Oliveira "Plasmon polaritons in photonic metamaterial superlattices: Absorption effects" Phys. Rev. E, Vol. 81, 047601, 2010.

[9] Haitao Jiang, Hong Chen, Hongqiang Li, Yewen Zhang and Shiyao Zhu, "Omnidirectional gap and defect mode of one-dimensional photonic crystals containing negative-index materials," Appl. Phys. Lett. vol. 83 , 5386, 2003.

[10] Li J. Zhou L., Chan C. T. and Sheng P., " Photonic transmission spectra in one-dimensional fibonacci multilayer structures containing single-negative metamaterials", Phys. Rev, Lett., 90, 083901, (2003).

In-plane vibrations in a two-dimensional periodic elastic system: experimental realization

Filiberto Ramírez-Ramírez[a], G. Báez[a], J. A. Franco-Villafañe[b],
and Rafael A. Méndez-Sánchez[b]

[a]Departamento de Ciencias Básicas, Universidad Autónoma Metropolitana-Azcapotzalco, Av San Pablo 180, Col. Reynosa Tamaulipas, 02200 México DF, México.
[b]Instituto de Ciencias Físicas, Universidad Nacional Autónoma de México, A.P. 48-3, 62251 Cuernavaca, Morelos, México.

The in-plane vibrations are an important problem in engineering since they appear at high frequencies in several areas of mechanical vibrations [1]. In particular, in the design of ship hulls, it has been shown that the in-plane vibrations are strongly related to the noise [2]. Also, in-plane vibrations appear when following narrow data tracks in data-storage systems [3]. To control these vibrations passive structured systems have to be studied.

In this work we study experimentally the in-plane vibrations of locally periodic narrow plate. 27 cells are machined on the plate by grooving on it a rectangular grid, to obtain a band structure (see Fig. 1). The machined channels have width *a* and depth *h.* The mechanical structure obtained in this way resembles the shape of a "*chocolate bar*".

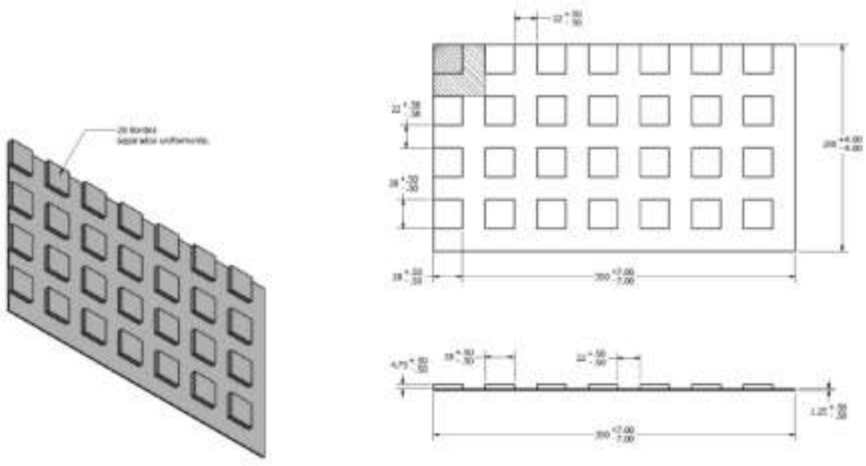

Figure 1. Example of a narrow plate with 28 cells. It was constructed by machining channels in both directions. In the right part, upper and lateral views are given. The dashed region in the upper view corresponds to the unit cell.

The plate was first studied theoretically using a plane wave expansion [4,5]. The method was applied to the classical theory of in-plane vibrations. The unit cell is repeated periodically in both directions and a band structure for in-plane vibrations is obtained. For certain values of *a* and *h*, a full gap is found.

Following the methods of Ref. [1], The spectrum of the in-plane resonances was measured using acoustic resonant spectroscopy [6]. The experimental setup includes the electromagnetic-acoustic transducers or EMATs, that are highly selective to the different kind of mechanical waves. In agreement with the theory, a full gap is found.

References

[1] In-plane vibrations of a rectangular plate: plane wave expansion modelling and experiment
A. Arreola-Lucas , J. A. Franco-Villafañe, G. Báez, and R. A. Méndez-Sánchez, Journal of Sound and Vibration (*in press*).

[2] D.J. Gorman, Free in-plane vibration analysis of rectangular plates by the method of superposition, Journal of Sound and Vibration 272 (2004) 831--851.

[3] K. Hyde, J.Y. Chang, C. Bacca, J.A. Wickert, Parameter studies for plane stress in-plane vibration of rectangular plates, Journal of Sound and Vibration 247 (2001) 471--487.

[4] B. Manzanares-Martínez, J. Flores, L. Gutiérrez, R.A. Méndez-Sánchez, G. Monsivais, A. Morales, F. Ramos-Mendieta, Flexural vibrations of a rectangular plate for the lower normal modes, Journal of Sound and Vibration 329 (2010) 5105--5115.

[5] B. Manzanares-Martínez, F. Ramos-Mendieta, A. Baltazar, Ultrasonic elastic modes in solid bars: An application of the plane wave expansion method, Journal of the Acoustical Society of America 127 (2010) 3503—3510.

[6] J.A. Franco-Villafañe, E. Flores-Olmedo, G. Báez, O. Gandarilla-Carrillo and R.A. Méndez-Sánchez, Acoustic resonance spectroscopy for the advanced undergraduate laboratory, European Journal of Physics 33 (2012) 1761--1769.

Asymmetric propagation between subwavelength planar waveguides

C. I. Ham-Rodriguez and J. Manzanares-Martinez
Departamento de Investigacion en Fisica, Universidad de Sonora,
Apartado Postal 5-088, Hermosillo, Sonora 83000, Mexico

Y. J. Rodriguez-Viveros, B. Manzanares-Martinez, and P. Castro-Garay
Departamento de Fisica, Universidad de Sonora,
Blvd. Luis Encinas y Rosales, Hermosillo, Sonora 83000, Mexico

D. Moctezuma-Enriquez
Centro de Investigacion en Materiales Avanzados (CIMAV),
Miguel de Cervantes 120, Chihuahua 31109, Mexico

We study the asymmetric propagation through the junction of two subwavelength planar waveguides with high and low refractive indices, respectively. The light propagation is analyzed at a certain frequency where for the low index waveguide only exist the $TE0$ eigenmode while for the high index waveguide are allowed the $TE0$ and $TE1$ eigenmodes. Using a time dependent modeling for the electromagnetics waves propagation is found an asymmetric transmission through the junction. Notwithstanding is observed that the $TE0$ mode is able to propagates from the low to the high index waveguide and vice versa, it has been found that the $TE1$ mode can not pass from the high to the low index waveguide.

Theoretical and experimental study of electromagnetic forces induced in one-dimensional photonic crystals.

Noemí Sánchez[1], J. E. Lugo[2], M. A. Palomino[1]

[1] Benemérita Universidad Autónoma de Puebla, Av. San Claudio y Río Verde, Col. San Manuel, Puebla, México, 72570 [2]Visual Psychophysics and Perception Laboratory, School of Optometry, University of Montreal, C.P. 6128 succ. Centre Ville, Montreal, Quebec, Canada H3C3J7.

In this work we studied theoretically and experimentally the induction of electromagnetic forces in one-dimensional photonic crystal when the beam impinges normally in the photonic crystal. The photonic structure consists of a micro-cavity like structure formed of two one-dimensional photonic crystals made of free-standing porous silicon (showed in Figure 1), separated by a variable air gap and the working wavelength is 633 nm.

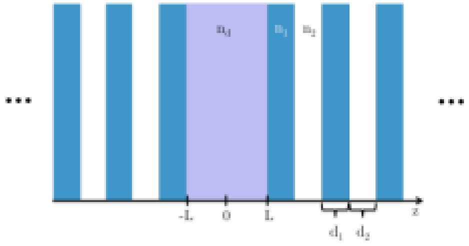

Figure 1. Onedimensional photonic crystal used in this work.

By applying the transfer matrix theory, we obtain the transmitances as a function of the frequency. For the evaluation of the electromagnetic fields within the structure we used as reference Sopaheluwakan's work. We started writing the solution as a superposition of a right and left going monocrhomatic wave. Then we used the relation for the plane wave amplitud and inally using the periodicity property of the onedimensional photonic crystal we can obtain the electromagnetics field equation:

$$E_z(L) = ik_d(A_1 - B_1) = ik_d(1+\gamma)A_1 \tag{1}$$

$$E_z(L) = ik_d\frac{(1+\gamma)}{(1-\gamma)}E_L \tag{2}$$

Within the dielectric layers, the Lorentz force density is given by: $\vec{f} = \rho\vec{\mathcal{E}} + \vec{\mathcal{J}} \times \vec{B}$

Since in a dielectric material $\varepsilon_0\varepsilon_r\vec{\mathcal{E}}=\varepsilon_0\vec{\mathcal{E}}+\vec{\mathcal{P}}$ and $\nabla\cdot\vec{\mathcal{E}}=0$ as there is no free charge, it follows that $\rho=0$. Therefore only the second term in Eq. 3 is nonzero, and the volume force density, using $\vec{\mathcal{B}}=\mu_0\vec{\mathcal{H}}$, reads

$$\vec{f}=\varepsilon_0(\varepsilon_r-1)\frac{\partial\vec{\mathcal{E}}}{\partial t}\times\mu_0\vec{\mathcal{H}} \tag{3}$$

Specifically, for time harmonic fields of time-dependence ej_t , the time-average force density is given by

$$\langle\vec{f}\rangle=\frac{1}{2}\mathrm{Re}[-j\omega\varepsilon_0(\varepsilon_r-1)\vec{E}^*\times\mu_0\vec{H}] \tag{4}$$

where *E* and *H* are the frequency domain electric and magnetic fields, respectively.
At the interfaces between the dielectric layers, a polarization surface charge is created, giving rise to a surface force density.
The surface force density at the boundary reads:

$$F_{x,\nu}=\frac{1}{2}\varepsilon_0(\mathcal{E}^{(+)}_{x,\nu})^2\left(\frac{\varepsilon_\nu^2}{\varepsilon_{\nu+1}^2}-1\right) \tag{6}$$

This total surface force density may be conveniently divided into two contributions from the two polarization densities of each layer at the interface. The force density on the surface charge of layer *v* is given by

$$F^{(-)}_{x,\nu}=\frac{1}{2}\varepsilon_0(\mathcal{E}^{(+)}_{x,\nu})^2(\varepsilon_\nu^2-1)>0 \tag{7}$$

and the force density on the polarization surface charge of layer *v+1* is

$$F^{(+)}_{x,\nu}=-\frac{1}{2}\varepsilon_0(\mathcal{E}^{(+)}_{x,\nu+1})^2(\varepsilon_{\nu+1}^2-1)<0 \tag{8}$$

Experimental setup is showed in Figure 2.

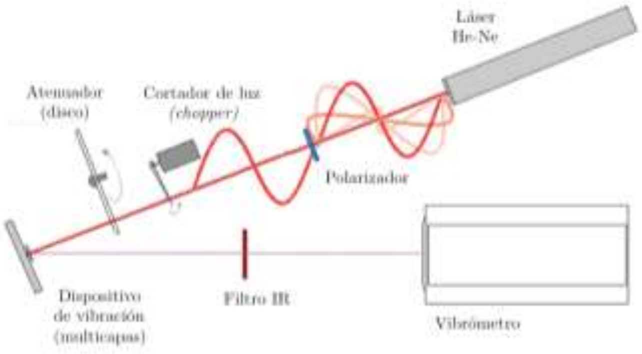

Figure 2 Experimental setup.

We show experimental evidence of this force when the photonic structure is capable of making auto-oscillations and forcedoscillations. We measured peak displacements and velocities ranging from 2 up to 35 microns and 0.4 up to 2.1 mm/s with a power of 13 mW.